Purification and analysis of ferrous chloride for an Fe/Cr flow battery application

JP du Toit

orcid.org/0000-0003-1979-2004

Dissertation accepted in partial fulfilment of the requirements for the degree *Master of Science in Chemistry* at the North-West University

Supervisor:	Prof HM Krieg
Co-supervisor:	Mr N Mans
Co-supervisor:	Mr DJ van der Westhuizen

Graduation December 2022

27251594

RESEARCH CONTRIBUTIONS

Presentation at International Conference

du Toit, J. P.; Krieg, H. M.; Mans, N.; van der Westhuizen D. J. (2022). UV-Vis Spectrophotometric analytical technique for monitoring Fe^{2+} in the positive electrolyte of an ICRFB. **The International Flow Battery Forum (IFBF®) Summer conference, 28 & 29 June 2022, Brussels, Belgium: Poster nr. 19.**

Article published in peer reviewed journal

du Toit, J. P.; Krieg, H. M.; Mans, N.; van der Westhuizen D. J. (2022). *UV-Vis Spectrophotometric analytical technique for monitoring Fe^{2+} in the positive electrolyte of an ICRFB.* In: Journal of Power Sources, article reference: POWER_POWER-D-22-04168.

ABSTRACT

The inevitable depletion of fossil fuels, concerns about adverse human health effects of air pollution, reduction of greenhouse gas emissions and climate change are globally recognised as some of the main factors that drive the transition to renewable energy sources. Unfortunately, these renewable energy sources are intermittent by nature and consequently are inharmonious with continuous supply required from large scale electrical grids. To bridge this gap, large scale energy storage solutions (LESS) have to be developed and implemented. As a result, research in the field of scalable electrochemical energy storage technology has received significant attention, resulting in promising solutions such as the redox flow battery (RFB). Although the all vanadium RFB (VRFB) has received the most attention to date, the iron-chromium RFB (ICRFB) holds significant potential for South Africa as both the iron and chrome used in the electrolyte are abundantly available in SA. To address some of the challenges facing the commercialisation of ICRFBs, two aspects related to the iron chrome electrolyte used will be investigated in this study.

To develop the ICRFB towards viability and market penetration, the next step is to evolve the lab-scale designs and experiments into large-scale demonstration units that have similar performance than the optimised lab-scale setups. Such upscaling requires significant volumes of electrolyte with a similar purity to those bought at a high cost for the laboratory-scale experiments. Hence, the first aim of this study was to develop a purification technique that could reduce the cost of the ICRFB electrolyte without sacrificing battery performance. This was attained by developing a crystallisation process in an open system where N_2 was used to inhibit the oxidation of Fe^{2+}. According to the inductively coupled plasma - optical emission spectroscopy (ICP-OES) and ultraviolet-visible spectrophotometry (UV-Vis) analysis, 81.3% Cu, 70.5% Ni and 62.7% Sn was removed from a low-cost industrial grade ferrous chloride ($FeCl_2$) solution during the crystallisation process. After 8 hours of ICRFB operation, the charge/discharge capacity of the purified electrolyte was 124.6% higher than that of the unrefined $FeCl_2$ solution and 5.6% lower than the lab-grade electrolyte. Similarly, it yielded 6.8% less capacity decay than the unrefined $FeCl_2$ and only 0.1% more than the lab-grade electrolyte. The improved performance was likely due to the removal of impurities, which would result in fewer side reactions such as the hydrogen evolution reaction (HER).

One of the drawbacks of the ICRFB compared to VRFB is its high rate of capacity decay resulting in imbalance due to the accumulation of Fe^{3+} in the positive electrolyte. Developing a simple method for monitoring the electrolyte, i.e. the Fe^{2+}/Fe^{3+} speciation, during operation, would provide information for the required rebalancing process. Furthermore, such electrolyte monitoring could also provide information on the state of charge (SOC) and state of health

(SOH) of the ICRFB. However, quantifying Fe^{3+} concentrations are difficult when requiring a non-destructive analysis of iron redox species that are present at high concentrations. In the second part of this study, a method using the near infrared (NIR) light absorption of Fe^{2+} in conjunction with Beer's law was developed to accurately and non-destructively quantify both Fe^{2+} and Fe^{3+} concentrations. Using 920 nm NIR light (UV-Vis) and the absorption constants, a function was developed to analyse the crystallised $FeCl_2$ solution. In addition, the effects of temperature, the HCl concentration, as well as the presence of Cr^{3+}, Bi catalyst and other dissolved gasses on the adsorption was investigated. The mathematical function of absorption that was derived in this study obtained a detection error of 3.33% for [Fe^{2+}] and 3.08% for [Fe^{3+}] during validation, and could be used to monitor the positive electrolyte of an ICRFB and hence the imbalance at varying temperatures and sample path lengths *in- situ*. The robust and instantaneous analytical method can be used to quantify dissolved iron species with different valences at high concentrations. This method was then also used during the crystallisation study to analyse the purity of the $FeCl_2$ produced, confirming that the proposed N_2 blanketing adequately inhibited Fe^{2+} oxidation during crystallisation.

Keywords: Iron-chromium redox flow battery, Low-cost energy storage, Electrolyte purification, Electrolyte impurities, Iron redox speciation, Beer-Lambert Law, Near-IR, UV-Vis Electrolyte monitoring method.

PREFACE

“Chemistry as a science is still in its infancy. I hold to my view because there is still so much beyond our understanding even in the simplest systems the chemist has cared to deal with.”

-Henry Taube-

As a student through my entire school education, chemistry seemed like this perfect science that was all figured out, with almost no unknowns in filled textbooks just waiting for me. Unknowingly at that moment, this was probably caused by the requirement from lecturers and writers to sometimes oversimplify subject matters so that young and undeveloped minds may understand them. Nevertheless, this creates a sense of naivety in young aspiring students in which they think chemistry works like mathematics, sometimes complex but always solvable by correcting one or two mistakes. The one thing I had to realise that stood out the most during this project, was that there exists a painful contrast between the theoretical science of chemistry and real-life results. From temperature changes between day and night during winter, affecting known and unknown system equilibriums, to spontaneous oxidation of “stable” species during weighing or sampling. Not to mention the complications brought forward by electronics and laboratory equipment that always seem to rectify themselves just before I gave up. Multiple failures unknown to textbooks and experimental designs repeatedly had to be deciphered, eventually tearing down my naivety and any drop of belief I had left in simplicity, albeit at the cost of repeating experiments, late nights, and my sanity. This might not have been exactly what Professor Henry meant, but I had to learn the hard way that the vast science of chemistry, highly deserving of respect, is not all figured out or simple, but definitely still in its infancy.

This research was driven by my desire as an aspiring scientist to not only obtain a degree, but to contribute to the advancement of energy storage technology. Energy storage is truly a worthy research topic with a growing significance as the world continues to move towards using renewable energy sources. Therefore, I firmly believe that it is important to advance energy storage technologies, especially those that rationally possess the potential for real-world applications.

I would like to give thanks to the following people:

The work in this paper was supported by the National Research Foundation (NRF) of South Africa [grant number 131689]. This work would also be impossible without the North-West University.

To the people at the North-West University of Potchefstroom: For the support and guidance from my professor and mentor Henning M. Krieg and extremely helpful study leaders Nico Mans and Derik J. van der Westhuizen. Thanks also to Hanno Bizjet, who helped me crystallise so much ferrous chloride solution.

To my colleagues and friends Mias and Stephan, who helped me find some humour in failures. To my parents Piet and Elize du Toit, who always believe in me and gave me this opportunity. Lastly, thanks to my fiancée Bianca and the rest of my friends and family, who somehow also always believe in me, and encouraged me during difficult times.

LIST OF FIGURES

Chapter 1

Figure 1: Illustration of renewable energies linked to existing power grids. (Photo credit: https://www.ascendanalytics.com/pages/integrated-resource-planning.) 1
Figure 2: Schematic diagram of an RFB.[19] 2
Figure 3: 60 MWh VRFB installation in Japan (Photo credit: Sumitomo Electric Industries, Ltd.) 3

Chapter 2

Figure 4: Illustration of RFB components. 10
Figure 5: Photograph of 0.1 M vanadium sulfate solutions in 2 M H_2SO_4. From the left the negative electrolyte V^{2+} (charged) and V^{3+} (discharged), followed by the positive electrolyte VO^{2+} (discharged) and VO_2^+ (charged).[16] 11
Figure 6: Conductivity of negative (left) and positive (right) electrolytes (2 M vanadium in 5 M total SO_4) as a function of SOC, for temperatures 10 ± 1, 20 ± 1 and 30 ± 1 °C.[20] 14
Figure 7: Absorbance of 750 nm light vs. 0% to 100% SOC of a negative VRFB electrolyte (2 M vanadium).[20] 15
Figure 8: Two case study plots of A_{diff} at 575 nm over SOC from UV-Vis calibration data (positive electrolyte) performed in the charge/discharge in-operando mode.[19] 16
Figure 9: Structure of Nafion CEM.[40] 20
Figure 10: Octahedral ferrous chloride tetrahydrate ($FeCl_2 \cdot 4H_2O$). 22
Figure 11: Schematic illustration of copper cementation using iron.[61] 24
Figure 12: Typical components of a UV-Vis analyser.[71] 26
Figure 13: Ferrozine ligand. 27
Figure 14: Luminol and the chemiluminescence induced when it reacts with oxygen from atmosphere and carbamide peroxide.[71] 28
Figure 15: Hydrogen production with varying copper contamination concentrations for the VRFB.[60] 29

Chapter 3

Figure 16: Schematic diagram of the lab-scale RFB cell used in the testing station. 48
Figure 17: Vacuum filtered $FeCl_2 \cdot xH_2O$ crystals. 50

Figure 18: Picture of purified $FeCl_2 \cdot 5H_2O$ (left - solid and 1 M solution in 1.0 M HCl) and unrefined $FeCl_2$ (right – 1 M solution in 1.0 M HCl and undiluted). 51
Figure 19: Picture of a $FeCl_2 \cdot xH_2O$ (216.83 g mol^{-1}) crystal obtained from filtration after fractional crystallisation of the unrefined $FeCl_2$ solution. 52
Figure 20: Coulombic efficiency, voltage efficiency, and energy efficiencies obtained from electrolytes with (a) an unrefined, (b) a purified and (c) a commercial $FeCl_2$ source. 57
Figure 21: Charge and discharge times over 10 cycles obtained from electrolytes with (a) an unrefined, (b) a purified and (c) a commercial $FeCl_2$ source..... 59
Figure 22: Discharge capacity of different electrolytes over 10 cycles. 60
Figure 23: Cost breakdown of unrefined $FeCl_2$ purification scaled for 10 L ICRFB electrolyte. 62

Chapter 4

Figure 24: Absorbance of cuvettes containing water (45 °C). 76
Figure 25: Absorbance spectra of undiluted 1.3 M Fe^{2+} and Fe^{3+} in 1.00 M HCl. 79
Figure 26: Absorbance spectra of ~0.013 M (100 x dilution) Fe^{2+} and Fe^{3+} in 1.00 M HCl. 80
Figure 27: The influence of the HCl concentration on the absorbance between 850 nm and 1000 nm (20 °C). 82
Figure 28: Total absorbance of a mixture containing Fe^{2+}, Fe^{3+} and Cr^{3+} as a function of the HCl concentration (20 °C). 83
Figure 29: Absorbance at 920 nm of Fe^{2+} at different concentrations (20 °C). 85
Figure 30: Absorbance of Fe^{2+} at 920 nm at different concentrations and temperatures. . 86
Figure 31: $\varepsilon Fe2+$ from 293.15-318.15 K. 86
Figure 32: Absorbance of Fe^{3+} at different concentrations (20 °C). 87
Figure 33: Absorbance of Fe^{3+} at 920 nm at different concentrations and temperatures. . 88
Figure 34: Absorbance of catholytes 1-5 with varying Fe^{2+}/Fe^{3+} ratios between 900 nm and 940 nm, prior to RFB charge cycles (20 °C)..... 90
Figure 35: RFB charge curves of catholytes 1-5 with 1.3 M Cr^{3+} anolyte (65 °C). 91
Figure 36: Absorbance of catholytes 1-5 with varying Fe^{2+}/Fe^{3+} ratios between 900 and 940 nm, after RFB charge cycles (20 °C). 93

Chapter 5

Figure 37: Flow diagram of the purification process established and used in this study. 100

Figure 38: Flow diagram of the purification process established and used in this study, including possible optimisation possibilities. 102

Figure 39: NIR Spectra of 1.30 M solutions of Fe in 1.0 M HCl, for unrefined $FeCl_2$ and purified $FeCl_2$ (25 °C)..... 106

Appendix

Figure A 1: NIR spectra (900-940 nm) of 5 mM Bi_2O_3 in 1.0 M HCl..... 108

Figure A 2: NIR spectra (900-940 nm) of RFB cycled catholyte: 1 M Fe^{2+}, 1 M Cr^{3+}, 1 M HCl……...108

Figure A 3: Colour shift between uncharged (Cr^{3+}) anolyte and charged (Cr^{2+}). 109

Figure A 4: Injection method used to combat Cr^{2+} oxidation in atmosphere. 109

Figure A 5: Absorbance shifts in visible region of ICRFB anolyte (Cr^{3+}/Cr^{2+}) at (charging) and resting OCV potentials..... 110

LIST OF TABLES

Chapter 2

Table 1: Summary of essential ICRFB and VRFB differences 20

Chapter 3

Table 2: ICP-MS detection limits and accuracy on internal QC, for all measured impurities……44
Table 3: Compositions, concentrations and sources of different electrolytes synthesised for testing in the lab-scale ICRFB. 46
Table 4: ICP-MS results for those metal impurities present in purified $FeCl_2$ that are likely to promote HER in an ICRFB 53
Table 5: ICP-OES results for metal impurities present in purified $FeCl_2$ 54
Table 6: ICP-OES results for PGMs present in purified $FeCl_2$ 55
Table 7: Comparison of ICRFB performance with electrolytes from different $FeCl_2$ sources……57
Table 8: Cost comparison of commercial and purified Fe sources to synthesise 10 L electrolyte, excluding $CrCl_3$, Bi, or HCl. 62

Chapter 4

Table 9: Composition and concentrations of samples used for determining the influence of [HCl] on Cr^{3+}, Fe^{2+} and Fe^{3+} absorption of NIR light. 74
Table 10: Composition and concentrations of two sets of 15 samples used for determining the molar absorption constants for Fe^{2+} and Fe^{3+} 75
Table 11: Catholyte ratios and compositions from ICP-OES analysis 77
Table 12: Absorbance at different HCl concentrations (0.500 – 5.00 M). 81
Table 13: ICP-OES and UV-Vis results with NIR analysis method/function error for catholytes 1-5 prior to RFB charge cycles. 91
Table 14: RFB charge times and capacity for catholytes 1-5. 92

Appendix

Table A 1: ICP-OES analysis of mixed configuration electrolyte before (i) and after (f) 24 cycles..... 109

Table A 2: Δ [Fe3] obtained from charge capacity of catholyte, vs Δ [Fe3] as obtained from UV-Vis method..... 109

NOMENCLATURE AND SYMBOLS

A	Ampere
Abs	Absorbance
A_{diff}	Normalised difference absorbance
AEM	Anion exchange membrane
Anolyte	Negative electrolyte
ASR	Area specific resistance
A_{total}	Total observed absorbance
b	Sample path length (cm)
CAPEX	Capital expenditures
Catholyte	Positive electrolyte
CE	Coulombic efficiency
CEM	Cation exchange membrane
CCV	Continuing calibration verification
DC	Direct current
E^0	Standard electrode potential
EE	Energy efficiency
Electrolyte	Conductive solution that contains the active redox species used by an RFB
F	Faraday's constant
HDPE	High density polyethylene
HER	Hydrogen evolution reaction
ICP-MS	Inductively coupled plasma - mass spectrometry
ICP-OES	Inductively coupled plasma - optical emission spectroscopy
ICRFB	Iron-chromium redox flow battery
IEM	Ion exchange membrane
kW h	Kilowatt hour
LESS	Large-scale energy storage solution
Li-ion	Lithium-ion
LIB	Lithium-ion battery
LOQ	Limits of quantification
M	Molarity in mol L^{-1}
MHz	Megahertz
MilliQ-water	Ultra-purified deionised water
MWh	Megawatt hour
NASA	National aeronautics and space administration

NIR	Near infra-red
NRF	National research foundation
OCV	Open-circuit cell voltage
PEM	Proton exchange membrane
PGM	Precious group metals
pH	Potential hydrogen
ppm	Parts per million in mg L^{-1}
QC	Quality control
$Q_{cap(charge)}$	Theoretical charge capacity
R	Ideal gas constant
RFB	Redox flow battery
SCX	Strong cation exchange
SHE	Standard hydrogen electrode
SOC	State of charge
SOH	State of health
T	Temperature in kelvin (K)
TEMPOL	4-hydroxy-2,2,6,6-tetramethyl-1-pipperidinyloxyl
UV-Vis	Ultraviolet-visible
V	Volt
VE	Voltage efficiency
VRFB	Vanadium redox flow battery
z	Total solution [Fe]
ZAR	South African rand
Ɛ	Molar absorptivity in mol^{-1} dm^3 cm^{-1}
$	United states dollar

TABLE OF CONTENTS

RESEARCH CONTRIBUTIONS i

ABSTRACT ii

PREFACE iv
LIST OF FIGURES vi
LIST OF TABLES ix
NOMENCLATURE AND SYMBOLS xi
TABLE OF CONTENTS xiii

CHAPTER 1 1

INTRODUCTION 1

1. Background 1
2. Problem Statement 4
3. Aim and objectives 4
4. References 5

CHAPTER 2 8

LITERATURE REVIEW 8

1. Introduction 8
2. Redox flow battery technology 9
   - 2.1 Brief overview 9
   - 2.2 The all-vanadium RFB 10
     - 2.2.1 Introduction 11
     - 2.2.2 Electrolyte monitoring methods 12
   - 2.3 Iron-Chromium RFB (ICRFB) 16
     - 2.3.1 Introduction 16
     - 2.3.2 Development 17
   - 2.4 VRFB vs ICRFB 20
3. Fe/Cr electrolyte 21
   - 3.1 Ferrous chloride 21
     - 3.1.1 Purification methods 22
     - 3.1.2 Analytical methods 25
   - 3.2 Effect of impurities on electrolyte performance 28
     - 3.2.1 Effect of impurities 29
     - 3.2.2 Impurities of concern 30
4. Beer-Lambert law 31
5. Conclusion 32
6. References 33

CHAPTER 3 40

Purifying $FeCl_2$ as an economical alternative source for ICRFB electrolyte synthesis 40

Abstract 40
1. Introduction 41
2. Materials and methods 42
   - 2.1 Ferrous chloride 42
   - 2.2 Purification procedure 42
   - 2.3 Analysis of $FeCl_2 \cdot xH_2O$ 43
   - 2.4 ICRFB tests 44
     - 2.4.1 Electrolytes 45
     - 2.4.2 Performance indicators 46
     - 2.4.3 ICRFB testing station 47
3. Results 48

3.1 Purification and fractional crystallisation of $FeCl_2$ 49
3.2 Impurities 52
3.3 RFB results 55
3.3.1 Efficiencies 55
3.3.2 Electrolyte storage capacity 57
3.3.3 Electrolyte capacity and decay 60
3.4 Cost analysis 61
4. Conclusion 62
5. References 64

CHAPTER 4 67

UV-Vis Spectrophotometric analytical technique for monitoring Fe^{2+} in the positive electrolyte of an ICRFB. 67

Abstract 67
1. Introduction 68
2. Theory 71
3. Materials and methods 72
3.1 Materials 72
3.2 Instrumentation 72
3.2.1 UV-Vis Spectrophotometry 72
3.2.2 ICP-OES 73
3.3 Experimental procedure 73
3.3.1 Wavelength determination 73
3.3.2 Deduction of the Beer-Lambert Law 74
3.3.3 Experimental determination of $\boldsymbol{\varepsilon Fe2+}$ and $\boldsymbol{\varepsilon Fe3+}$ 75
3.3.4 Experimental error 76
3.3.5 Method validation 77
3.3.5.1 Electrolyte preparation 77
3.3.5.2 ICRFB Testing station 78
4. Results and discussion 78
4.1 Wavelength determination 78
4.2 Deduction of the Beer-Lambert Law 80
4.3 Experimental determination of $\boldsymbol{\varepsilon Fe2+}$ 84
4.4 Experimental determination of $\boldsymbol{\varepsilon Fe3+}$ 87
4.5 Final approximation for $[Fe^{2+}]$ 89
5. Method validation 90
6. Conclusions 94
7. References 95

CHAPTER 5 98

EVALUATION AND RECOMMENDATIONS 98

1. Purification procedure for $FeCl_2$ 98
1.1 Impurity removal 98
1.3 Economic feasibility 101
2. $FeCl_2$ and positive electrolyte analysis 103
2.1 Iron redox speciation analysis technique 103
2.2 Analysis of purified $FeCl_2$ 105
Appendix 108

CHAPTER 1

INTRODUCTION

1. Background

It has become globally accepted that the transition to renewable energy sources is the key to reducing greenhouse gas emissions and ensuring the provision of adequate energy supplies for future demands.[1] This greenhouse gas emission reduction is not only directed towards the mitigation of climate change, but also aims at improving living conditions by reducing environmental pollution.[2-3] Although this transition has been ongoing for some time, the inevitable depletion of fossil fuel reserves has also introduced a significant and urgent driving factor.[4] Consequently, many efforts and resources are currently being spent on the development of renewable energy sources to progress the transition as swiftly as possible.

One of the main challenges impeding such progress occurs when integrating these renewable energy sources into large electrical grids (Figure 1), which will become more pressing as we strive towards renewables becoming the primary source of energy.[5-6] All grids encounter fluctuating demand seasonally and daily, with winter and on-peak hours experiencing increased energy consumption. Since renewable energies are intermittent by nature (sunlight, wind), the supply and demand is incongruous.[7] As a result, stability and control of renewable energy sources and supply is required, which in turn necessitates large-scale energy storage solutions (LESSs).[7-10]

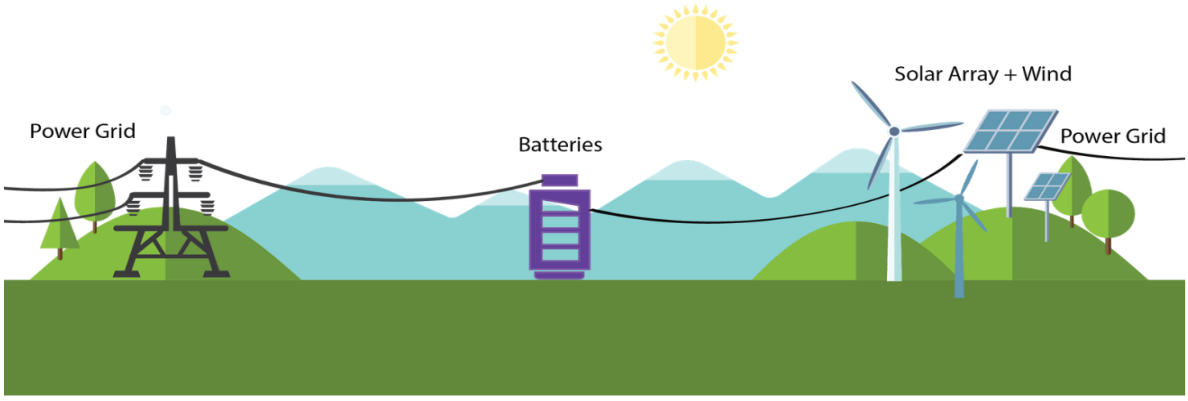

Figure 1: Illustration of renewable energies linked to existing power grids. (Photo credit: https://www.ascendanalytics.com/pages/integrated-resource-planning.)

In the light of progressing the transition to renewable energy sources, various types of stationary LESSs are being researched, including electrochemical, electrical, chemical, thermal and mechanical processes, of which the electrochemical processes have been receiving the most attention.[9] The most preferred electrochemical energy storage at present are Lithium-Ion (Li-ion) batteries, which have seen monumental improvements, leading to the successful application for various small to large-scale applications, most notably for electric vehicles.[11] The application of Li-ion batteries for large-scale applications makes sense considering their outstanding energy densities compared to other battery technologies. However, firstly, it is expensive to scale up mainly due to resource limitations[12-13] and secondly the modular up-scaling of Li-ion energy storage is strenuous. As a result, research is ongoing to find more practical and economically low-cost solutions for LESSs.

Redox flow batteries (RFBs), as shown in Figure 2, are excellent candidates, as they have a flexible design with fairly uncomplicated up-scaling, without the safety compromising fire hazard of other stationary LESSs using Li.[14-16] While RFBs have lower energy densities than Li-Ion batteries, a stationary LESS is often not limited by the size needed for the larger volumes of electrolyte required. The current leading RFB technology in terms of research and performance is the all-vanadium RFB (VRFB). However, it is also plagued by the same challenge as the Li-ion battery, i.e. a high cost due to the price of the vanadium used in the electrolyte.[17-18] Hence, although the VRFB is a promising battery technology, reducing the cost further would enable wider market penetration. For example, using an RFB with an electrolyte consisting of more abundant materials, such as the iron-chromium RFB (ICRFB), might provide enough financial advantages to contribute to the transition to a renewable energy economy.[18]

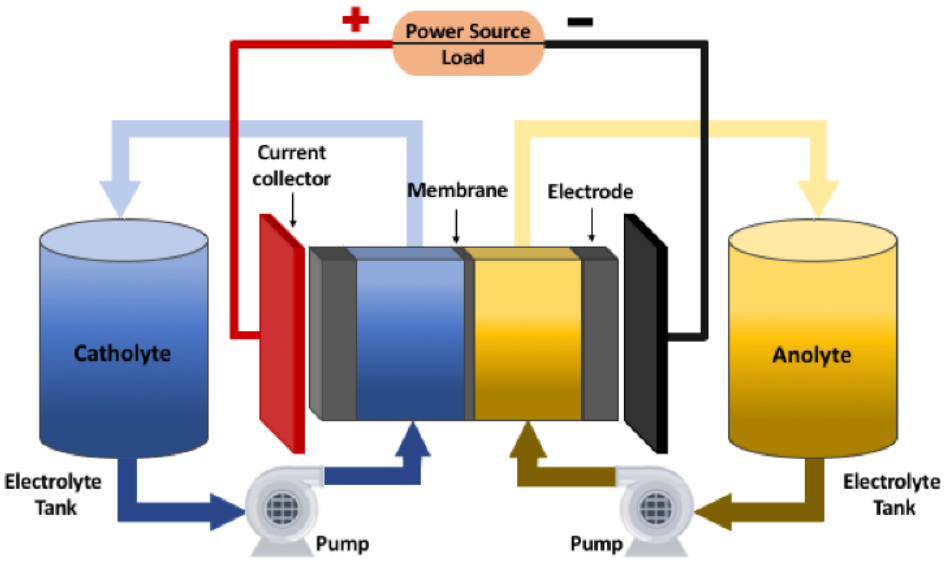

Figure 2: Schematic diagram of an RFB.[19]

The VRFB and ICRFB share many similarities, as both are aqueous flow batteries that use two acidic electrolytes (catholyte and anolyte) containing dissolved metal ions (vanadium or iron/chrome), which are stored in separate tanks and then pumped past electrodes separated by an ion exchange membrane (IEM) where the charging and discharging occurs using the different oxidation states of the metal ions. As mentioned, the VRFB has seen considerably more developments than the ICRFB, including for example, developing processes for the further purification of electrolyte materials, studies on the effects of impurities in the electrolytes as well as electrolyte analysing and monitoring techniques.[18,20-25] These developments have allowed the construction of several operational facilities and demonstration plants in the past decade, including the 60 MWh installation by Sumitomo Electric Industries, Ltd. in Japan, where the LESS has successfully been combined with renewable energy sources in a large-scale application to stabilise the renewable energies used for Hokkaido's grid network (Figure 3).[26]

Figure 3: 60 MWh VRFB installation in Japan (Photo credit: Sumitomo Electric Industries, Ltd.)

With the extensive information available, existing VRFB research can provide a framework for ICRFB developments owing to the similarities in battery functionality, which could support further development of the ICRFB. Using this knowledge to develop a more economical ICRFB could then fill the existing gap in research that the ICRFB requires to become a suitable LESS candidate.

2. Problem statement

The ICRFB is an excellent candidate as an economically feasible LESS. However, it has unfortunately not yet seen the research and development that is required to become widely incorporated. It is beneficial to the technology that iron and chromium metals are abundant, however, electrolyte cost could be reduced. Currently, electrolytes are synthesised from lab-grade purified chemicals for small-scale for research, which require high purity levels, as many elements could negatively influence the sensitive electrochemical RFB system.[14,18,27] However, it is likely the lack of research regarding alternative and cheaper ICRFB electrolyte production methods that is restricting the ICRFB from reaching its full economical potential.

In addition, the ICRFB is also challenged by a higher capacity decay per cycle from the chemical imbalance between the electrolytes than has been obtained with the VRFB, thus requiring extensive rebalancing.[18] Although such rebalancing of the capacity decay can be attained, it would require an accurate yet simple way to measure the lost capacity, for example by measuring the concentrations of the various ionic species during charging and discharging. Such a simplified method does, however, not yet exist for the ICRFB.

3. Aim and objectives

The aim of this study is therefore to improve ICRFB technology by developing methods to purify the iron chloride and analyse the iron species in the electrolyte. The first objective is to develop a cheap and simple method to produce the purified iron chloride for an electrolyte. The second objective is to develop a simplistic analytical technique that can be used to distinguish between the iron species, Fe^{2+} and Fe^{3+}, during operation, which would be necessary for quantifying the rebalancing required. Accomplishing these two goals could drastically aid the development of this promising technology while enhancing its cost-effectiveness, aiding the ICRFB in becoming a feasible LESS and providing it with greater opportunity for global market penetration.

4. References

1. Menyah, K.; Wolde-Rufael, Y., CO2 emissions, nuclear energy, renewable energy and economic growth in the US. *Energy Policy* **2010,** *38* (6), 2911-2915.
2. Madaniyazi, L.; Xerxes, S., Outdoor air pollution and the onset and exacerbation of asthma. *Chronic Diseases and Translational Medicine* **2021,** *7* (2), 100-106.
3. Suman, A., Role of renewable energy technologies in climate change adaptation and mitigation: A brief review from Nepal. *Renewable and Sustainable Energy Reviews* **2021,** *151*, 111524.
4. Höök, M.; Tang, X., Depletion of fossil fuels and anthropogenic climate change—A review. *Energy Policy* **2013,** *52*, 797-809.
5. Weber, A. Z.; Mench, M. M.; Meyers, J. P.; Ross, P. N.; Gostick, J. T.; Liu, Q., Redox flow batteries: a review. *Journal of Applied Electrochemistry* **2011,** *41* (10), 1137-1164.
6. Sangster, A. J., Massive energy storage systems enable secure electricity supply from renewables. *Journal of Modern Power Systems and Clean Energy* **2016,** *4* (4), 659-667.
7. Ding, C.; Zhang, H.; Li, X.; Liu, T.; Xing, F., Vanadium Flow Battery for Energy Storage: Prospects and Challenges. *The Journal of Physical Chemistry Letters* **2013,** *4*.
8. Darling, R. M.; Gallagher, K. G.; Kowalski, J. A.; Ha, S.; Brushett, F. R., Pathways to low-cost electrochemical energy storage: A comparison of aqueous and nonaqueous flow batteries. *Energy and Environmental Science* **2014,** *7* (11), 3459-3477.
9. Kebede, A. A.; Kalogiannis, T.; Van Mierlo, J.; Berecibar, M., A comprehensive review of stationary energy storage devices for large scale renewable energy sources grid integration. *Renewable and Sustainable Energy Reviews* **2022,** *159*.
10. Connolly, D. A Review of Energy Storage Technologies *For the integration of fluctuating renewable energy*. University of Limerick, 2009.
11. Tian, Y.; Zeng, G.; Rutt, A.; Shi, T.; Kim, H.; Wang, J.; Koettgen, J.; Sun, Y.; Ouyang, B.; Chen, T.; Lun, Z.; Rong, Z.; Persson, K.; Ceder, G., Promises and Challenges of Next-Generation "Beyond Li-ion" Batteries for Electric Vehicles and Grid Decarbonization. *Chemical Reviews* **2021,** *121* (3), 1623-1669.
12. Chen, T.; Jin, Y.; Lv, H.; Yang, A.; Liu, M.; Chen, B.; Xie, Y.; Chen, Q., Applications of Lithium-Ion Batteries in Grid-Scale Energy Storage Systems. *Transactions of Tianjin University* **2020,** *26* (3), 208-217.
13. Wadia, C.; Albertus, P.; Srinivasan, V., Resource constraints on the battery energy storage potential for grid and transportation applications. *Journal of Power Sources* **2011,** *196* (3), 1593-1598.

14. Zeng, Y. K.; Zhou, X. L.; An, L.; Wei, L.; Zhao, T. S., A high-performance flow-field structured iron-chromium redox flow battery. *Journal of Power Sources* **2016,** *324*, 738-744.
15. Lourenssen, K.; Williams, J.; Ahmadpour, F.; Clemmer, R.; Tasnim, S., Vanadium redox flow batteries: A comprehensive review. *Journal of Energy Storage* **2019,** *25*, 100844.
16. Hering, G. Burning concern: Energy storage industry battles battery fires https://www.spglobal.com/marketintelligence/en/news-insights/latest-news-headlines/burning-concern-energy-storage-industry-battles-battery-fires-51900636 (accessed 2022/04/07).
17. Li, L.; Kim, S.; Wang, W.; Vijayakumar, M.; Nie, Z.; Chen, B.; Zhang, J.; Xia, G.; Hu, J.; Graff, G.; Liu, J.; Yang, Z., A Stable Vanadium Redox-Flow Battery with High Energy Density for Large-Scale Energy Storage. *Advanced Energy Materials* **2011,** *1*.
18. Zeng, Y. K.; Zhao, T. S.; An, L.; Zhou, X. L.; Wei, L., A comparative study of all-vanadium and iron-chromium redox flow batteries for large-scale energy storage. *Journal of Power Sources* **2015,** *300*, 438-443.
19. Clemente, A.; Ramos, G. A.; Costa-Castelló, R., Voltage H∞ Control of a Vanadium Redox Flow Battery. *Electronics* **2020,** *9* (10), 1567.
20. Corcuera, S.; Skyllas-Kazacos, M., State-of-Charge Monitoring and Electrolyte Rebalancing Methods for the Vanadium Redox Flow Battery. *European Chemical Buletin* **2012,** *1*, 511-519.
21. Park, J. H.; Park, J. J.; Lee, H. J.; Min, B. S.; Yang, A., Influence of Metal Impurities or Additives in the Electrolyte of a Vanadium Redox Flow Battery. *Journal of The Electrochemical Society* **2018,** *165* (7), A1263-A1268.
22. Zhang, W.; Liu, L.; Liu, L., An on-line spectroscopic monitoring system for the electrolytes in vanadium redox flow batteries. *RSC Advances* **2015,** *5* (121), 100235-100243.
23. Skyllas-Kazacos, M.; Kazacos, M., State of charge monitoring methods for vanadium redox flow battery control. *Journal of Power Sources* **2011,** *196* (20), 8822-8827.
24. Cao, L.; Skyllas-Kazacos, M.; Menictas, C.; Noack, J., A review of electrolyte additives and impurities in vanadium redox flow batteries. *Journal of Energy Chemistry* **2018,** *27* (5), 1269-1291.
25. Reynard, D.; Vrubel, H.; Dennison, C. R.; Battistel, A.; Girault, H., On-Site Purification of Copper-Contaminated Vanadium Electrolytes by using a Vanadium Redox Flow Battery. *ChemSusChem* **2019,** *12* (Issue 6), 1222-1228.

26. Huang, Z.; Mu, A., Research and analysis of performance improvement of vanadium redox flow battery in microgrid: A technology review. *International Journal of Energy Research* **2021,** *45*, 14170–14193.
27. Zhang, H.; Tan, Y.; Li, J.; Xue, B., Studies on properties of rayon- and polyacrylonitrile-based graphite felt electrodes affecting Fe/Cr redox flow battery performance. *Electrochimica Acta* **2017,** *248*, 603-613.

CHAPTER 2

LITERATURE REVIEW

1. Introduction

The transition to renewable energy sources is a major priority with the aim to mitigate climate change and prepare for the inevitable depletion of fossil fuels.[1-3] However, using intermittent renewable energies such as solar or wind, requires energy storage, especially if they are to be integrated into an existing power grid.[4-7] As a result, research in the area of large-scale energy storage solutions (LESS) has become a popular topic where technologies such as Li-ion batteries (LIBs) and redox flow batteries (RFBs) have received considerable attention.[6,8-11] Despite the desirable features of LIBs, such as their high energy density, the cost of upscaling, and consequently the cost of large-scale energy storage, is intrinsically high due to the resource limitations of lithium.[12] Upscaling of RFBs has, however, been shown to be extremely cost effective, especially at the longer discharge durations required for integration of renewable energies.[11] In addition, RFBs offer extreme design flexibility, i.e., a larger storage capacity simply requires larger electrolyte holding tanks while a larger power output simply requires additional battery cells (larger stack).[6] Furthermore, RFBs are also considered to be safe and energy efficient LESSs.[4,7]

Renewable energies combined with LESSs are especially relevant to South Africa (SA). This can be attributed to the fact that SA, in recent years, has experienced a limited and unstable power supply due to outdated and ill-maintained coal plants. While the current run-down power plants are able to meet the electricity needs during off-peak times, they struggle to do so during peak times. In this case, LESSs can be used to stabilise the grid, i.e., electricity is stored during off-peak times and used during peak times.

This literature overview will be introduced with a discussion on RFB technology in Section 2. The RFB discussion will be followed by an in-depth discussion on the iron-chromium RFB electrolyte in Section 3. Finally, a short overview regarding the theory of the Beer-Lambert law will be given in Section 4.

2. Redox flow battery technology

2.1 Brief overview

In Figure 4, the typical components of a single cell RFB are illustrated. As previously mentioned, RFBs are flow batteries that use electrolytes to store and dispense electrochemical energy. As can be seen in Figure 4, a RFB consists of a battery stack and electrolyte holding tanks. The energy conversions (charging or discharging) take place in the battery stack while the charged or discharged electrolytes are stored in the separate holding tanks. For the energy conversions to take place, the electrolytes are pumped through their respective positive and negative half-cells. The two half-cells amount to a full cell which contains two crucial components for energy efficiency (EE) and stability, namely the redox couples and the ion exchange membrane (IEM) that separates them. The membrane, which may be an anion exchange membrane (AEM) or a cation exchange membrane (CEM), should selectively allow ion transfer of charge carrier species during the redox reactions, while acting as a physical barrier between electrolytes, which prohibits the migration of active species from one half-cell to the other. On both sides of the IEM there are carbon/graphite felts, bipolar plates and current collectors. Graphite felts against the bipolar plates are commonly used as flow-through electrodes, providing a high surface area for electron exchange. Bipolar plates (normally made from a polymer matrix containing conductive metal alloys and graphite) protect the current collectors, often made from copper, from the corrosive environment.[13] The poles of the cell, connected to the metal current collectors, are connected to a direct current (DC) charging source or load. Depending on the intended power output of the RFB, the poles are easily connectable to an electrical inverter. These components, which amount to a single RFB cell, are usually repeated in a series of cells in the order of bipolar plate, graphite felt, membrane, graphite felt, bipolar plate sandwiched between two current collectors and two end plates, owing to the functionality of bipolar plates, to assemble a stack. Combining cells in series has the advantage of functioning at higher voltages, since the output voltage is equal to the sum of the individual cell voltages (which is primarily determined by the standard redox potential of the used redox couples).

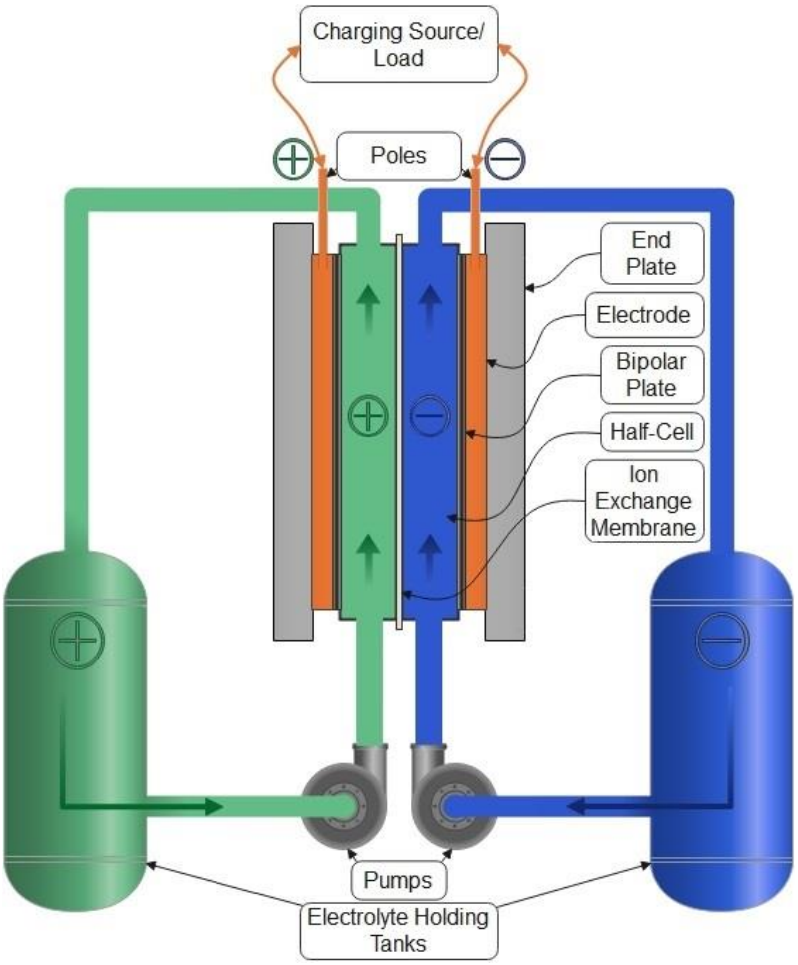

Figure 4: Illustration of RFB components.

2.2 The all-vanadium RFB

The all-vanadium RFB (VRFB) uses vanadium as active species in both half-cells and it is the most developed RFB technology to date. Since the VRFB is the most researched flow battery, the technology and research are considered extensively in this study since the knowledge can support ICRFB development. This section will cover a brief introduction of the VRFB system and a review on literature about the analytical techniques that have been used to analyse or monitor acidic electrolyte mixtures. Combining what has been gained from the literature in this section with that discussed in the Fe/Cr electrolyte review (Section 3), will hopefully provide the information required to find the most effective, accurate and yet simple method for analysing a Fe/Cr electrolyte.

2.2.1 Introduction

As the most researched RFB to date, the VRFB was first introduced by Professor Maria Skyllas-Kazacos and her co-workers in 1985. While the continued research has led to substantial developments since then, the high electrolyte cost, due to the scarcity of vanadium, still impedes significant market penetration of the VRFB.[6,11]

As mentioned, the VRFB uses vanadium as active species in both half-cells, exploiting all four of its oxidation states as is shown in Equations (1-3).[4,14-15] The 4 different oxidation states each provide an electrolyte solution that is vibrantly and distinctly coloured (Figure 5). Consequently, distinct colour changes are observed in both half-cells during the charge and discharge process.

Positive electrode reaction:

$$VO^{2+} + H_2O - e^- \rightleftharpoons VO_2^+ + 2H^+ \qquad +1.004\,V\ vs.SHE \qquad (1)$$

Negative electrode reaction:

$$V^{3+} + e^- \rightleftharpoons V^{2+} \qquad -0.255\,V\ vs.SHE \qquad (2)$$

Overall cell reaction (forward reaction = discharge):

$$VO^{2+} + V^{3+} + H_2O \rightleftharpoons VO_2^+ + V^{2+} + 2H^+ \qquad \Delta E^0 = +1.259\,V \qquad (3)$$

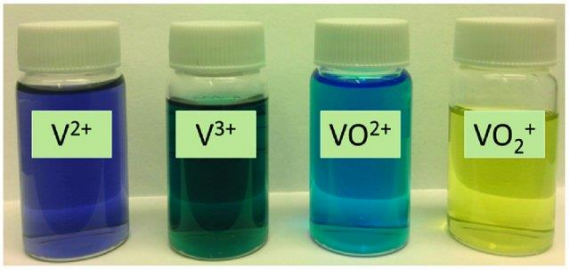

Figure 5: Photograph of 0.1 M vanadium sulfate solutions in 2 M H_2SO_4. From the left the negative electrolyte V^{2+} (charged) and V^{3+} (discharged), followed by the positive electrolyte VO^{2+} (discharged) and VO_2^+ (charged).[16]

2.2.2 Electrolyte monitoring methods

As will be explained in Section 2.3, RFBs that use acidic electrolytes (including the VRFB) suffer from chemical imbalance that can originate from various sources, with unwanted side reactions and membrane crossover being the most prominent.[17-19] Hence, these RFBs require effective and integrated chemical or electrochemical rebalancing systems. However, for effective rebalancing, information from some form of electrolyte monitoring system is required, delivering data either on the state of charge (SOC), or the state of health (SOH).[17-21] Sensors providing that information would ensure that rebalancing can be scheduled periodically, allowing the retention of the charge/discharge capacity of the battery.[20] In this section, an overview of the developments regarding the monitoring/analysing of vanadium electrolyte properties during battery operation will be reviewed. Since the VRFB has very similar workings than the ICRFB, this review should provide adequate information to aid in the development of an ICRFB electrolyte analysing technique.

2.2.2.1 Open-circuit cell voltage (OCV)

One of the easiest and most common ways to measure the SOC is to measure the OCV.[18] After having measured the potential difference over the positive and negative electrodes of the battery, the Nernst equation can be used to determine the concentrations of the active species present at any given time.[20] However, this method fails as soon as battery operation creates chemical imbalance between cells, which results in an unknown error that increases over time.[17] Nonetheless, promising techniques, like dynamic modelling, have been developed that can be integrated with the OCV measurements to minimise such errors. Such successful integrations have been demonstrated providing accurate periodical electrolyte rebalancing.[22-23]

2.2.2.2 Potentiometric titration

This method uses the same principle as traditional titrations where a chemical provides a visible indicator to determine the end point of the titration. However, by measuring the potential of an appropriate indicator electrode instead of using a colour change, significantly more accurate titration values are obtained.[24] However, although this method could be used to accurately quantify electrolyte components, it is unsuitable for in-line electrolyte monitoring as it requires the extraction of samples for external monitoring.[21]

2.2.2.3 Reference electrodes

Another method that has been explored for accurate SOC monitoring was to insert reference electrodes into both the electrolytes of the two half-cells, providing simultaneous measurements of the Nernst potentials of both half-cells. The advantage of this method is that calibration and corrections of the reference potential could be obtained using 50% SOC as a standard for the internal calibration.[19] However, this method encountered errors due to inaccuracies in potential readings that could originate either from impurities in the reference electrode, or from unstable electrode readings in general.[17,25] A possible reason for such unstable readings is that accurate and hence sensitive electrodes usually have to be stored in buffer solutions to maintain stability. Hence, they are not suitable to remain immersed in concentrated acidic solutions such as battery electrolytes for extended periods of time as would be required for in-line monitoring. To overcome that, an extremely robust reference electrode would have to be developed that maintains high resolution data output in spite of indefinite exposure to harsh chemical environments.

2.2.2.4 Conductivity

Another method that has been considered to monitor vanadium electrolytes, was by relating the SOC of the electrolytes to their respective conductivities (mS cm^{-1}). Research has shown that the conductivity of both the positive and negative electrolytes display a linear correlation with their SOC, confirming the potential feasibility of this method.[20] Skyllas-Kazacos and Kazacos[20] observed a linear relationship between the experimentally obtained SOC data and the conductivity at different temperatures (Figure 6), showing that the conductivity increases with increasing temperature and electrolyte SOC.

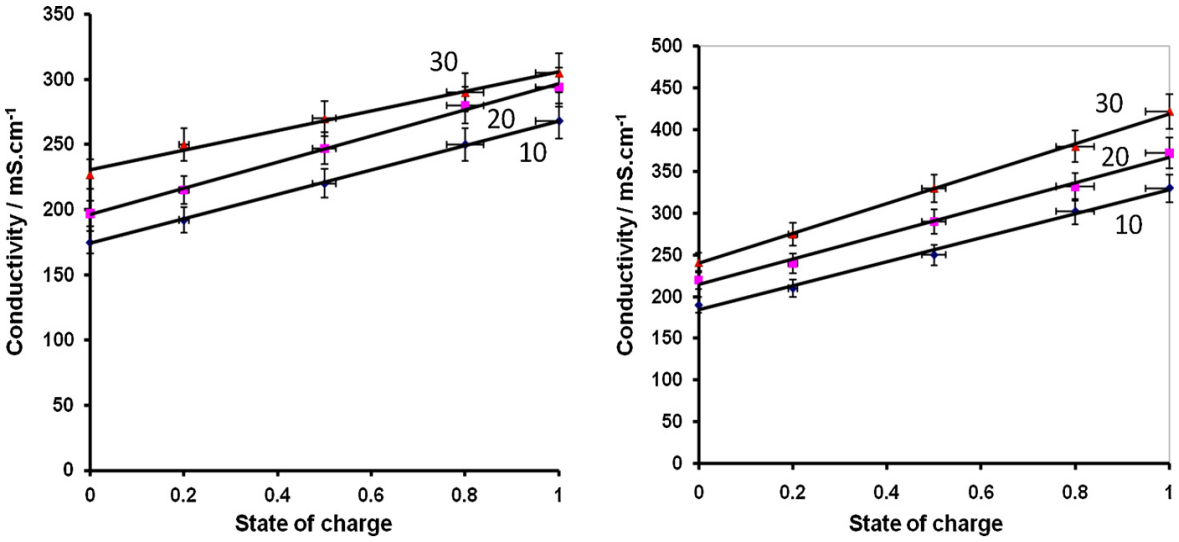

Figure 6: Conductivity of negative (left) and positive (right) electrolytes (2 M vanadium in 5 M total SO_4) as a function of SOC, for temperatures 10 ± 1, 20 ± 1 and 30 ± 1 °C.[20]

However, despite the linearity, it was confirmed that the readings obtained by this method can be skewed by chemical imbalances caused by membrane crossover due to conductivity shifts when the amounts of vanadium and sulfate change or build up in either of the half-cells during battery operation. Furthermore, inaccuracies from unstable readings when measuring conductivity often occur, correlating with the slight error of the conductivity probe and the small temperature deviations shown in Figure 6.[18,20] The unstable readings are especially concerning considering the low detection resolution of this method.[21] Hence, to effectively use conductivity to measure the SOC, a monitoring method with a higher detection resolution, detection range and accuracy would be required to ensure a stable measurement.

2.2.2.5 Spectroscopic methods

Although spectroscopic methods such as ultra-violet visible (UV-Vis) spectrophotometry will be discussed in more detail when discussing ICRFBs (Section 3), it is included in this section in view of its suitability also for VRFBs. Since VRFB electrolytes differ in colour between discharged and charged states (see Figure 5), absorption or transmittance spectroscopy has been proposed as non-destructive methods to monitor electrolyte SOC or SOH *in-situ*.[20,26-27] Since then, research in spectroscopic methods to monitor VRFB electrolyte has developed significantly.[19-21,28] Using appropriate monochromatic wavelengths, spectroscopy can, in

theory, monitor the concentrations of specific chemical species in RFB electrolytes without being affected by changes from chemical imbalance.

Research has, however, shown that spectroscopic methods could become challenging due to the presence of non-linearities between absorbances and SOC values caused by the high concentrations of metals often present in electrolytes.[19] It is clear that dilution would not be feasible due to the obvious negative effect this would have on battery performance. Hence, the direct application of spectrophotometry as a SOC or SOH monitoring method is consequently currently still hindered. This problem could, however, be alleviated by simulating the desired dilution factor, using a cuvette with a narrower path length. Other remaining non-linearities, if constant, could theoretically be corrected using appropriate calibrations. Figure 7 provides an example showing the relationship between the absorption and the SOC for an undiluted negative VRFB electrolyte. A strong linear relationship with a slight scattering of datapoints can be seen from 5% to 100% SOC, where the absorption of monochromatic 750 nm light increases due to the increased electrochemical conversion of V^{3+} to V^{2+}.[20]

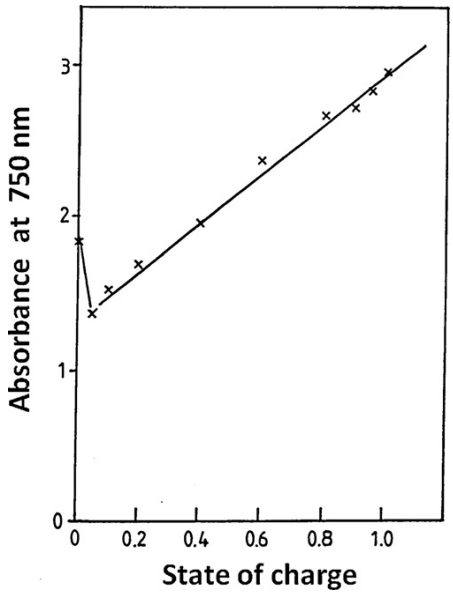

Figure 7: Absorbance of 750 nm light vs. 0% to 100% SOC of a negative VRFB electrolyte (2 M vanadium).[20]

A more recent study investigating the suitability of UV-Vis spectrophotometry to measure the SOC used the normalised difference absorbance (A_{diff}) spectrum of the positive and negative electrolytes, providing SOC values with high accuracies. In the example shown in Figure 8, 575 nm monochromatic light was used to produce A_{diff} values that were correlated with voltage

measurements in real time during charge/discharge cycles, yielding calibration curves. It is clear from the testing of the calibration curves that the SOC values from the charge/discharge samples fitted the positive parabolic calibration curve well in both cases. This confirms the potential of this UV-Vis in-operando mode to accurately and instantaneously measure SOC values in VRFB systems.[19]

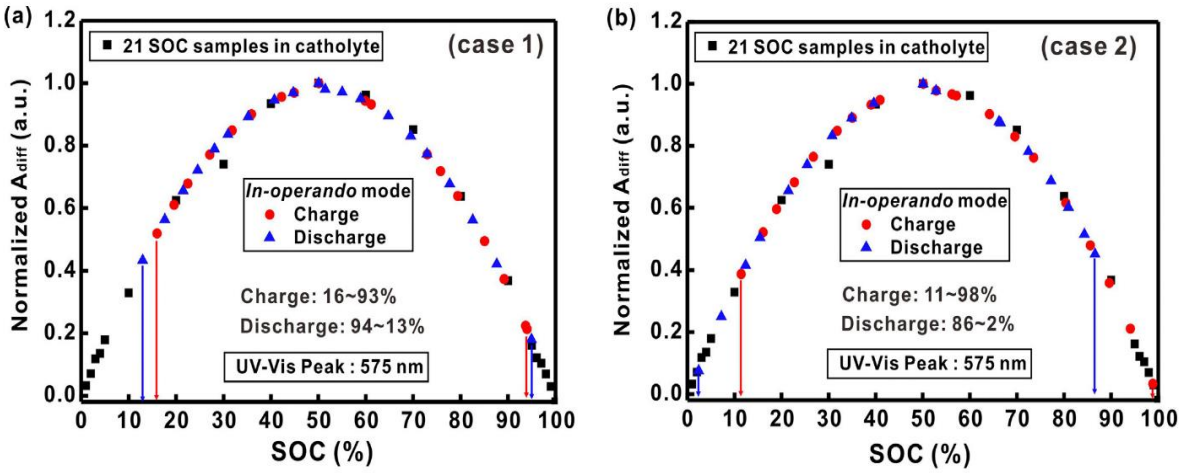

Figure 8: Two case study plots of A_{diff} at 575 nm over SOC from UV-Vis calibration data (positive electrolyte) performed in the charge/discharge in-operando mode.[19]

It is thus clear that spectroscopic methods, such as spectrophotometry, have significant potential as modern SOC monitoring methods in VRFBs.[19] Since spectroscopic techniques can be used to determine an accurate SOC value via in-situ electrolyte analysis for the VRFB, they can potentially be excellent candidates for analysing ICRFB electrolytes as well.

2.3 Iron-Chromium RFB (ICRFB)

2.3.1 Introduction

In this section, the literature on ICRFBs will be discussed briefly since this study focuses on the development of an analytical monitoring technique for the ICRFB. The ICRFB uses the two oxidation states of both iron and chromium in a chloride environment to store and discharge energy according to Equations (4-6).[24]

Positive electrode reactions:

$$Fe^{2+} \rightleftharpoons Fe^{3+} + e^{-} \qquad +0.771\,V\ vs.SHE \qquad (4)$$

Negative electrode reactions

$$Cr^{3+} + e^{-} \rightleftharpoons Cr^{2+} \qquad -0.408\,V\ vs.SHE \qquad (5)$$

Overall cell reaction (forward reaction = charge):

$$Fe^{2+} + Cr^{3+} \rightleftharpoons Fe^{3+} + Cr^{2+} \qquad \Delta E^{0} = +1.179 \qquad (6)$$

2.3.2 Development

This section will highlight some of the key developments made since the introduction of the ICRFB, before discussing some of the drawbacks of this battery, including comments on the current state of ICRFB development.

2.3.2.1 Origin and first developments

The ICRFB was introduced in 1974, together with the establishment of RFBs, by L.H. Thaller, a researcher for NASA, as a flexible energy storage solution with many possible applications.[29] In the following years, NASA released various papers on the progress of the ICRFB. In addition, they were also involved in a study in 1982 that extensively investigated UV-Vis spectrophotometry as a means to study the chemistry of the negative electrolyte of an ICRFB. Using a flow-through cuvette system, they identified the participating chromium complexes in aqueous chloride solutions at the anode surfaces of the negative electrolyte (Equation (7)), using wavelengths in the range of 350 nm to 1000 nm.[30]

(Charging = forward reaction)

$$Cr(H_2O)_5Cl^{2+} + e^{-} \rightleftharpoons Cr(H_2O)_5Cl^{+} \qquad (7)$$

It was believed that the electron transfer reaction on the anode surface, for both charge and discharge, followed an inner-sphere reaction pathway bridged by the chloride ligand.[30-31] Strong evidence from visible spectrophotometry and ion-exchange chromatography indicated that these two complexes are the active species in the negative electrolyte during battery operation. At room temperature, they found that the active Cr^{3+} species, $Cr(H_2O)_5Cl^{2+}$, was in

equilibrium with an inactive Cr^{3+} species, $Cr(H_2O)_6^{3+}$. By increasing the temperature, the equilibrium shifted towards the active species, leaving the electrolyte solution with less inactive $Cr(H_2O)_6^{3+}$, which resulted in improved charging performance above 50% SOC.[31] Based on this, an increase in the ICRFB operating temperature, as well as the deposition of bismuth as catalyst on the anode surface, was proposed to help increase the rate-limiting inner-sphere reaction rate that is considered to be slow.[27,32]

As expected, a year later it was shown that operating an ICRFB with a bismuth catalyst at 65 °C instead of room temperature not only improved the charge acceptance rate of the chromium electrolyte above 50% SOC, but also confirmed the necessity of higher temperatures during upscaling.[32] However, such increases in temperature unfortunately also resulted in declining membrane selectivity, leading to increased crossover of active species and hence increased capacity losses. To counteract the crossover, a mixed reactant electrolyte (containing both iron and chromium) for both half-cells was proposed in 1984[33], which, combined with the increase in operating temperature and, made the ICRFB feasible for bulk energy storage.[33-34]

2.3.2.2 Drawbacks and further developments

Despite the advances, capacity loss arguably remained the most prominent challenge for ICRFBs. According to the final report from NASA in 1984, one of the major causes for the chemical imbalance occurring between the two half-cells during charge and discharge cycles was that the charging voltage of 1.2 V would promote the hydrogen evolution reaction (HER) at the negative electrode (Equation (8)), which is further favoured with increasing impurity content.[33]

$$2H^+ + 2e^- \rightarrow H_2 \qquad E^0 = 0.000\,V \qquad (8)$$

Accordingly, imbalance occurs when the oxidation of Fe^{2+} leads to the reduction of protons instead of the Cr^{3+}. Additionally, imbalance is aggravated by oxygen intrusion in either electrolyte holder, leading to the oxidation of species.[34] This was later confirmed by Pawar *et al*,.(1988) who demonstrated, when using UV-Vis spectrophotometry and a positive electrolyte consisting of $K_4Fe(CN)_6$, that air-tight systems retained balance significantly longer compared to open air systems.[27] Nonetheless, the chemical imbalance caused by HER, resulting in the positive electrolyte becoming more oxidised than the negative electrolyte over time, necessitated the development of an electrochemical rebalancer as proposed by NASA in 1984.[33]

The first-generation rebalancer circulated a side stream of positive electrolyte through a cell that reduced Fe^{3+} using hydrogen gas, which could be sourced from the negative cell's HER or from an external H_2 vessel. However, over time its performance deteriorated due to flooding of the hydrogen electrode as well as electrolyte contamination due to the diffusion of platinum from the hydrogen electrode.[34] However, in spite of these shortcomings and challenges, NASA was able to demonstrate the potential of the ICRFB as a LESS.[33]

To improve on the shortcomings of the previous rebalancer, NASA developed a 2nd-generation rebalancer containing an iron-chlorine rebalance cell that had improved stability without any remarkably negative effects on ICRFB performance.[34] While this rebalancer also recirculated a side stream of the positive electrolyte, they used chloride ions instead of hydrogen for the electrolyte reduction, which required approximately 1% of the energy needed to charge the ICRFB. The chloride ions would oxidise to chlorine gas as the Fe^{3+} in the electrolyte was reduced. The chlorine gas generated was purged from the system with N_2 and reacted with potassium hydroxide. It is noteworthy that the chlorine gas could also be reacted with the hydrogen produced at the anode to replenish the H^+ lost by the system, however this might cause an unwanted accumulation of Cl^-. When using the iron-chlorine rebalancer cell, a consistent performance of an ICRFB for six months with intermittent cycling was reported, with the resulting performance losses attributed to the membrane and the electrodes. Upscaling their ICRFB (from 14.5 cm^2 cells to 867 cm^2) yielded promising results, which they then described as "a well-defined approach to energy storage".[34]

Despite these promising results, the interest in the ICRFB declined with the discovery of the VRFB. Another factor that restricted the development of this technology was the lack of suitable membrane materials, which initially resulted in high area specific resistances (ASR) and low selectivities.[29,35-36] Since then there have been significant advances in membrane technology, which led to the wide use of the perfluorinated Nafion IEMs in most modern RFBs.[9,37-39] Typically, Nafion contains an aliphatic perfluorinated backbone with ether-linked side chains containing sulfonate functional groups that allow the cation exchange process (Figure 9).[40] Not only are these materials chemically inert, but they also retain their selectivity at the higher temperatures required for the efficient operation of many RFBs.

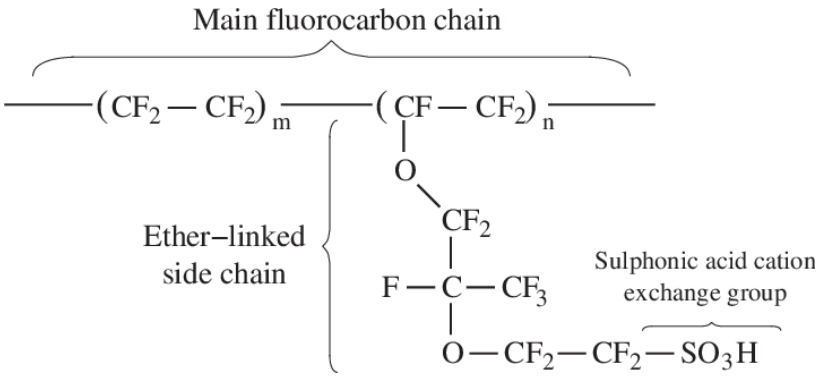

Figure 9: Structure of Nafion CEM.[40]

2.4 VRFB vs ICRFB

Despite its shortcomings, some remarkable developments have recently led to the advancement of ICRFB technology, including catalyst systems that restrict the HER, the use of thermally treated carbon/graphite felts as electrodes in a flow-through cell to increase the surface area of electron transfer reactions, and alternative use of flow field cells.[38,41-42] In this section, a comparison of cost is drawn between the newer generation ICRFBs and the current frontrunner, the VRFB. The most important differences are tabulated in Table 1. It is clear from the cost of the metal ores (as in February 2022) that vanadium is significantly more expensive than iron and chrome (without considering the costs of purification) due to its scarcity. This then directly translates to the cost of the VRFB electrolyte which is approximately 10 times more expensive. The global production of ferrochrome in 2017 was estimated at 11.7 megatons, with South Africa holding the largest chromium ore reserves.[43-44] On the other hand it is clear that the vanadium electrolyte not only has a higher energy density, but more importantly suffers less directly from capacity decay than the ICRFB.

Table 1: Summary of essential ICRFB and VRFB differences

	ICRFB	VRFB
Cost of metal ore ($/kg)	Cr(28.5% Cr) = 0.20[45-46] Fe(62% Fe) = 0.15[47]	V(98% V_2O_5) = 23.59[47]
Electrolyte cost ($/kW h)[11]	17	112
Energy density (W h kg^{-1})[4]	15	25
Discharge capacity after 30 cycles* (%)[11]	65	90

*Without rebalancing

As previously stated, (see Section 2.2.1), the VRFB is currently the most advanced system. However, the high electrolyte cost will remain a challenge, where its own success could result

in an increased vanadium demand, resulting in further price hikes. In addition, the solubility of the vanadium ion is low compared to that of the ICRFB.[11,48] Thanks to advances made in membrane technology and the lower cost of the iron-chrome compared to the vanadium, the ICRFB is an attractive LESS considering its potential economic viability for wide market penetration.[35,38,49]

3. Fe/Cr electrolyte

It was mentioned that the objectives of this study were twofold. The first objective was to investigate a possibly cheaper and trivial method to produce a purified electrolyte. Although the Fe/Cr electrolyte is less expensive than the vanadium electrolyte (Section 2.4), further cost reduction of the Fe/Cr electrolyte would benefit the ICRFB technology, considering its effect on the CAPEX cost of a LESS.

The second objective was to develop an analytical technique to quantify and monitor the Fe^{2+} and Fe^{3+} concentrations, which is not only important for the purification process, but more importantly for quantifying the progression of imbalance (RFB) or rebalancing during operation. The reason for focussing the development of an analytical method on the Fe rather than the Cr component is related to the cause of imbalance. It was mentioned that HER, which is largely responsible for the increasing chemical imbalance, causes increasing Fe^{3+} concentrations in the positive electrolyte (Section 2.3.1), thus leading to less Fe^{2+} being available for the reduction of Cr^{3+} during charging. Hence, quantifying the Fe^{2+} or Fe^{3+} concentrations would provide a direct measure of imbalance and rebalance. This section will focus mainly on the Fe component in the form of $FeCl_2$ (Section 3.1) in terms of purification and analysis, followed by a discussion on the effect of impurities on electrolyte performance (Section 3.2).

3.1 Ferrous chloride

This section will provide a brief introduction to the chemistry of iron followed by an overview of both purification (Section 3.1.1) and analytical techniques (Section 3.1.2). Ferrous chloride is widely used as a cost-effective additive to control the dissolved sulfide levels in wastewater, in dye's, medicines and in the metallurgical industry.[50-51] It is most commonly obtained as green and stable hydrated octahedral $FeCl_2 \cdot 4H_2O$ (Figure 10) crystals derived from its white-greenish anhydrous, but hygroscopic $FeCl_2$. Unfortunately, the ferrous ion Fe^{2+} readily oxidises to ferric Fe^{3+} in the presence of numerous oxidising agents, including atmospheric

oxygen. Hence, $FeCl_2 \cdot 4H_2O$ spontaneously oxidises in the atmosphere in the presence of moisture, producing mainly Fe_2O_3 (rust). $FeCl_2 \cdot 4H_2O$ must therefore be stored in air-tight vessels and oxygen exposure should be avoided. Another route to prevent oxidation at room temperature is to dissolve the $FeCl_2 \cdot 4H_2O$ in an acidic solution (pH < 2).[52] This is most probably also beneficial to the ICRFB electrolyte, as the Fe^{2+} is somewhat stabilised by the 1M HCl solution. Although oxygen intrusion in the pH < 2 environment could still oxidise the Fe^{2+} to Fe^{3+}, the reaction is reversible (rebalancing - see Section 2.3.2.2).

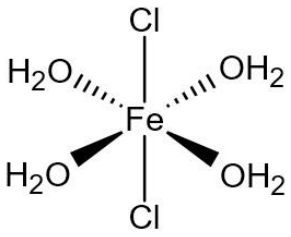

Figure 10: Octahedral ferrous chloride tetrahydrate ($FeCl_2 \cdot 4H_2O$).

3.1.1 Purification methods

In this brief review, the two most common techniques (recrystallisation and cementation) used to purify inorganic solutions or salts, with the focus on removing metal impurities for the ICRFB while minimising spontaneous atmospheric oxidation of Fe^{2+}, are presented.

3.1.1.1 Recrystallisation

Recrystallisation or fractional crystallisation is a method that uses differences in solubility of different compounds (a function of temperature) in a solvent to purify a compound of interest. When using this technique to remove undesired impurities, the impure salt is typically dissolved in a solvent or solvent mixture to obtain a saturated solution, often at elevated temperatures, for example by evaporating the solvent using heat and/or vacuum techniques. After the desired concentration has been reached, the solution is cooled. During cooling, the solution becomes oversaturated as the solubility usually decreases with temperature.[53] If controlled carefully, this can then lead to the precipitation or crystallisation of the desired species in a purified form, as the impurities are present at lower concentrations and generally remain in solution.[53] The crystals can then be filtered and thus separated from the mother

liquor containing most of the impurities. Subsequently, the crystals can be washed using a cooled solvent to remove both residual impurities that might still be adsorbed on the crystals, and any remaining solvent. However, this washing almost unavoidably also redissolves a small layer of the crystals. This, with the loss of any residual dissolved species during crystallisation, implies that a compromise must be sought between the yield and purity when using recrystallisation. To optimise this, processes have been developed with low yield and high purity that are then repeated to increase the yield.[54-55]

For RFBs in general, and ICRFB specifically, pure electrolytes are required, leading to an increased cost of the electrolyte. Recrystallisation of impure but inexpensive $FeCl_2 \cdot 4H_2O$ could be suitable to provide $FeCl_2$ with an adequate purity for use in ICRFBs. Already in 1956, a recrystallisation process was used to purify $FeCl_2 \cdot 4H_2O$ required for a hydrolysis experiment.[56] In this case, only iron powder and HCl were required, while parts of the procedure were conducted in an inert nitrogenated atmosphere to prevent oxidation. While both iron powder and HCl are inexpensive, creating an inert process might prove challenging, which can, however, be achieved to a lesser extent using N_2 without an enclosure.

3.1.1.2 Cementation

Although cementation has been used for centuries to cost-effectively recover dissolved metals from solutions, it is also an excellent technique to remove impurities from solutions.[57-58] During cementation, solids of a lesser noble metal (with a lower galvanic potential) are introduced to a solution containing the more noble dissolved metal. In theory, the more noble dissolved metal gets reduced to its solid state, while the less noble metal (introduced as a solid) gets oxidised and, consequently, dissolves into the solution. While the galvanic series shows which metals are more noble than others, the process is influenced, and hence becomes more complicated in practice, due to the varying chemical environments such as pH changes.[58-59] To determine the effect of pH, Pourbaix diagrams of different metals and their reduction potentials can be used to show the various electron transfer reactions in an aqueous environment as a function of pH.

An excellent example of cementation is the removal of copper from an iron solution, which is also relevant for this study, where copper contamination of VRFB electrolytes, even at very low concentrations (ppm), have a detrimental effect on battery performance by promoting chemical imbalance through the HER as discussed previously.[60] Comparing the standard potentials at which the VRFB and ICRFB operate, it is logical to expect that copper would also

be detrimental for the ICRFB. Figure 11 schematically depicts cementation where copper is electrochemically deposited onto a piece of iron, while simultaneously oxidising the iron into the acidic solution.

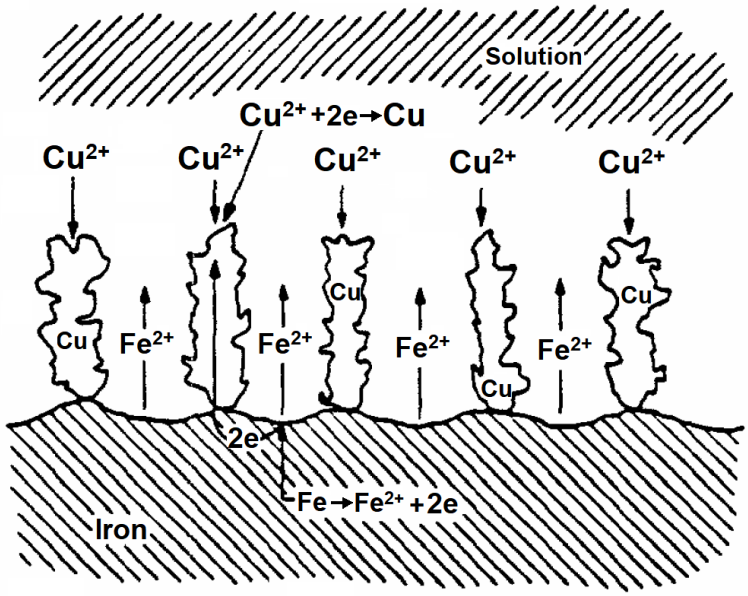

Figure 11: Schematic illustration of copper cementation using iron.[61]

In this example, in theory, 0.88 g of iron should be introduced as Fe^{2+} to the solution for each gram of copper reduced from the solution. However, in practice, an average of 1.4 g to 3.2 g Fe is reduced per gram of copper due to the several reactions that occur simultaneously:[61]

$$2Fe^{3+} + Fe \rightarrow 3Fe^{2+} \quad (9)$$

$$2H^{+} + Fe \rightarrow Fe^{2+} + H_2 \quad (10)$$

$$Fe + \frac{1}{2}O_2 + 2H^{+} \rightarrow 2Fe^{2+} + H_2O \quad (11)$$

$$2Fe^{2+} + \frac{1}{2}O_2 + 2H^{+} \rightarrow 2Fe^{3+} + H_2O \quad (12)$$

$$Cu + 2Fe^{3+} \rightarrow Cu^{2+} + 2Fe^{2+} \quad (13)$$

From the above reactions, specifically reactions (12) and (13), leading to Fe^{3+} and Cu^{2+} in the final product ($FeCl_2$), should be avoided or mitigated. On the other hand, reactions (9), (10) and (11) are beneficial as both Fe and Fe^{3+} are reduced or oxidised to the desired Fe^{2+}, which should be promoted by the simple addition of Fe to the acidic solution.

Hence, by using cementation, unwanted nobler metals such as copper can be removed from a $FeCl_2$ solution by adding an excess of solid Fe particles which can be filtered off after the reaction. Such an excess of Fe would promote the removal of Cu^{2+} as well as the reduction of Fe^{3+}. As discussed previously, oxygen exposure should be avoided to prevent Fe^{2+} oxidation (Equation (12)). Considering the low cost of Fe metal, cementation would provide an excellent low-cost method to purify $FeCl_2$, producing a cost-effective purified electrolyte.

3.1.2 Analytical methods

This section will review methods that have been used to analyse solutions containing dissolved iron in view of the aim of developing a method to analyse and distinguish between Fe^{2+} and Fe^{3+}. From the literature, it is clear that distinguishing between Fe^{2+} and Fe^{3+} proves difficult, even more so when dealing with relatively low concentrations of iron in water. Among many of the reasons provided, some of the main contributors were the reactivity as well as the reversibility of the two species.[62-64]

3.1.2.1 ICP-OES and ICP-MS

Inductively coupled plasma - optical emission spectroscopy (ICP-OES) instruments use extremely high temperatures (6000-8000 °C) to excite atoms, causing them to emit characteristic spectra that are then analysed. The high temperatures are obtained by creating a plasma by ionising argon gas with a radio-frequency induction coil that typically radiates power between 0.5 and 2.7 kW with varying frequencies below 50 MHz.[65] By passing a small amount of the dissolved sample in solution through the plasma, the concentrations of the elements are obtained with high accuracy, even at concentrations in the ppb range (μg L^{-1}). However, despite the accuracy and sensitivity of this method, it cannot distinguish between different species of the same element. However, ICP-OES was used in this study to accurately determine the total iron (Fe^{2+} and Fe^{3+}) content in solutions/electrolytes, as well as metal impurities.

ICP can also be coupled with, for example, mass spectrometry (ICP-MS), or other analytical techniques to expand their capabilities. While the ICP-MS is commonly used as an atomic spectroscopy method, an improvement was made in 1988 that only realised in the late 1990s, known as the sector field (sf) ICP-MS, that helped reduce signal interferences.[66] Since then the technology has also been coupled with other analytical techniques to provide accurate concentrations of different redox species. For example, in a recent study, strong cation

exchange chromatography (SCX) was coupled with ICP-sf-MS to obtain simultaneous redox speciation of various metal species, including iron. In this case, the chromatography separates the ions based on their polarity differences, ensuring that the redox species are separated before reaching the ICP-MS.[62] Using this combination of methods, Fe species were measurable with a detection limit of 0.5 µg L^{-1}.[67] This has also been achieved by coupling ICP-MS with other forms of chromatography techniques, showing their suitability to differentiate specifically between Fe^{2+} and Fe^{3+}.[63,68] However, despite these advances, these combined technologies are complex, expensive, lead to sample destruction and require sample dilution, making them unfeasible for continuous or in-line electrolyte analysis.

3.1.2.2 UV-Vis molecular absorption spectroscopy

UV-Vis molecular absorption spectroscopy, also known as UV-Vis spectrophotometry, measures the amount of light a sample absorbs. In a traditional UV-Vis instrument (Figure 12), UV, visible and sometimes near infra-red (NIR) light, commonly produced by deuterium and tungsten lamps, are processed through a monochromator, which acts as a wavelength selector that enables the light exposure of singular wavelengths to a sample.[69] After passing through the sample, a detector measures the amount of remaining light, thereby providing the amount of light absorbed. Many molecules and atoms absorb electromagnetic radiation as their electrons are excited into higher states of vibrational or rotational energies.[70] Since different molecules and atoms have different allowed states of energy, this method can be used not only quantitively, but also qualitatively.

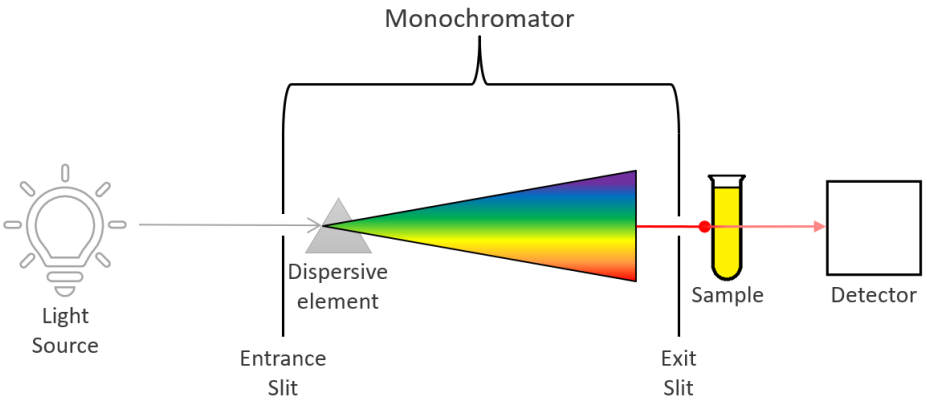

Figure 12: Typical components of a UV-Vis analyser.[71]

The wide applicability, high sensitivity, selectivity, accuracy and automation capabilities make UV-VIS a very useful method in analytical chemistry.[70] It is therefore likely that this method could be suitable for developing a measurement method to determine the iron redox speciation in ICRFB electrolytes. Additionally, as previously mentioned (Section 2.2.2.5), UV-VIS has seen promising development as a non-destructive electrolyte monitoring method in VRFB research.

Apart from its role in ICRFBs, iron plays a significantly larger role in a broad range of biological processes.[72] This has led to a demand for alternative analytical techniques to quantify dissolved iron species. In recent years, studies within the biogeochemical field have investigated the suitability of Ferrozine (Figure 13) as a possible method to monitor dissolved Fe^{2+} and Fe^{3+} ion concentrations in water bodies.[73-75] Ferrozine acts as a highly reactive ligand with chelating properties that chelates specifically Fe^{2+} to produce Fe^{II}-$(Ferrozine)_3$. As a result of its specific absorption bands, this organometallic compound is intensely and vibrantly coloured, which enables the ions to be quantified with visible light spectrophotometry (562 nm).[72,76] When applied correctly, a linear correlation between absorption and concentration is obtained in the dissolved iron concentration range of 1 to 200 µM.[76]

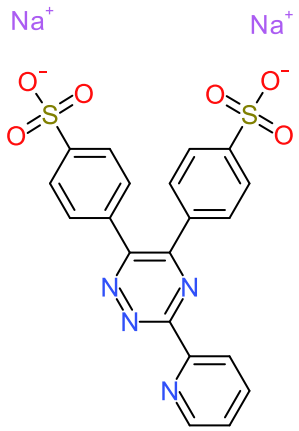

Figure 13: Ferrozine ligand.

The Ferrozine method was specifically developed to analyse ferrous iron at very low concentrations, making it unsuitable for high ferrous iron concentrations (≥ 1 M), as would be found in ICRFB electrolytes. However, this method might be suitable by adding small amounts of semi-reactive ligand additives to the electrolyte to selectively create desired absorption bands that could help quantify iron, or other, species.

3.1.2.3 Chemiluminescence

Another method often used to measure iron in water bodies is chemiluminescence. A chemical reaction is used to induce the emission of light, which can then be measured with photon counters or luminometers, where the number of photons is proportional to the concentration of the reacting species. Accordingly, this method resides under emission spectroscopy. A major advantage of this method is that the instrumentation required is rudimentary as it does not require an external light source. In addition, the instrument also does not require wavelength selectors.[24]

Trace amounts of Fe^{2+} can be analysed with this technique using luminol (Figure 14), which reacts with the Fe^{2+} in solution and emits light with a nonlinear relationship to its concentration.[77] While higher concentrations of iron could also be measured by this technique, the addition of luminol would not be suitable for in-line battery electrolyte monitoring. Nevertheless, this method could still be used for iron redox speciation analysis due its simplicity, considering that the total iron content would have to be determined using a different technique.

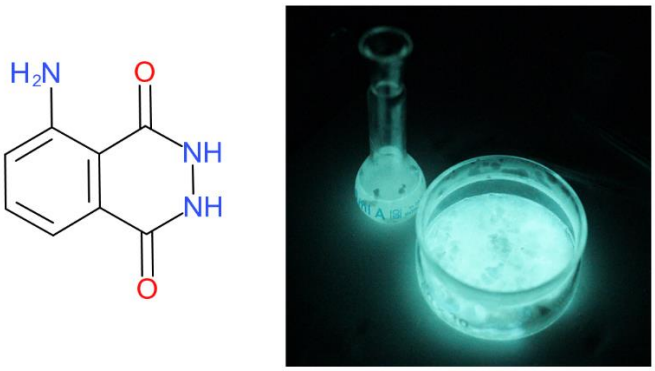

Figure 14: Luminol and the chemiluminescence induced when it reacts with oxygen from atmosphere and carbamide peroxide.[71]

3.2 Effect of impurities on electrolyte performance

As this study aims to purify and analyse $FeCl_2$ to be used in an ICRFB, the effect of the impurities on performance and the type of impurities influencing electrolyte performance were reviewed and summarised in this section.

3.2.1 Effect of impurities

As previously stated, limited research is available on the effect of impurities on the performance of an ICRFB. It is, however, still useful to review the effects of impurities on the performance of an VRFB, showing their negative side-effects, which should be considered when purifying an iron solution to be used as an ICRFB electrolyte.

It was mentioned that the HER at the negative electrode (see Section 2.3.2.2) causes imbalance between electrolytes both in the ICRFB and the VRFB. Metal impurities in the negative electrolyte that could be deposited on the negative electrode through electroplating, could not only directly contribute towards imbalance due to electroplating, but could also produce a surface that favours and catalyses the HER. When studying the effects of copper impurities on VRFB performance, an accelerated HER was observed at the negative electrolyte after only three cycles with copper concentrations as low as 50 ppm.[60] In Figure 15, the direct, and largely linear, relation between the copper content (0 – 200 ppm) and the HER rate is shown. It is thus clear that high levels of copper would have a devastating effect on electrolyte performance and should therefore be monitored carefully.

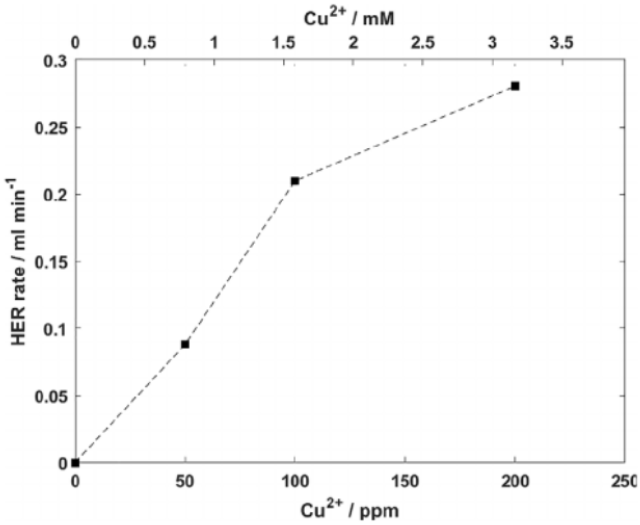

Figure 15: Hydrogen production with varying copper contamination concentrations for the VRFB.[60]

The effect of many other metal impurities, including Li^+, Na^+, K^+, Mg^{2+}, Cr^{3+}, Mn^{2+}, Fe^{2+}, Fe^{3+}, Co^{2+}, Ni^{2+}, Zn^{2+}, Mo^{6+} and Sn^{2+} on VRFB electrolyte performance has been investigated.[78-79] The presence of only 0.005 M Li^+, Cr^{3+} or Ni^{2+} in the electrolyte retarded the kinetics of the redox reaction in the negative electrolyte (V^{2+}/V^{3+}). Metals that had no noticeable effect were Na^+ and Mg^{2+}. Metals that promoted the HER were Sn^{2+} and Ni^{2+} (as low as 0.001 M), while

Mo^{6+} produced sediment formation in electrolytes. Additionally, Sn^{2+} also had detrimental effects on the negative electrolyte reactions by increasing the activation overpotential and reducing voltage efficiency. The other remaining impurities (at ≥ 0.1 M) resulted in a decreased diffusion rate of the V^{3+} ions, which negatively affected the peak current at the negative electrode.[78-79]

Although literature results on the effects of impurities on VRFB performance vary somewhat for certain species, some metals stand out more as potentially harmful to RFB performance. Accordingly, the metals Cu^{2+}, Ni^{2+} and Sn^{2+} all seem to promote the HER at the negative electrode, which will increase electrolyte imbalance. Other metals that had a negative effect on the negative electrolyte's redox reaction might only be specific to V^{2+}/V^{3+}, while not affecting Cr^{2+}/Cr^{3+}, but this would have to be determined since the reaction kinetics and chemical reactions are so different. Obviously, Fe^{2+}/Fe^{3+} and Cr^{3+} would not be considered impurities in an ICRFB electrolyte, in spite of the side reactions they could cause.

3.2.2 Impurities of concern

While no literature could be found on the effects of impurities on ICRFB performance, VRFB research might again give insight into impurities that could have similar negative effects in an ICRFB. For example, both systems suffer from the effect of the HER on the negative electrode, resulting from the acidic aqueous electrolytes accompanied by the potential at the negative electrode. Both the VRFB and ICRFB generally use Nafion membranes to separate the two redox-couples and hence the different metallic species in solution. Apart from the chemical differences of the electrolytes, the activity of impurities at a similar concentration in both batteries, could theoretically be higher for the ICRFB due to its higher operating temperatures (65 °C), showing the importance of determining the effect that these might have on ICRFB performance.

It is clear that, when attempting to purify a low cost $FeCl_2$, it is likely to contain high amounts of impurities related to the mining of the iron ore. The metals often present in iron ore at concentrations exceeding 1% are Zn, Pb and Al. Other metals such as Mg, Mn, Cu, Ni, Co, V, Sn and Cd may also be present in smaller amounts, depending on the location of origin of the ore.[80-83] Some other unlisted metals that might be present in low ppm ranges may still be detrimental to the performance of the RFB.[60] From the research on VRFB, it seems that Cu^{2+}, Ni^{2+} and Sn^{2+} should definitely be removed if present, but unfortunately, as mentioned previously, there is limited research on the effects of impurities on the performance on RFB electrolytes, even for the well-researched VRFB.[79] Consequently, the range of metal impurities

to be analysed before and after $FeCl_2$ purification should be as wide as possible, while special attention should be paid to those that may promote the HER.

4. Beer-Lambert law

Since the Beer-Lambert law is the most important law in optical spectroscopy and the basis of the analysis technique developed in this study, an overview of the history is briefly given in this section.

The Beer-Lambert law, also known as the Bouguer-Beer-Lambert law, was originally developed by Pierre Bouguer around 1729 when he described the path length of a sample and how it affected absorbance of light. The law was later improved by Johann Heinrich Lambert, working in the field of spectrophotometry in 1852, and August Beer, who published a book in 1854 when working on the spectrophotometry of the atmosphere. The law was described by Beer as the loss of intensity of light through infinitely thin layers of a homogeneous medium, with a loss that is proportional to the intensity and thickness of the layers.[84] This led to a differential equation from Bouguer that was put in mathematical form by Lambert as:

$$I(d) = I_0 \cdot \exp(-\alpha d) \tag{14}$$

where α is the Napierian constant, I_0 is the light's initial intensity and $I(d)$ the light's intensity after it has travelled through the medium with a distance d. Later, in 1857, Bunsen and Roscoe expressed the equation in terms of absorptivity (a):

$$a = \frac{1}{d}\log_{10}\left(\frac{I_0}{I}\right) \tag{15}$$

In the following years, the absorption law was expressed in various forms, but Luther published a paper in 1913 that merged the Bouguer-Lambert and Beer law into an expression of absorption A:

$$\log_{10}\left(\frac{I_0}{I}\right) = A = \varepsilon \cdot c \cdot d \tag{16}$$

where the molar absorption coefficient ε was introduced with sample concentration c (mol dm^{-3}) as $\varepsilon \cdot c = a$.

In spite of its importance, there are limitations to the Beer-Lambert law, since the absorption in reality is not as exact and simple as portrayed in Equation (16).[84] For example, effects such

as wave interference of light may change absorption values without any physical changes in the sample. As a result, the law is nowadays used as an accurate approximation and not as factually accurate.[84] Absorbance today is commonly expressed as:

$$A = \varepsilon bc \tag{17}$$

The old nomenclature used before and during the 1900s was gradually replaced, and the Society for Applied Spectroscopy and the American Chemical Society agreed on modern terms, symbols, and definitions where $\mathcal{E}$, and *b,* were defined as molar absorptivity and path length of the sample expressed in mol^{-1} dm^3 cm^{-1} and cm, respectively. Equation (17) is used today to experimentally determine the molar absorptivity of radiation by chemical species of known concentrations.

5. Conclusion

The ICRFB shows great potential, thanks to modern membrane technology, as a LESS that may provide stability in rural and industrial environments in South Africa. Additionally, it has the potential as a LESS that can globally solve the mismatch between the intermittency of renewable energy sources and the constant electricity demand which will become more prevalent as we transition to using renewable sources. However, this LESS requires economically viable electrolyte materials, electrolyte rebalancing and methods to monitor electrolyte imbalance/SOC/SOH to reach its full potential. Factors like impurities in electrolytes, electrolyte imbalance and the HER still need to be addressed. After considering factors like impurities, purification techniques, the importance, and the chemistry of iron, a possible solution was obtained for economical electrolyte sources. Low-cost uncomplicated techniques such as cementation and fractional crystallisation enable the removal of impurities from cheaper $FeCl_2$ sources, which allows large-scale research or applications to operate with less expense. Analysing metal impurities, even at very low concentrations (ppb), should easily be achieved using ICP-OES. However, analysing the Fe^{2+}/Fe^{3+} content of an electrolyte produced with these methods require a specialised analytical method, which would also serve as a solution to monitoring electrolyte imbalance as Fe^{3+}. From VRFB research and iron analysis techniques, possible methods of analysis were reviewed and considered, with spectroscopic methods like UV-Vis spectrophotometry being the most suitable since its application is non-destructive and allows for in-line analysis. Furthermore, it is clear that an electrolyte analysing/monitoring method should be developed using this analytical technique together with the Beer-Lambert law to allow accurate analysis of both dissolved species of iron in the ICRFB electrolyte.

6. References

1. Suman, A., Role of renewable energy technologies in climate change adaptation and mitigation: A brief review from Nepal. *Renewable and Sustainable Energy Reviews* **2021,** *151*, 111524.
2. Menyah, K.; Wolde-Rufael, Y., CO2 emissions, nuclear energy, renewable energy and economic growth in the US. *Energy Policy* **2010,** *38* (6), 2911-2915.
3. Höök, M.; Tang, X., Depletion of fossil fuels and anthropogenic climate change—A review. *Energy Policy* **2013,** *52*, 797-809.
4. Ding, C.; Zhang, H.; Li, X.; Liu, T.; Xing, F., Vanadium Flow Battery for Energy Storage: Prospects and Challenges. *The Journal of Physical Chemistry Letters* **2013,** *4*.
5. Wei, W.; Qingtao, L.; Bin, L.; Xiaoliang, W.; Liyu, L.; Zhenguo, Y., Recent Progress in Redox Flow Battery Research and Development. *Advanced Functional Materials* **2013,** *23* (8), 970-986.
6. Li, L.; Kim, S.; Wang, W.; Vijayakumar, M.; Nie, Z.; Chen, B.; Zhang, J.; Xia, G.; Hu, J.; Graff, G.; Liu, J.; Yang, Z., A Stable Vanadium Redox-Flow Battery with High Energy Density for Large-Scale Energy Storage. *Advanced Energy Materials* **2011,** *1*.
7. Chen, R.; Kim, S.; Chang, Z., Redox Flow Batteries: Fundamentals and Applications [open access]. 2017; pp 103-118.
8. Darling, R. M.; Gallagher, K. G.; Kowalski, J. A.; Ha, S.; Brushett, F. R., Pathways to low-cost electrochemical energy storage: A comparison of aqueous and nonaqueous flow batteries. *Energy and Environmental Science* **2014,** *7* (11), 3459-3477.
9. Weber, A. Z.; Mench, M. M.; Meyers, J. P.; Ross, P. N.; Gostick, J. T.; Liu, Q., Redox flow batteries: a review. *Journal of Applied Electrochemistry* **2011,** *41* (10), 1137-1164.
10. Connolly, D. A Review of Energy Storage Technologies *For the integration of fluctuating renewable energy*. University of Limerick, 2009.
11. Zeng, Y. K.; Zhao, T. S.; An, L.; Zhou, X. L.; Wei, L., A comparative study of all-vanadium and iron-chromium redox flow batteries for large-scale energy storage. *Journal of Power Sources* **2015,** *300*, 438-443.
12. Chen, T.; Jin, Y.; Lv, H.; Yang, A.; Liu, M.; Chen, B.; Xie, Y.; Chen, Q., Applications of Lithium-Ion Batteries in Grid-Scale Energy Storage Systems. *Transactions of Tianjin University* **2020,** *26* (3), 208-217.
13. de Oliveira, M. C. L.; Antunes, R. A., Bipolar Plates in Redox Flow Batteries, Fuel Cells and Electrolyzers. In *Reference Module in Earth Systems and Environmental Sciences*, Elsevier: 2021.

14. Skyllas-Kazacos, M.; Rychcik, M.; Robins, R. G.; Fane, A. G., New All-Vanadium Redox Flow Cell. *Journal of The Electrochemical Society* **1986,** *133*.
15. Lourenssen, K.; Williams, J.; Ahmadpour, F.; Clemmer, R.; Tasnim, S., Vanadium redox flow batteries: A comprehensive review. *Journal of Energy Storage* **2019,** *25*, 100844.
16. Michos, I.; Cao, Z.; xu, Z.; Jing, W.; Dong, J., Investigations on a Mesoporous Glass Membrane as Ion Separator for a Redox Flow Battery. *Batteries* **2019,** *5*, 6.
17. Struckmann, T.; Kuhn, P.; Ressel, S., A combined in situ monitoring approach for half cell state of charge and state of health of vanadium redox flow batteries. *Electrochimica Acta* **2020,** *362*, 137174.
18. Corcuera, S.; Skyllas-Kazacos, M., State-of-Charge Monitoring and Electrolyte Rebalancing Methods for the Vanadium Redox Flow Battery. *European Chemical Buletin* **2012,** *1*, 511-519.
19. Shin, K.-H.; Jin, C.-S.; So, J.-Y.; Park, S.-K.; Kim, D.-H.; Yeon, S.-H., Real-time monitoring of the state of charge (SOC) in vanadium redox-flow batteries using UV–Vis spectroscopy in operando mode. *Journal of Energy Storage* **2020,** *27*, 101066.
20. Skyllas-Kazacos, M.; Kazacos, M., State of charge monitoring methods for vanadium redox flow battery control. *Journal of Power Sources* **2011,** *196* (20), 8822-8827.
21. Zhang, W.; Liu, L.; Liu, L., An on-line spectroscopic monitoring system for the electrolytes in vanadium redox flow batteries. *RSC Advances* **2015,** *5* (121), 100235-100243.
22. Tang, A.; Bao, J.; Skyllas-Kazacos, M., Dynamic modelling of the effects of ion diffusion and side reactions on the capacity loss for vanadium redox flow battery. *Journal of Power Sources* **2011,** *196* (24), 10737-10747.
23. Tong, S.; Klein, M. P.; Park, J. W., On-line optimization of battery open circuit voltage for improved state-of-charge and state-of-health estimation. *Journal of Power Sources* **2015,** *293*, 416-428.
24. Skoog, D. A.; West, D. M.; Holler, F. J.; Crouch, S. R., *Fundamentals of analytical chemistry*. Ninth ed.; Brooks/Cole: 2014.
25. Haisch, T.; Ji, H.; Weidlich, C., Monitoring the state of charge of all-vanadium redox flow batteries to identify crossover of electrolyte. *Electrochimica Acta* **2020,** *336*, 135573.
26. Skyllas-Kazacos, M.; Maddern, B. G.; Kazacos, M.; Joy, J. State of charge of redox cell. June, 1989.
27. Pawar, S. H.; Madhale, R. D.; Patil, P. S.; Lokhande, C. D., Studies on iron-chromium redox storage system. *Bulletin of Materials Science* **1988,** *10* (4), 367-372.

28. Vinco, J. H.; Domingos, A. E. E. d. C.; Espinosa, D. C. R.; Tenório, J. A. S.; Baltazar, M. d. P. G., Unfolding the Vanadium Redox Flow Batteries: An indeep perspective on its components and current operation challenges. *Journal of Energy Storage* **2021,** *43*, 103180.
29. Thaller, L. H., Electrically Rechargable Redox Flow Cells. In *Ninth Intersociety Energy Conversion Engineering conference*, San Fransisco, California, 1974.
30. Johnson, D. A.; Reid, M. A., Chemical and Electrochemical Behavior of the Cr(III)/Cr(II) Half-Cell in the Iron-Chromium Redox Energy Storage System. *Journal of The Electrochemical Society* **1985,** *132* (5), 1058-1062.
31. Johnson, D. A.; Reid, M. A. *Chemical and Electrochemical Behaviour of the Cr(III)/Cr(II) Half Cell in the NASA Redox Energy Storage System*; Spring Arbor College, Spring Arbor, Michigan 49283.

National Aeronautics and Space Administration, Lewis Research Center, Cleveland, Ohio 44135: 1982.

32. Gann, R. F.; Hagedorn, N. H.; Ling, J. S. *Single Cell Performance Studies on the Fe/Cr Redox Energy Storage System Using Mixed Reactant Solutions at Elevated Temperature*; NASA Lewis Research Center Cleveland, OH, United States: 1983.
33. Hagedorn, N. H. *NASA Redox Storage System Development Project. Final Report*; National Aeronautics and Space Administration, Cleveland, OH (USA). Lewis Research Center: 1984.
34. Gann, R. F.; Hagedorn, N. H.; Johnson, J. A. *Cycling Performance of the Iron-Chromium Redox Energy Storage System*; NASA TM-87034; NASA Lewis Research Center Cleveland, OH, United States: 1985.
35. Ling, J. S.; Charleston, J. *Advances in Membrane Technology for the NASA Redox Energy Storage System*; NASA TM-82701; NASA Lewis Research Center Cleveland, OH, United States: 1980.
36. Hagedorn, N. H. *Nasa redox storage system development project*; NAS 1.15:83677; National Aeronautics and Space Administration, Cleveland, OH (USA). Lewis Research Center: 1984.
37. Pham, T. A.; Koo, S.; Park, H.; Luong, Q. T.; Kwon, O. J.; Jang, S.; Kim, S. M.; Kim, K., Investigation on the Microscopic/Macroscopic Mechanical Properties of a Thermally Annealed Nafion® Membrane. *Polymers* **2021,** *13* (*22*).
38. Sun, C.; Zhang, H., Review of the Development of First-Generation Redox Flow Batteries: Iron-Chromium System. *ChemSusChem* **2021,** *15* (1), 15.

39. Jiang, B.; Wu, L.; Yu, L.; Qiu, X.; Xi, J., A comparative study of Nafion series membranes for vanadium redox flow batteries. *Journal of Membrane Science* **2016,** *510*, 18-26.
40. Shah, A.; Ralph, T.; Walsh, F., Modeling and Simulation of the Degradation of Perfluorinated Ion-Exchange Membranes in PEM Fuel Cells. *Journal of The Electrochemical Society - J ELECTROCHEM SOC* **2009,** *156*.
41. Zeng, Y. K.; Zhou, X. L.; An, L.; Wei, L.; Zhao, T. S., A high-performance flow-field structured iron-chromium redox flow battery. *Journal of Power Sources* **2016,** *324*, 738-744.
42. Zhang, H.; Tan, Y.; Li, J.; Xue, B., Studies on properties of rayon- and polyacrylonitrile-based graphite felt electrodes affecting Fe/Cr redox flow battery performance. *Electrochimica Acta* **2017,** *248*, 603-613.
43. Fares, A. I.; Sohel, K. M. A.; Al-Jabri, K.; Al-Mamun, A., Characteristics of ferrochrome slag aggregate and its uses as a green material in concrete – A review. *Construction and Building Materials* **2021,** *294*, 123552.
44. Ren, S.; Li, H.; Wang, Y.; Guo, C.; Feng, S.; Wang, X., Comparative study of the China and U.S. import trade structure based on the global chromium ore trade network. *Resources Policy* **2021,** *73*, 102198.
45. Stibbs, J.; Liu, S. https://www.metalbulletin.com/Article/5085229/UG2MG-chrome-ore-price-jumps-17t-to-44-month-high.html (accessed 02-22).
46. Cramer, L.; Basson, J.; Nelson, L., The impact of platinum production from UG2 ore on ferrochrome production in South Africa. *Journal of The South African Institute of Mining and Metallurgy* **2004,** *104*, 517-527.
47. https://markets.ft.com/data/commodities/tearsheet/summary?c=Iron+ore (accessed 02-22).
48. Wang, W.; Nie, Z.; Chen, B.; Chen, F.; Luo, Q.; Wei, X.; Xia, G.; Skyllas-Kazacos, M.; Li, L.; Yang, Z., A New Fe/V Redox Flow Battery Using a Sulfuric/Chloric Mixed-Acid Supporting Electrolyte. *Advanced Energy Materials* **2012,** *2* (4), 487-493.
49. Thaller, L. H. *Recent advances in Redox Flow Cell Storage Systems*; NASATM-79186; NASA Lewis Research Center Cleveland, OH, United States: 1979.
50. Miao, F.; Huang, Y., Study on composite optics properties of FeCl2·4H2O crystal in material engineering. In *Advanced Materials Research*, 2012; Vol. 583, pp 187-190.
51. Jameel, P., The use of ferrous chloride to control dissolved sulfides in interceptor sewers. *Journal of the Water Pollution Control Federation* **1989,** *61* (2), 230-236.
52. Ning, J.; Zheng, Y.; Brown, B.; Young, D.; Nesic, S., A Thermodynamic Model for the Prediction of Mild Steel Corrosion Products in an Aqueous Hydrogen Sulfide Environment. *Corrosion* **2015,** *71*, 150504075113003.

53. Petrucci, R. H.; Harwood, W. S.; Herring, G. F.; Madura, J. D., *General chemistry : principles and modern applications*. Pearson Prentice Hall: Upper Saddle River; New Jersey, 2007.
54. Curtolo, C. D.; Rodriguez-Rojas, M. J.; Friedrich, S.; Friedrich, B., Alternative fractional crystallization-based methods to produce high-purity aluminum. *Journal of Materials Research and Technology* **2021,** *12*, 796-806.
55. Joachim, U., The Crystallization Technology Handbook, 2nd ed Edited by Marcel Dekker: . In *Crystal Growth & Design*, A. Marsmann, Ed. American Chemical Society: New York, Basel, 2001; pp 25-44 & 439-581.
56. Gayer, K. H.; Wootner, L., The Hydrolysis of Ferrous Chloride at 25°1. *Journal of the American Chemical Society* **1956,** *78* (16), 3944-3946.
57. Agrawal, M. L.; Kapoor, R. D., Theoretical considerations on the cementation of copper with iron. *Journal of the Southern African Institute of Mining and Metallurgy* **1982,** *82* (4), 106-111.
58. Free, M. L., *Hydrometallurgy Fundamentals and Applications*. 2 ed.; Springer, Cham: 2022; p 458.
59. Saylam, H. In *Deposition of cobalt on iron powder*, 1982.
60. Reynard, D.; Vrubel, H.; Dennison, C. R.; Battistel, A.; Girault, H., On-Site Purification of Copper-Contaminated Vanadium Electrolytes by using a Vanadium Redox Flow Battery. *ChemSusChem* **2019,** *12* (Issue 6), 1222-1228.
61. Dinardo, O.; Kondos, P. D.; MacKinnon, D. J.; McCready, R. G. L.; Riveros, P. A.; Skaff, M. *Study on metals recovery/recycling from acid mine drainage*; Canada Centre for Mineral and Energy Technology, Ottawa, ON (Canada): 555 Booth Street, Ottawa, Ontario, 1991.
62. Pohl, P.; Prusisz, B., Redox speciation of iron in waters by resin-based column chromatography. *TrAC Trends in Analytical Chemistry* **2006,** *25* (9), 909-916.
63. Wolle, M. M.; Fahrenholz, T.; Rahman, G. M. M.; Pamuku, M.; Kingston, H. M. S.; Browne, D., Method development for the redox speciation analysis of iron by ion chromatography–inductively coupled plasma mass spectrometry and carryover assessment using isotopically labeled analyte analogues. *Journal of Chromatography A* **2014,** *1347*, 96-103.
64. Achterberg, E. P.; Holland, T. W.; Bowie, A. R.; Fauzi, R.; Mantoura, C.; Worsfold, P. J., Determination of iron in seawater. *Analytica Chimica acta* **2001,** *442* (1), p 1-14.
65. Skoog, D. A.; West, D. M.; Holler, F. J.; Crouch, S. R., *Fundamentals of analytical chemistry*. Ninth edition. ed.; Brooks/Cole, Cengage Learning: Belmont, CA, 2014; p p 773-790.

66. Jakubowski, N.; Moens, L.; Vanhaecke, F., Sector field mass spectrometers in ICP-MS. *Spectrochimica Acta Part B: Atomic Spectroscopy* **1998,** *53* (13), 1739-1763.
67. Solovyev, N.; Vinceti, M.; Grill, P.; Mandrioli, J.; Michalke, B., Redox speciation of iron, manganese, and copper in cerebrospinal fluid by strong cation exchange chromatography – sector field inductively coupled plasma mass spectrometry. *Analytica Chimica Acta* **2017,** *973*, 25-33.
68. Yan, X.-P.; Hendry, M. J.; Kerrich, R., Speciation of Dissolved Iron(III) and Iron(II) in Water by On-Line Coupling of Flow Injection Separation and Preconcentration with Inductively Coupled Plasma Mass Spectrometry. *Analytical Chemistry* **2000,** *72* (8), 1879-1884.
69. Pavia, D. L.; Lampman, G. M.; Kriz, G. S.; Vyvyan, J. R., *Introduction to spectroscopy*. 4 ed.; 2009, 2001 Brooks/Cole, Cengage Learning: 2009; p 381-413.
70. Skoog, D. A.; West, D. M.; Holler, F. J.; Crouch, S. R., *Fundamentals of analytical chemistry*. Ninth edition. ed.; Brooks/Cole, Cengage Learning: Belmont, CA, 2014; p 658-674 & 722-738.
71. https://sudonull.com/post/125415-Chemiluminescence-of-luminol-whats-inside-the-glow-sticks (accessed 02-23).
72. Smith, G. L.; Reutovich, A. A.; Srivastava, A. K.; Reichard, R. E.; Welsh, C. H.; Melman, A.; Bou-Abdallah, F., Complexation of ferrous ions by ferrozine, 2,2′-bipyridine and 1,10-phenanthroline: Implication for the quantification of iron in biological systems. *Journal of Inorganic Biochemistry* **2021,** *220*, 111460.
73. Lin, M.; Hu, X.; Pan, D.; Han, H., Determination of iron in seawater: From the laboratory to in situ measurements. *Talanta* **2018,** *188*, 135-144.
74. Jones, M. R.; Lee, K., Sequential injection analysis Ferrozine spectrophotometry versus Luminol chemiluminescence for continuous online monitoring of the concentration and speciation of iron. *Microchemical Journal* **2020,** *157*, 104881.
75. Chen, L.; Xu, J.; Wang, T.; Huang, Y.; Yuan, D.; Gong, Z., Toward a versatile flow technique: Development and application of reverse flow dual-injection analysis (rFDIA) for determining dissolved iron redox species and soluble reactive phosphorus in seawater. *Talanta* **2021,** *232*, 122404.
76. Jeitner, T. M., Optimized ferrozine-based assay for dissolved iron. *Analytical Biochemistry* **2014,** *454*, 36-37.
77. Bolster, K.; Heller, M.; Moffett, J., Determination of iron(II) by chemiluminescence using masking ligands to distinguish interferences. *Limnology and Oceanography: Methods* **2018,** *16*, 10.

78. Cao, L.; Skyllas-Kazacos, M.; Menictas, C.; Noack, J., A review of electrolyte additives and impurities in vanadium redox flow batteries. *Journal of Energy Chemistry* **2018,** *27* (5), 1269-1291.
79. Park, J. H.; Park, J. J.; Lee, H. J.; Min, B. S.; Yang, A., Influence of Metal Impurities or Additives in the Electrolyte of a Vanadium Redox Flow Battery. *Journal of The Electrochemical Society* **2018,** *165* (7), A1263-A1268.
80. Lau, L. L.; Strezov, V.; Gonçalves, M. V. B.; Bagatini, M. C., Trace elements emission in iron ore sintering: A review. *Environmental Advances* **2021,** *6*, 100123.
81. da Silva, F. L.; Araújo, F. G. S.; Teixeira, M. P.; Gomes, R. C.; von Krüger, F. L., Study of the recovery and recycling of tailings from the concentration of iron ore for the production of ceramic. *Ceramics International* **2014,** *40* (10, Part B), 16085-16089.
82. Muwanguzi, A. J. B.; Karasev, A. V.; Byaruhanga, J. K.; Jönsson, P. G., Characterization of Chemical Composition and Microstructure of Natural Iron Ore from Muko Deposits. *ISRN Materials Science* **2012,** *2012*, 174803.
83. Mustafa, S.; Luo, L.; Zheng, B.-T.; Wei, C.-X.; Niyonzima, J. C., Effect of Lead and Zinc Impurities in Ironmaking and the Corresponding Removal Methods: A Review. *Journal of Metals* **2021,** *Volume 11*, 1-19.
84. Mayerhöfer, T. G.; Pahlow, S.; Popp, J., The Bouguer-Beer-Lambert Law: Shining Light on the Obscure. *ChemPhysChem* **2020,** *21* (18), 2029-2046.

CHAPTER 3

Purifying $FeCl_2$ as an economical alternative source for ICRFB electrolyte synthesis

Johannes Petrus du Toit, Henning Manfred Krieg, Nico Mans, Derik Jacobus van der Westhuizen.

Abstract

The iron-chrome redox flow battery (ICRFB) is an electrochemical energy storage technology with significant potential to become a large-scale energy storage solution (LESS), due to the abundance of iron and chrome used for its electrolyte. However, although this LESS has significant potential, it requires further development, which in turn will require large quantities of electrolyte. Unfortunately, the electrolytes currently have short lifetimes, as rectifying capacity decay from electrolyte imbalance remains a challenge. As a result, discarding electrolytes made from commercially available lab-grade chemicals such as $FeCl_2$ increase the running costs. This study covers the development of an inexpensive and uncomplicated procedure, to purify unrefined $FeCl_2$ originally intended for industrial applications by combining fractional crystallisation with cementation. Using said purification procedure the degree of contamination was reduced by removing, amongst others, 81.3% Cu, 70.5% Ni and 62.7% Sn, that all could contribute to undesired side reactions such as the hydrogen evolution reaction (HER). It was finally shown that the electrolyte obtained from the purification of the unrefined source of $FeCl_2$ performed on par with commercially available lab-grade $FeCl_2$ in an ICRFB.

Keywords: Iron-chromium redox flow batteries, Electrolyte purification, Electrolyte testing, Low-cost energy storage, Impurities

1. Introduction

As the inevitable global transition towards renewable energy sources becomes ever more relevant, so does the need for capable large-scale energy storage solutions (LESSs).[1-3] Redox flow batteries (RFBs) show significant potential for use as LESSs, considering the low cost and ease of upscaling offered by this technology.[4-5] Since the supply and availability of the elements used as the redox pair are vital when considering up-scaling, the iron-chromium RFB (ICRFB) is a particularly attractive LESS requiring metals that are both inexpensive as well as abundant.[6-8]

Although the calculated cost for the ICRFB electrolyte is relatively low, most laboratory-scale tests on ICRFB systems are conducted with commercial and often expensive electrolytes. This is understandable, since laboratory tests require repeatable and causal results to reduce variations in performance that could stem from varying factors such as the membrane, current and voltage, or the electrolyte. Hence, the electrolyte has to be prepared from high quality and pure precursor chemicals to prohibit impurities and/or composition differences from affecting battery performance.[9-10] For this reason, electrolytes for laboratory use are usually bought from chemical suppliers at a high cost. However, upscaling RFBs from demo to LESS applications are required,[5-6,11] leading to the larger amounts of electrolyte required, which would lead to excessive costs when prepared from the aforementioned lab-grade chemicals. Obviously, such upscaling would have to occur without compromising the quality of the electrolyte. An additional disadvantage of the ICRFB compared to the VRFB is that the ICRFB electrolyte becomes imbalanced rather quickly, leading to a build-up of ferric iron (Fe^{3+}) either caused by imbalance reactions during battery cycling or via oxygen intrusion.

For these two reasons, larger-scale experiments on ICRFB are currently expensive, not only because of the initial cost of the electrolyte, but also due to the significant amount of electrolyte that has to be discarded after only a few cycles due to imbalance. Hence, obtaining a less expensive alternative to the currently used laboratory grade $FeCl_2$ salts would be beneficial, but would require an alternative low-cost purification technique. One possible option could entail cementation with, for example, Fe metal, which could provide a low-cost alternative by removing those metal impurities that have higher reduction potentials, such as Cu and Ni, from the electrolyte.[12-13] However, while electrolyte purity and impurity removal, as well as their impact on performance, have received significant attention in the field of the all-vanadium RFB (VRFB), [9,14-15] there is a gap in ICRFB research, as impurities and purification regarding electrolytes have yet to be addressed.

Consequently, the aim of this study was to determine whether less expensive and unrefined $FeCl_2$ could be purified to provide an ICRFB electrolyte with a reduced cost. To achieve this, an inexpensive and simple purification process was developed combining cementation and fractional crystallisation. Finally, the purified low-grade $FeCl_2$ electrolyte was tested in an ICRFB and compared to the existing lab-grade electrolyte.

2. Materials and methods

2.1 Ferrous chloride

Metsep SE (Pty) LTD supplied 100 L of a low-grade $FeCl_2$ as an acidic solution containing 12-14% total iron with a minimum of 10% as Fe^{2+}. This $FeCl_2$ solution is currently used both in sewage treatment, hydrometallurgy for heavy metal removal, industrial effluent treatment and reduction of Cr^{6+}.[16] A sample was provided for this study as the $FeCl_2$ solution is currently only sold in bulk (~30 tons). Due to the low cost, this solution was deemed suitable for developing a low-cost and simple purification technique to reduce the electrolyte cost for large-scale ICRFB applications. The low-grade, low-cost $FeCl_2$ solution that was purified during this study will be referred to as unrefined $FeCl_2$. For comparison, a pure $FeCl_2$ (purity ≥ 99.0%) was obtained from Sigma-Aldrich (Merck). This will be referred to as commercial and lab-grade. The Fe powder used for the cementation was obtained from Sigma-Aldrich (Merck) (purity ≥ 99%).

2.2 Purification procedure

Based on an extensive literature survey (see Literature review - Section 3.1.1), as well as consideration of available equipment and various lab-scale tests, a purification procedure was devised using 475 mL of the unrefined solution (174.5 g L^{-1} Fe). This volume was chosen as a proof-of-concept experiment with the purpose of identifying possible challenges with this procedure. This led to certain experimental adjustments for both safety reasons and ease of processing. The method entailed taking 475 mL from the 100 L bulk and putting it into a 500 mL beaker, adding boiling stones and bubbling the solution with N_2 for one hour. The solution was then heated to a boiling point of 106 °C (at 0.938 atm). After the solvent had boiled off to a solution volume of 260 mL, 10 g fine Fe powder and 13 mL HCl (32 %, Labchem) were slowly added. The solution was then left to cool in an ice bath where hydrous, light green, $FeCl_2$ visibly started to precipitate. Ten minutes after precipitation started, the contents of the

beaker were vacuum filtered and washed with ice cold MilliQ-water (0.055 $\mu S.cm^{-1}$). The wet crystals were stored overnight in a sealed and N_2-flushed glass bottle.

For the upscaling of the purification process, 2 x 4 L of the bulk $FeCl_2$ solution were simultaneously treated, which was repeated 5 times to obtain a total treatment volume of 40 L. For each repetition, 8 L (2 x 4 L) of the unrefined FeCl2 solution was removed from the 100 L bulk, thoroughly mixed, and placed into 5 L glass flasks. The same procedure was followed as that of the small-scale experiment, where boiling stones were added and N_2 was bubbled. The unrefined $FeCl_2$ solutions took much longer to concentrate to a near-saturated Fe concentration, while heated under a nitrogen blanket to prohibit Fe^{2+} oxidation. As the concentrations of the solutions increased, the boiling point increased, requiring additional heating. After boiling for ± 2.5 h, the solutions had reached 119 °C, while the total volume of each container had been reduced to 2.5 L. To allow cementation (see Literature review - Section 3.1.1.2) of the impurities, while simultaneously reducing any built-up Fe^{3+} to Fe^{2+}, 102.5 mL HCl (32 %, Labchem) and 70 g of fine Fe metal powder (≥99%, Merck) were added to the concentrated $FeCl_2$ solution, while sustaining a temperature above 95 °C.

After most of the Fe had reacted, confirmed by the cessation of boiling, the solutions were stirred for an additional 30 minutes with a magnetic stirrer. After stirring, any solid impurities (including cemented metals) and unreacted iron powder were filtered from the hot solutions (~105 °C) by means of vacuum filtration, using a highly porous acid- and temperature-resistant polyester cloth filter (pore size >10 µm). After filtration, the solutions were poured into 20 L high density polyethylene (HDPE) containers that had been adequately flushed with N_2 prior to the addition of the solutions. It is important to note that this step was performed immediately after filtration to prohibit loss of product via precipitation since the solutions were at saturation point. To allow crystallisation of hydrous $FeCl_2$, the vessels were left overnight (at temperatures 2-10 °C). The formed crystals were filtered using the same vacuum filtration method as discussed above, before being washed using ice cold MilliQ-water (0.055 $\mu S\ cm^{-1}$). The wet crystals were then moved and sealed in N_2-flushed HDPE containers.

2.3 Analysis of $FeCl_2 \cdot xH_2O$

ICP-OES (Agilent Technologies 5110) was used to accurately determine the water content of the hydrated $FeCl_2$ crystals and ICP-MS (analysis done by SUN-CAF) was used to measure impurities in the unrefined $FeCl_2$ before and after purification (see Table 2 for detection limits and accuracy). Firstly, the Fe concentration of the unrefined $FeCl_2$ solution was determined using ICP-OES analysis. For this analysis, a sample of the unrefined $FeCl_2$ was prepared by

diluting it by a factor of 100 in 1.0 M HCl (diluted from 32 %, Labchem). The water and Fe content of the purified $FeCl_2$ was determined by dissolving 4.813 g $FeCl_2 \cdot xH_2O$ in 100 mL 1.0 M HCl and diluting it 1000 times. Subsequently, the impurities were determined by preparing 1.3 M Fe solutions from both the unrefined and purified $FeCl_2$ solutions. After diluting 500 times using 1.0 M HCl, the samples were sent for ICP-MS analysis.

Table 2: ICP-MS detection limits and accuracy on internal QC, for all measured impurities

	B $\mu g\ L^{-1}$	**Al** $\mu g\ L^{-1}$	**Si** $\mu g\ L^{-1}$	**V** $ng\ L^{-1}$	**Cr** $ng\ L^{-1}$	**Mn** $ng\ L^{-1}$	**Fe** $mg\ L^{-1}$	**Co** $ng\ L^{-1}$
LOQ	50.00	0.5687	5.573	5.431	95.15	77.80	1.535	44.37
% Accuracy on internal QC	105.0	100.2	75.16	100.8	103.9	101.4	102.6	104.3
	Ni $\mu g\ L^{-1}$	**Cu** $\mu g\ L^{-1}$	**Zn** $\mu g\ L^{-1}$	**As** $ng\ L^{-1}$	**Se** $ng\ L^{-1}$	**Sr** $ng\ L^{-1}$	**Mo** $ng\ L^{-1}$	**Cd** $ng\ L^{-1}$
LOQ	1.473	1.680	0.1778	29.89	34.43	18.14	7.097	1.581
% Accuracy on internal QC	105.7	107.3	115.5	105.1	112.7	103.0	98.31	104.1
	Sn $ng\ L^{-1}$	**Sb** $ng\ L^{-1}$	**Ba** $ng\ L^{-1}$	**Hg** $\mu g\ L^{-1}$	**Pb** $ng\ L^{-1}$	**K** $mg\ L^{-1}$	**Mg** $mg\ L^{-1}$	**Na** $mg\ L^{-1}$
LOQ	14.34	1.072	12.16	0.2834	32.16	1.000	1.000	1.000
% Accuracy on internal QC	112.3	101.4	103.1	102.7	105.5	109.4	115.0	118.2
	S $mg\ L^{-1}$	**Ru** $ng\ L^{-1}$	**Rh** $ng\ L^{-1}$	**Pd** $ng\ L^{-1}$	**Re** $ng\ L^{-1}$	**Ir** $pg\ L^{-1}$	**Pt** $ng\ L^{-1}$	**Au** $ng\ L^{-1}$
LOQ	1.000	0.9956	19.66	1.639	1.160	33.69	15.78	5.125
% Accuracy on internal QC	100.2	106.0	106.7	103.1	98.05	103.3	107.3	94.69

2.4 ICRFB tests

Three ICRFB cycling tests were used to determine the effectiveness of the electrolyte made from the purified $FeCl_2$ solution. In Section 2.4.1, the preparation of the electrolytes is discussed, followed by a brief overview of the parameters that were used as performance indicators for these electrolytes (Section 2.4.2). Finally, information on the ICRFB testing station used is presented (Section 2.4.3).

2.4.1 Electrolytes

To allow comparison on the effectiveness of the crystallisation process, electrolytes were prepared using either the unrefined $FeCl_2$, purified $FeCl_2$ or lab-grade $FeCl_2$ (Table 3). These electrolytes were subjected to ten cycles of charging and discharging on a 1 W lab-scale ICRFB (see Section 2.4.3). The composition of these electrolytes only differed in the source of $FeCl_2$ used, using the same type and amount of HCl, $CrCl_3$ and Bi_2O_3. By comparing the battery performance of the purified $FeCl_2$ to its unrefined counterpart, any performance changes resulting from the purification process were obtained. The influence of the purification was further confirmed by comparing the ICRFB data against an electrolyte prepared with lab-grade $FeCl_2$, which will further be referred to as commercial (Table 3). The electrolytes were prepared by adding the weighed salts or specific volumes of solution to volumetric flasks, before adding 1.0 M HCl (to obtain 1.3 M Fe). Each electrolyte underwent N_2 bubbling for 20 mins.

For the charge/discharge cycling tests, the electrolytes described in Table 3 were tested using 100 mL of electrolyte, where the catholyte and anolyte consisted of 50 mL each. Both catholyte and anolyte were circulated at a flow rate of 50 mL min^{-1}. For preconditioning, the electrolytes were charged to 1.3 V at a constant current of 1.120 A (current density = 40 mA cm^{-2}) to ensure that all the bismuth (which acts as catalyst for the Cr^{2+}/Cr^{3+} redox couple – see Literature review - Section 2.3.1) had plated on the anode before being discharged to 0.65 V. After this first preconditioning cycle, the ICRFB was cycled 10 times at 40 °C between 1.3 V and 0.65 V while keeping the charge/discharge current constant at 1.120 A and logging the voltage readings at regular intervals. From the charge/discharge cycles, both the discharge capacity and the capacity decay per cycle were determined. The ICRFB test cell was flushed prior to each test by cycling 1 M HCl (100 mL) for 10 minutes, after replacing the graphite felt electrodes. By using the same proton exchange membrane (PEM - Nafion117 from Fuel Cell Store), fresh electrodes (GFA 6, SGL Carbon) and identical operating conditions for each test run, any performance differences could be ascribed to the employed electrolyte.

Table 3: Compositions, concentrations and sources of different electrolytes synthesised for testing in the lab-scale ICRFB.

Electrolyte	Composition		Supplier
Unrefined	1M HCl*		
	1.3M $FeCl_2$		From 174.5 g L^{-1} unrefined $FeCl_2$ and MilliQ-water
	1.4M $CrCl_3 \cdot 4H_2O$	>96%	ACE Chemicals (Platinum line)
	10mM Bi_2O_3	≥99.9%	Merck
	1M HCl*		
Purified	1.3M $FeCl_2 \cdot 5H_2O$		Recrystallised from unrefined $FeCl_2$
	1.4M $CrCl_3 \cdot 4H_2O$	>96%	ACE Chemicals (Platinum line)
	10mM Bi_2O_3	≥99.9%	Merck
	1M HCl*		
Commercial	1.3M $FeCl_2 \cdot 4H_2O$	≥99.0%	Merck
	1.4M $CrCl_3 \cdot 4H_2O$	>96%	ACE Chemicals (Platinum line)
	10mM Bi_2O_3		≥99.9% Merck

*All 1M HCl used were obtained from LABCHEM 32% HCl and prepared with MilliQ-water (0.055 µS cm^{-1}).

2.4.2 Performance indicators

Using constant current density charge/discharge cycles, the electrolyte performance was evaluated and compared using the following performance indicators.

Coulombic Efficiency (%)

$$CE = \frac{A \times h_{(Discharge)}}{A \times h_{(Charge)}} \times 100\% \quad (18)$$

where *A* is the charging/discharging current in ampere and *h* is the time of either a charge or discharge cycle in hours.

Voltage Efficiency (%)

$$VE = \frac{\bar{V}_{(Discharge)}}{\bar{V}_{(Charge)}} \times 100\% \quad (19)$$

where $\bar{V}$ is the average voltage calculated for either the discharge or charge cycle.

Energy Efficiency (%)

$$EE = CE \times VE \quad (20)$$

Discharge Capacity (A h L^{-1})

$$Cap_{(Discharge)} = \frac{A \times h_{(Discharge)}}{L} \quad (21)$$

where A is the charging/discharging current in ampere, *h* is again the time of either a charge or discharge cycle in hours and L is the volume of electrolyte measured in litres.

Capacity decay (%.$cycle^{-1}$)

$$\frac{|Cap_{(Discharge)}(n) - Cap_{(Discharge)}(n+1)|}{Cap_{(Discharge)}(n)} \times 100\% \quad (22)$$

where *n* = the cycle number (excluding the preliminary cycle used for plating of Bi)

Area Specific Resistance (Ω cm^2)

$$ASR = \left(\frac{\overline{V}_{(Charge)} - \overline{V}_{(Discharge)}}{2}\right) \times \frac{1}{Current\ density} \quad (23)$$

where the current density, in A cm^{-2}, is obtained by dividing the constant current with the active surface area of the carbon felt electrode.

Although the focus in this study was on the discharge capacity and the capacity decay per cycle, other factors including the CE, VE, EE and ASR were determined as well, since they are commonly used in RFB research as descriptors that directly reflect energy losses due to inefficiencies occurring during battery operation.[5,17-20] The CE provides the ratio of electric charge (A h) between discharge and charge cycles, VE the ratio between the average discharge and charge voltages during cycles, and EE the ratio of power obtained between discharge and charge cycles, whereas the ASR provides the resistance based on the average voltage of the charge and discharge cycles.[20-21]

2.4.3 ICRFB testing station

As mentioned previously, the electrolyte was tested using a lab-scale RFB, which allowed the performance of each electrolyte to be measured. The RFB test station consisted of a single

flow-through RFB cell, a Potentiostat/Galvanostat (SP 240, BioLogic), a two-channel peristaltic pump (323 S, Watson Marlow) and a circulating water bath (CORDIO CD-BC6 Heating circulator, Julabo) to control the temperature of the double-walled electrolyte reservoirs. The RFB cell (Figure 16) consisted of: endplates, current collectors including insulation pads, bipolar plates, carbon felt electrodes, cell frames, multiple seals and a membrane. The graphite felt electrodes (SGL, GFA 6) had an active area of 28 cm^2 and were heat treated at 400 °C for 6 hours prior to cycling tests to increase the electrochemical activity and hydrophilicity while ensuring the thermal decomposition of any adsorbed chemicals.[6,21] A Nafion117 PEM was used in the RFB cell to separate the anolyte and catholyte while allowing proton transfer between the electrolytes to maintain balance of charge. RFB cycling tests were measured at 40 °C, using the circulating water bath together with RFB cell heating from a hot plate. The electrolytes were circulated through the system at 50 mL min^{-1} using acid compatible Masterflex L/S® Viton tubing combined with the aforementioned peristaltic pump.

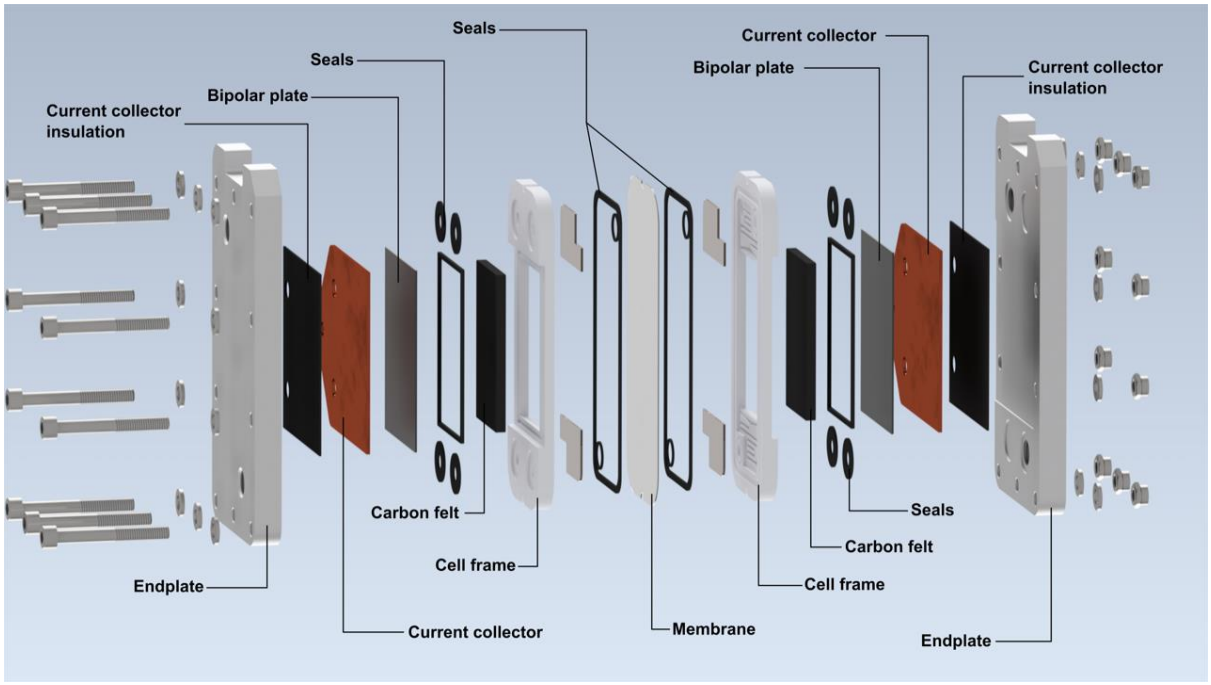

Figure 16: Schematic diagram of the lab-scale RFB cell used in the testing station.

3. Results

In this section, the results from the purification process, including the purified crystals obtained and the metal impurities removed, are discussed. Additionally, a comparison is drawn between the RFB performance of the three different electrolytes, prepared with the different sources of

$FeCl_2$, to determine whether the purification procedure serves as a feasible solution towards an economical electrolyte production.

3.1 Purification and fractional crystallisation of $FeCl_2$

The main objective of the smaller-scale (475 mL) proof-of-concept fractional crystallisation experiment was to identify and resolve possible challenges of the proposed purification technique. During the experiment, it was firstly observed that when adding Fe powder to the boiling solution, the boiling rate increased rapidly, resulting in such foaming that most of the solution spilled out of the flask. This was caused by the exothermic reaction of Fe with HCl, producing hydrogen gas, while also introducing nucleation points into the hot solution and aiding the boiling.[22] This overflow was resolved by adding the fine Fe powder slowly and in small amounts over the course of 30 minutes. Another challenge occurred during the hot filtration step where the concentrated acidic solution either clogged or dissolved the initially used filter materials made from cellulose. This issue was resolved by using a thick and highly porous polyester filter that was compatible with the acid while reducing the blockage (see also Section 2.2).

Having resolved these issues using the small-scale experiments, the fractional crystallisation procedure was upscaled as discussed in Section 2.2. According to the results, the 40 L of unrefined $FeCl_2$ solution after the crystallisation step yielded 14.23 kg crystals (enough to produce 48 L of the mixed electrolyte containing 1.3 mol L^{-1} of Fe^{2+}), resulting in a percentage yield of 52.5%. The five repetitions gave similar results, yielding almost exclusively solid green hydrated $FeCl_2$ crystals (Figure 17) with slight yellow/brown crystals visible on top, which is an indication of oxidation of the $FeCl_2$ to the hydrated $FeCl_3$ occurring during the air-exposed filtering step. After ten hours of storage, the initially wet crystals appeared dry.

Figure 17: Vacuum filtered $FeCl_2 \cdot xH_2O$ crystals.

According to ICP-OES analysis, the iron content of the sample was 12.39 mg L^{-1}, which computed to 1.239 g of iron in 4.813 g of the dry crystals analysed. Without considering any remaining adsorbed HCl (crystals were washed during the filtration), the two chloride ions would contribute 2.812 g to $FeCl_2$, which left the remaining 2.001 g as water. This would equate to a crystal structure of $FeCl_2 \cdot 5H_2O$ instead of the expected $FeCl_2 \cdot 4H_2O$.[23] However, after flowing additional N_2 over the dried crystals for another hour, the moisture content decreased, yielding an average coordinated H_2O of ~4.7 with a molar mass of 211.01 g mol^{-1}. This meant that the crystals consisted of a mixed hydrate, which would require further drying (in an inert atmosphere) if the goal were to obtain pure $FeCl_2 \cdot 4H_2O$ (198.81 g mol^{-1}).[24]

Pictures of the samples taken before and after purification are shown in Figure 18. It is clear that a significant colour change occurred due to the purification process. The unrefined solution (right) had a non-transparent dark brown colour indicative of turbidity and various undesired metals and contaminants including dissolved $FeCl_3$ and Fe_2O_3. The purified solution (left) was light green, indicative of $FeCl_2$, with a high transparency, showing that the purification process had removed a significant amount of the unwanted contaminants.

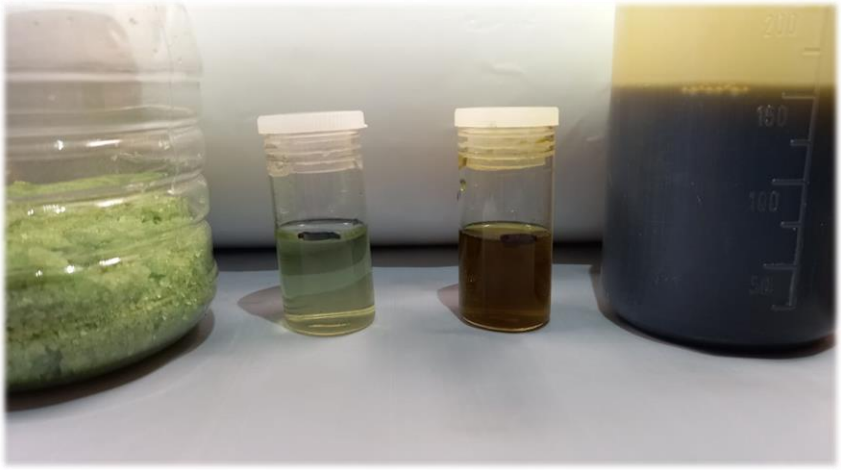

Figure 18: Picture of purified $FeCl_2 \cdot 5H_2O$ (left - solid and 1 M solution in 1.0 M HCl) and unrefined $FeCl_2$ (right – 1 M solution in 1.0 M HCl and undiluted).

In Figure 19, a photo of one of the crystals obtained after the crystallisation and washing process is shown. It is clear that the crystals had grown in skewed rectangular shapes with slanted sides, while appearing vivid emerald-green in colour. The crystals seemed visibly free from any solid impurities, including any $FeCl_3$ or Fe_2O_3 (orange or dark brown/black). The size of the crystals was fairly small, ranging from 0.1 cm to 0.7 cm, which was preferrable as larger crystals could trap impurities which would have been difficult to wash out. Although smaller crystals tend to result in a smaller yield due to the larger surface area exposed to the rinsing agent, the higher purity is preferred for the ICRFB.

Figure 19: Picture of a $FeCl_2 \cdot xH_2O$ (216.83 g mol^{-1}) crystal obtained from filtration after fractional crystallisation of the unrefined $FeCl_2$ solution.

3.2 Impurities

The influence of impurities was studied for VRFBs to determine their degrading effect on the discharge capacity as well as per-cycle capacity loss. For example, Reynard *et al.*, when studying the effect of Cu (up to 200 mg L^{-1}) in the electrolyte, found that already low concentrations of Cu (50 mg L^{-1}) promote the hydrogen evolution reaction (HER) at the negative electrode.[14] As previously mentioned (see Literature review - Section 2.3.2.2), the HER is one of the main contributors to chemical imbalance, leading to per-cycle capacity losses not only for the VRFB but also the ICRFB. When reviewing possible impurities of concern to establish which metals could possibly affect ICRFB performance, it was concluded that, although there are a small number of metals (Cu^{2+}, Ni^{2+} and Sn^{2+}) that promote the HER at low mg L^{-1} contamination levels, it would be optimal to determine the widest possible range of impurities before and after purification. Since the reduction of metals such as Cu^{2+} (0.337 V SHE), Ni^{2+} (-0.250 V SHE), Sn^{2+} (-0.136 V SHE) and Co^{2+} (-0.277 V SHE) require lower potentials than Cr^{3+} (-0.408V SHE) that is reduced at the anode during charging, it is clear that these metals will probably be reduced and deposited on the anode, with voltages reaching 1.25V.[25] According to VRFB research, Ni^{2+} for example, started to negatively impact peak current performance at 0.05 M (~3 mg L^{-1}), leading to a reduced VE by 8.9% due to its deposition on the negative electrode. When they investigated the cathodic peak current, both Mn^{2+} and Co^{2+} had an observable negative effect, though this was mainly due to mass transfer interference with V^{3+}.[10]

According to literature (Section 3.2.2), trace amounts of Cu^{2+}, Ni^{2+} and Sn^{2+} negatively influence the VRFB by promoting the HER reaction, while other metals such as Li, Cr and Ni negatively affect the mass transfer in the vanadium electrolyte. Since both the anolyte and catholyte in the ICRFB is produced by mixing Cr^{3+} and Fe^{2+} obtained from mining streams that could contain varying amounts of many transition metals, similar impurities would be present at both electrodes, increasing the possible influence these could have on the performance. Consequently, in this study a wide range of metals both in the mg L^{-1} and µg L^{-1} range (see Table 2) were analysed in the unrefined as well as the purified $FeCl_2$, using ICP-MS. For the purpose of this purification study, only the amount of metal impurities removed from the $FeCl_2$ is discussed and not the effects of specific impurities on the ICRFB performance. The overall impact of the purification on the performance is presented in Section 3.3.

In Table 4, the concentrations obtained for the contaminants that have promoted the HER in VRFB, Cu^{2+}, Ni^{2+} and Sn^{2+}, are presented for the unrefined and the purified $FeCl_2$ (before and after purification/crystallisation). Values in the table were normalised such that the [Fe] = 1.3 M (72608.8 mg L^{-1}) for all samples, thereby representing theoretical impurity concentrations present during electrolyte testing.

Table 4: ICP-MS results for those metal impurities present in purified $FeCl_2$ that are likely to promote HER in an ICRFB

Metal (mg L^{-1})	Cu	Ni	Sn
Unrefined	23.21	14.97	4.182
Purified	4.334	4.409	1.559

According to these results, the metal present at the highest concentration in the original unrefined $FeCl_2$ solution was Cu at 23.21 mg L^{-1}, followed by Ni at 14.97 mg L^{-1} and Sn at 4.182 mg L^{-1}. During purification, 81.33% Cu, 70.55% Ni and 62.72% Sn was removed from the $FeCl_2$ solution. Although, ideally, these metals would have to be removed completely to prohibit any possible negative effect on the ICRFB performance, it is clear, considering the percentage of impurities removed, that the purification procedure was effective, especially for Cu. This can be ascribed to the fractional crystallisation where, theoretically, the hydrated $FeCl_2$ crystals precipitate and grow out of solution in a high purity form, leaving most of the remaining impurities in the mother liquor that is filtered off.[26] The addition of the Fe powder (cementation), however, also contributed to this removal, since the excess addition of iron powder does cause precipitation of more noble metals such as Cu, Ni and Sn.[12-13,27] Although cementation is a relatively slow process, the reaction rates are accelerated at higher temperatures, since the rate of cementation is highly sensitive to temperature.[28] Since the iron

powder was added to the solutions when they were above 100 °C, it is understandable that these and other impurities could have deposited onto the iron powder before being removed from the hot filtrate.

When examining the other non-PGM metal impurities where the possible effects on ICRFB performance are not known (Table 5), it is apparent that Na was present in both the unrefined and purified $FeCl_2$ at very high concentrations (about 3 g L^{-1}) compared to the other metals listed. Other metals present in relatively high concentrations were Zn, Al, Mn and Si, where the purification process removed 93.96% Zn, 49.78% Al, 40.95% Mn and 4.34% Si. According to the results, the procedure was effective at removing Zn, while being less effective in removing Si.

Table 5: ICP-OES results for metal impurities present in purified $FeCl_2$

Metal (mg L^{-1})	Al	V	Mn	Co	Si
Unrefined	68.30	1.703	353.4	4.489	509.4
Purified	34.30	0.4003	208.7	2.945	487.3

Metal (mg L^{-1})	Zn	As	Mo	Na
Unrefined	249.1	3.132	4.321	3151
Purified	15.04	0.4539	0.7152	2858

While Pt contamination is known to have negative effects on the performance of RFBs due to the catalysed reduction of water, the effects of other precious group metals (PGMs) on the performance of an RFB is largely unknown. From VRFB research, it appears that some PGMs can also improve the electrochemical performance. For example, it was shown that iridium can coat the carbon felt electrodes, thereby catalytically improving the reactivity of the V^{2+}/V^{3+} redox couple at the anode surface.[19,29] Platinum has also been shown to enhance the V redox couple when adding it onto carbon felt electrodes as nanoparticles. This, however, prompted further research to develop catalyst surfaces with polymers on electrodes, since performance degrades if it enters the electrolyte.[19,30] It is thus clear that PGMs will most likely influence ICRFB performance, and hence it is important to study their removal during crystallisation and cementation (Table 6). From these metals, Au should theoretically not plate due to its high reduction potential, but Ir and Pt plating could potentially occur, which might benefit the electrochemical activity of specifically the $Cr(H_2O)_5Cl^{2+}/Cr(H_2O)_5Cl^{+}$ couple as it does with V. However, since any Pt remaining in the electrolyte after plating, or due to deplating during discharge, would be undesired (catalysing HER), it should be removed. The concentrations of all PGMs were reduced by the purification method, with the purification efficiency decreasing

in the order Ru>Pt>Ir>Pd>Au>Rh>Re. The Pt content was initially 4.142 mg L^{-1} and the procedure reduced it by 54.23% (1.896 mg L^{-1}). Depending on the lower limits for an ICRFB electrolyte, more than one purification step might be required to sufficiently remove the Pt.

Table 6: ICP-OES results for PGMs present in purified $FeCl_2$

Metal (µg L^{-1})	Ru	Rh	Pd	Re	Ir	Pt	Au
Unrefined	89.78	212.3	509.9	85.88	39.96	4142	117.1
Purified	33.04	138.1	283.6	57.59	22.22	1896	65.14

3.3 RFB results

During testing with the lab-scale RFB, initial Bi plating was confirmed (by the signature curves of voltage over time from the first charge) for all three electrolytes. With all three electrolytes, even the electrolyte synthesised from the dark, unfiltered, and unrefined $FeCl_2$ solution that contained a number of unknown impurities and/or solids, typical charging and discharging cycles were obtained for 10 cycles. The obtained results are reviewed in this section by comparing the performance of the three electrolytes firstly in terms of the CE, VE and EE (Section 3.3.1), then the storage capacity expressed in terms of the change in time of the charge and discharge cycles (Section 3.3.2), and finally the electrolyte capacity (Section 3.3.3).

3.3.1 Efficiencies

According to the VRFB literature (Section 2.4.2), the CE, VE and EE are parameters or descriptors that indicate battery efficiencies while also providing some information on the activity on electrode surfaces. Since metal impurities mainly influence the activity on the electrode surfaces, determining the CE, VE and EE would provide information on the success of the purification procedure when comparing electrolytes using unrefined, purified or a commercial $FeCl_2$ source.

While especially the VE and EE values obtained (Figure 20 and Table 7) were lower than those provided in literature,[20] the ICRFB test was suitable to show the influence of the Fe source. It is clear that the electrolyte containing the purified $FeCl_2$ (Figure 20(b)) outperformed its unrefined counterpart (Figure 20(a)) in all aspects, yielding a higher CE (8.08%), VE (5.17%) and EE (9.25%), as well as a lower ASR (15.82%). Furthermore, the VE from the unrefined $FeCl_2$ also decreased substantially during 10 cycles (more than 6%). It is also clear that the electrolyte made from the purified $FeCl_2$ performed similar to the electrolyte made with

the commercial $FeCl_2$ (Figure 20(c)), displaying a higher average VE and EE, but a lower EE retention. Only the CE of the electrolyte using the commercial $FeCl_2$ was unmatched, increasing with cycling. According to Table 7, the ASR of the purified $FeCl_2$ electrolyte was even lower than that obtained when using the commercial $FeCl_2$. It is thus clear that the partial removal of a broad range of dissolved metals from the unrefined $FeCl_2$ did lead to an improved ICRFB performance. It is possible that the increased VE retention resulted from a reduced HER rate due to the lower Cu, Ni and Sn contamination levels. However, it is recommended that the effects of individual metals on the HER and discharge capacity retention should be determined experimentally.

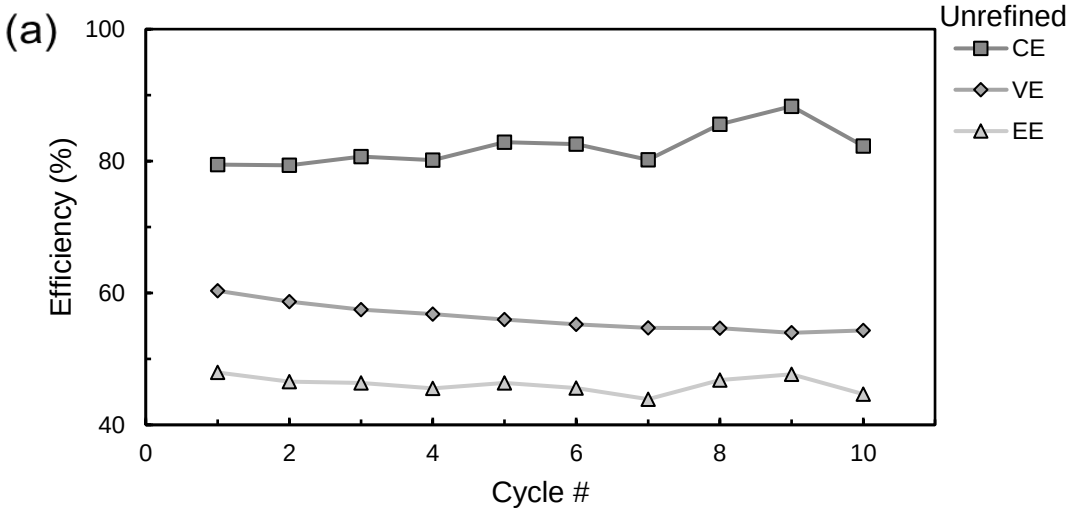

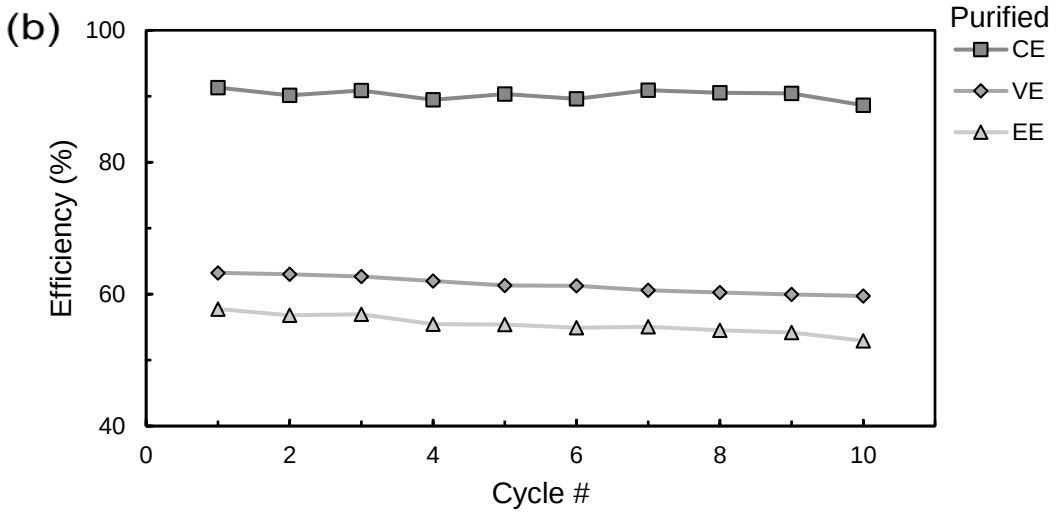

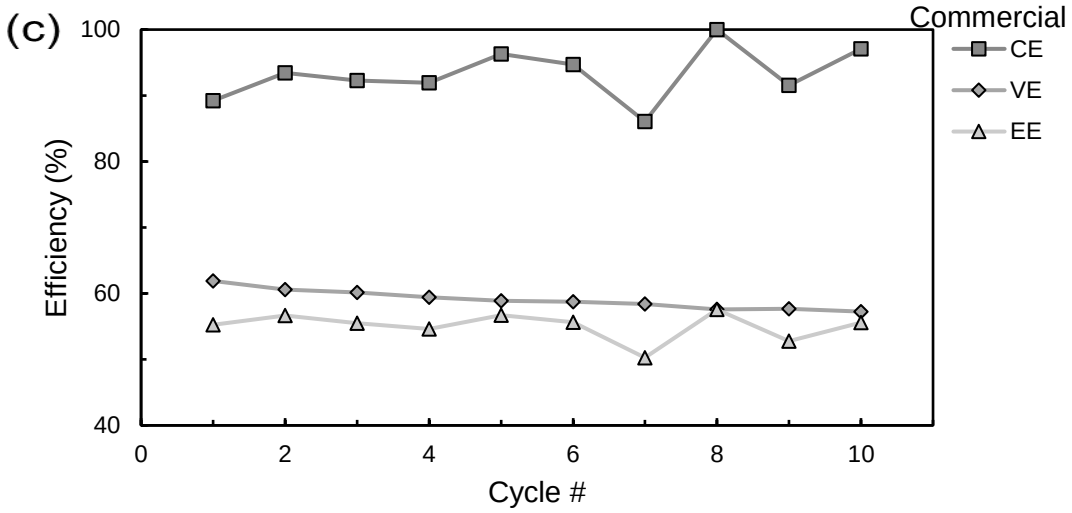

Figure 20: Coulombic efficiency, voltage efficiency, and energy efficiencies obtained from electrolytes with (a) an unrefined, (b) a purified and (c) a commercial $FeCl_2$ source.

Table 7: Comparison of ICRFB performance with electrolytes from different $FeCl_2$ sources.

Electrolyte ($FeCl_2$)	Efficiency at 40 mA cm^{-1} (%)			ASR (Ω cm^2)
	CE	VE	EE	
Unrefined	82.14	56.22	46.14	6.88
Purified	90.22	61.39	55.39	5.94
Commercial	93.26	59.05	55.05	6.29

3.3.2 Electrolyte storage capacity

The charge/discharge times achieved by each of the various electrolytes were measured during galvanostatic battery cycles (Figure 21), as these times are identical to the capacity of an electrolyte (A h), ultimately affecting the battery's storage capacity and lifetime. The 10 cycles investigated are indicative of how electrolytes would perform when subjected to short term battery operation.

Figure 21 shows the charge/discharge time as a function of the cycle number for electrolytes prepared from (a) an unrefined, (b) a purified/crystallised and (c) a commercial lab-grade $FeCl_2$ source. From Figure 21(a) and (b), it is clear that the charge/discharge times increased significantly due to the purification/crystallisation process. Since the charge/discharge cycles were measured galvanostatically (constant current), the increase in charge/discharge times

(A h) are indicative of an increase in RFB storage capacity. Considering the total run-time of ten charge/discharge cycles, the purified $FeCl_2$ electrolyte ran for 8.02 h, which is a 124.6% longer runtime (4.45 h) than the 3.57 h obtained when using the unrefined $FeCl_2$ electrolyte. When comparing Figure 21(b) and (c), it is clear that the total run-time of the recrystallised $FeCl_2$ electrolyte (b) was only 5.6% shorter (8.02 h) than the 8.50 h achieved when using the electrolyte made from the commercial $FeCl_2$. It can be assumed that the increased time, and hence storage capacity, obtained when using the purified electrolyte was probably the result of two factors: firstly, during the purification, any existing Fe^{3+} was reduced to Fe^{2+}, providing more Fe^{2+} species that could be oxidised and reduced during charging and discharging. Secondly, the amounts of other metals and contaminants present were reduced during the purification, resulting in a further increase in storage capacity. This is likely as the presence of the contaminants could have increased the internal resistance due to reduced electrochemical activity on the electrode surfaces and an increased solution saturation contributing to a lower conductivity.

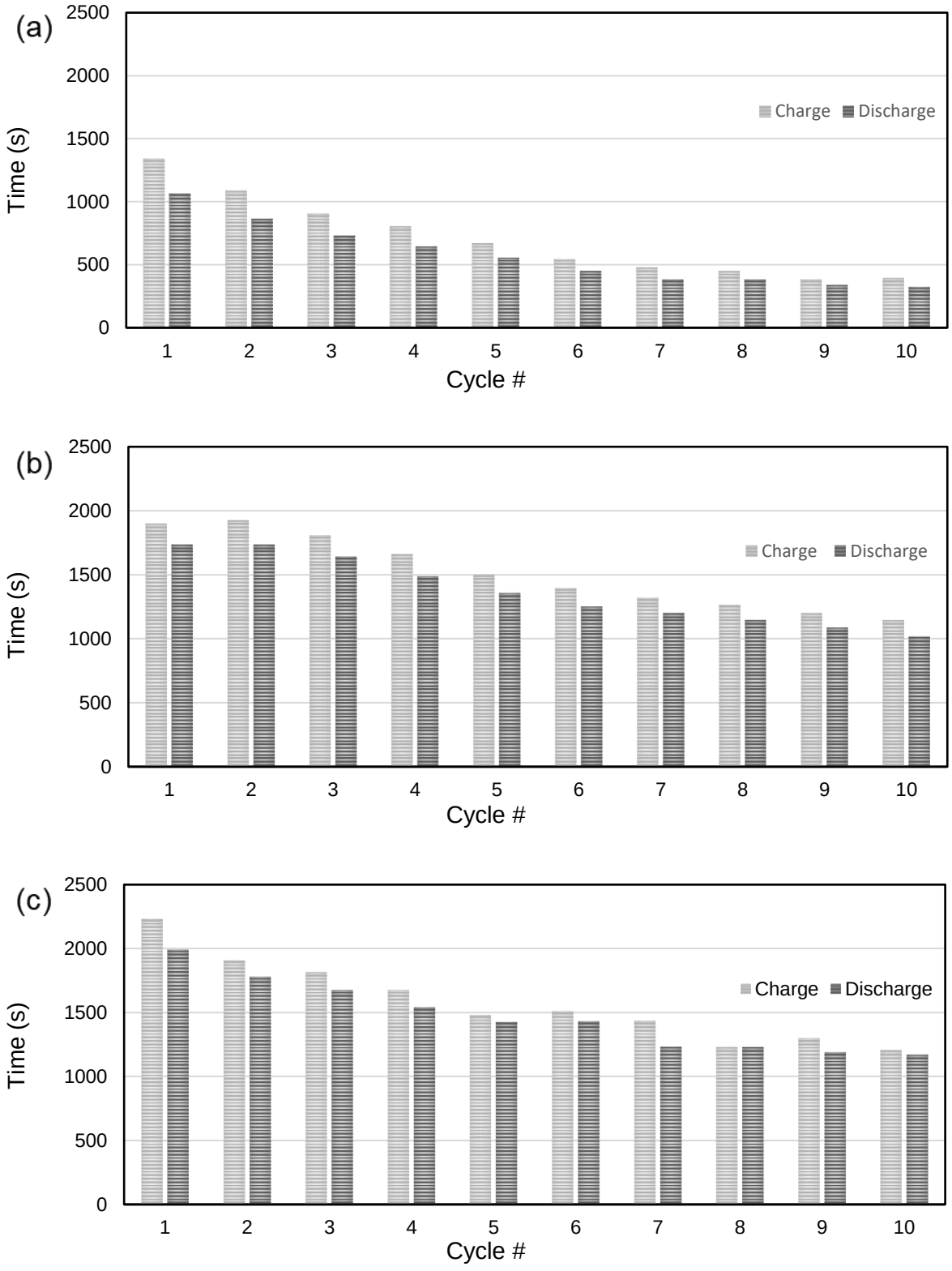

Figure 21: Charge and discharge times over 10 cycles obtained from electrolytes with (a) an unrefined, (b) a purified and (c) a commercial $FeCl_2$ source.

3.3.3 Electrolyte capacity and decay

In order to properly compare the discharge capacity of the electrolytes, we need to consider the retention of discharge capacity, since sustainability of discharge capacity is important for long-term battery operation.[6,31] Therefore, the decay of discharge capacity was also investigated over ten cycles (Figure 22). The electrolyte with unrefined $FeCl_2$ consistently performed at significantly lower capacities despite starting off good at above 4000 mA h L^{-1}. When comparing the best discharges, the electrolyte with recrystallised $FeCl_2$ initially had 29.5% better discharge capacity than the unrefined, but 12.8% lower than the electrolyte with purchased $FeCl_2$. However, as the electrolytes completed more cycles, the recrystallised $FeCl_2$ performed almost as well as the purchased and increasingly superior to the unrefined. At cycle 5, the recrystallised electrolyte had 102.3% better capacity than the unrefined and only 4.9% less than the purchased.

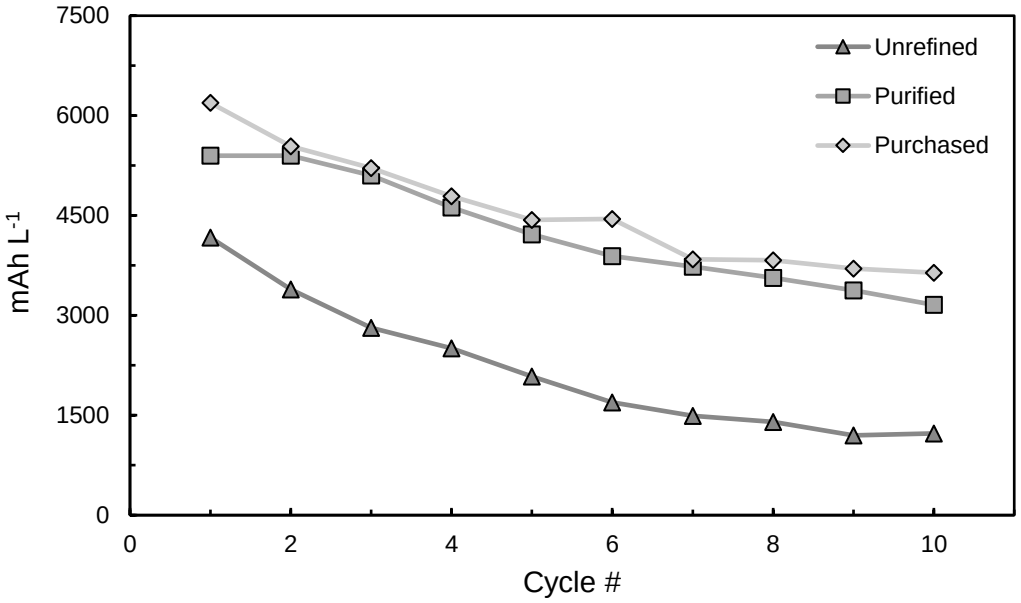

Figure 22: Discharge capacity of different electrolytes over 10 cycles.

Interestingly, the electrolyte with recrystallised $FeCl_2$ does not follow the usual pattern of dropping considerably in discharge capacity between the first and second cycle. A possible explanation to this is the balancing of ions through the membrane, which usually completes during the Bi plating cycle, is still happening until cycle #2 whereafter the ICRFB performs optimally. This could be due to some of the element/elements present in the crystals in trace amounts. Nevertheless, this phenomenon helped the average per cycle decay of this electrolyte. The average per cycle decay of the recrystallised electrolyte is 5.7%, which is low

compared to the 12.5% of the unrefined and almost on par with the 5.6% of the purchased. It is noteworthy that the per cycle decay of capacity obtained experimentally is higher than other sources, however, this is due to various factors. Firstly, when Zeng *et al*., (2016) obtained a decay as low as 0.6% also using Bi, a flow-field cell was used rather than a flow-through cell. Additionally, the electrolytes were only cycled between 1.2V and 0.8V, which resulted in less hydrogen production due to a lower upper potential at the anode, which would cause capacity losses.[7] An older source from NASA experimenting on catalysts such as bismuth reported about 1% decay, although it is unclear whether this specific value was obtained with 1.2V or 1.3V cell potentials.[32] Other factors could also cause different per cycle decay rates, such as the impurities in the HCl used, the purity of both the chrome and iron sources and the degree to which the system is sealed, i.e. the amount of oxygen exposed to the system, to name a few. Furthermore, it is also known that small amounts of metal impurities can deposit on the anode, where they promote the HER.[9-10,15,33] Nonetheless, even with the higher rates of capacity loss, comparing the $FeCl_2$ produced during fractional crystallisation to the high purity ferrous chloride of a reputable supplier, without changing any other experimental variables, should yield a measurement of the recrystallisation procedure's success.

In conclusion, when comparing the electrolyte performance of the recrystallised ferrous chloride in terms of discharge capacity, it excelled far beyond the unrefined product and performed only slightly below the high-grade ferrous chloride. The increase in discharge capacity and its retention could definitely be the result of metal impurities removed by the purification procedure. Additionally, the average per cycle decay obtained with the purified $FeCl_2$ was almost on par with the high-grade $FeCl_2$ tested on the same system.

3.4 Cost analysis

When comparing only the cost of the Fe required to make 10 L of an ICRFB electrolyte containing a total of 1.3 M Fe, it is clear (Table 8) that the cost of purifying alternative Fe sources, such as industrial-grade $FeCl_2$, costs a fraction (5.42%) of lab-grade $FeCl_2$. The total cost of Fe from the commercial source in this study would have been R6 470.05, whereas the total cost of the purified option was estimated as R350.37. The breakdown of the purification cost (Figure 23) confirms that the largest contributor to the cost was the nitrogen gas required to prevent oxidation during purification, drying and storage, making up 61% of the total cost, while the $FeCl_2$ itself only contributed 6.6%. However, since nitrogen gas was not used sparingly in this study, the cost thereof could further be reduced by using it more efficiently, for example by incorporating a closed boiling system to the purification procedure.

Table 8: Cost comparison of commercial and purified Fe sources to synthesise 10 L electrolyte, excluding $CrCl_3$, Bi, or HCl.

Fe source	Component	Required for 10 L Electrolyte	Cost (ZAR)
Commercial	$FeCl_2 \cdot 4H_2O$ (Merck)[34]	2.585 kg	6 470.05
Purified	Unrefined $FeCl_2$ solution (Metsep)*	7.924 L	23.20
	Fine Fe powder (Merck)[35]	138.76 g	102.53
	HCl 32% (Labchem)*	203.1 mL	10.64
	Nitrogen (Afrox)* for purification, drying and storage of crystals	~1/8 cylinder	214.00

*Price obtained from supplier

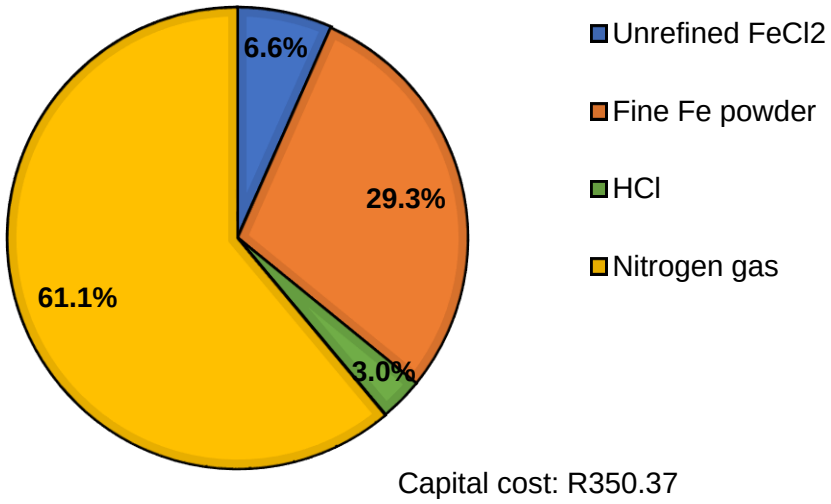

Figure 23: Cost breakdown of unrefined $FeCl_2$ purification scaled for 10 L ICRFB electrolyte.

4. Conclusion

In this study, a low-cost unrefined $FeCl_2$, not suitable for battery use, was effectively purified at a suitable scale, using an inexpensive and simple purification method. By combining cementation and fractional crystallisation, the concentrations of most of the metal impurities that were expected to negatively affect ICRFB performance were adequately reduced, while minimising the amount of Fe^{3+} levels present. It was then shown that the $FeCl_2$ produced by this procedure can be used to synthesise an electrolyte that performed on par in terms of CE, VE and EE with an electrolyte prepared using lab-grade $FeCl_2$ from a commercial source. The electrolyte containing the purified $FeCl_2$ also outperformed its unrefined counterpart in terms

of discharge capacity and capacity retention. Through a cost estimate, it was found that using this purification procedure, the CAPEX cost attributed to the ICRFB electrolyte preparation could be reduced, while minimally sacrificing performance. To reduce the electrolyte cost even further, the purification process could be optimised by reducing the nitrogen gas consumption during purification and drying.

5. References

1. Suman, A., Role of renewable energy technologies in climate change adaptation and mitigation: A brief review from Nepal. *Renewable and Sustainable Energy Reviews* **2021,** *151*, 111524.
2. Menyah, K.; Wolde-Rufael, Y., CO2 emissions, nuclear energy, renewable energy and economic growth in the US. *Energy Policy* **2010,** *38* (6), 2911-2915.
3. Chen, T.; Jin, Y.; Lv, H.; Yang, A.; Liu, M.; Chen, B.; Xie, Y.; Chen, Q., Applications of Lithium-Ion Batteries in Grid-Scale Energy Storage Systems. *Transactions of Tianjin University* **2020,** *26* (3), 208-217.
4. Chen, R.; Kim, S.; Chang, Z., Redox Flow Batteries: Fundamentals and Applications [open access]. 2017; pp 103-118.
5. Li, L.; Kim, S.; Wang, W.; Vijayakumar, M.; Nie, Z.; Chen, B.; Zhang, J.; Xia, G.; Hu, J.; Graff, G.; Liu, J.; Yang, Z., A Stable Vanadium Redox-Flow Battery with High Energy Density for Large-Scale Energy Storage. *Advanced Energy Materials* **2011,** *1*.
6. Zeng, Y. K.; Zhao, T. S.; An, L.; Zhou, X. L.; Wei, L., A comparative study of all-vanadium and iron-chromium redox flow batteries for large-scale energy storage. *Journal of Power Sources* **2015,** *300*, 438-443.
7. Zeng, Y. K.; Zhou, X. L.; An, L.; Wei, L.; Zhao, T. S., A high-performance flow-field structured iron-chromium redox flow battery. *Journal of Power Sources* **2016,** *324*, 738-744.
8. Wadia, C.; Albertus, P.; Srinivasan, V., Resource constraints on the battery energy storage potential for grid and transportation applications. *Journal of Power Sources* **2011,** *196* (3), 1593-1598.
9. Cao, L.; Skyllas-Kazacos, M.; Menictas, C.; Noack, J., A review of electrolyte additives and impurities in vanadium redox flow batteries. *Journal of Energy Chemistry* **2018,** *27* (5), 1269-1291.
10. J. H. Park; J. J. Park; H. J. Lee; B. S. Min; J. H. Yang, Influence of Metal Impurities or Additives in the Electrolyte of a Vanadium Redox Flow Battery. *Journal of The Electrochemical Society* **2018,** *165* (7), A1263-A1268.
11. Kebede, A. A.; Kalogiannis, T.; Van Mierlo, J.; Berecibar, M., A comprehensive review of stationary energy storage devices for large scale renewable energy sources grid integration. *Renewable and Sustainable Energy Reviews* **2022,** *159*.
12. Agrawal, M. L.; Kapoor, R. D., Theoretical considerations on the cementation of copper with iron. *Journal of the Southern African Institute of Mining and Metallurgy* **1982,** *82* (4), 106-111.

13. Sareyed-Dim, N. A. The cementation of nickel onto iron at elevated temperatures. Chemical Engineering, 1974.
14. Reynard, D.; Vrubel, H.; Dennison, C. R.; Battistel, A.; Girault, H., On-Site Purification of Copper-Contaminated Vanadium Electrolytes by using a Vanadium Redox Flow Battery. *ChemSusChem* **2019,** *12* (Issue 6), 1222-1228.
15. Pahlevaninezhad, M.; Pahlevani, M.; Roberts, E. P. L., Degradation of the All-Vanadium Redox Flow Battery in the Presence of Metal Impurities. *ECS Meeting Abstracts* **2021,** *MA2021-02* (4), 497-497.
16. http://www.ncp.co.za/ferrous-chloride/ (accessed 2022-04-03).
17. Chen, D.; Hickner, M. A.; Agar, E.; Kumbur, E. C., Selective anion exchange membranes for high coulombic efficiency vanadium redox flow batteries. *Electrochemistry Communications* **2013,** *26*, 37-40.
18. Tang, A.; Bao, J.; Skyllas-Kazacos, M., Dynamic modelling of the effects of ion diffusion and side reactions on the capacity loss for vanadium redox flow battery. *Journal of Power Sources* **2011,** *196* (24), 10737-10747.
19. Kim, K.; Park, M.-S.; Kim, Y.; Kim, J. H.; Dou, S.; Skyllas-Kazacos, M., A technology review of electrodes and reaction mechanisms in vanadium redox flow batteries. *Journal of Materials Chemistry A* **2015**.
20. Zhang, H.; Tan, Y.; Li, J.; Xue, B., Studies on properties of rayon- and polyacrylonitrile-based graphite felt electrodes affecting Fe/Cr redox flow battery performance. *Electrochimica Acta* **2017,** *248*, 603-613.
21. Kim, S.; Thomsen, E.; Xia, G.; Nie, Z.; Bao, J.; Recknagle, K.; Wang, W.; Viswanathan, V.; Luo, Q.; Wei, X.; Crawford, A.; Coffey, G.; Maupin, G.; Sprenkle, V., 1 kW/1 kWh advanced vanadium redox flow battery utilizing mixed acid electrolytes. *Journal of Power Sources* **2013,** *237*, 300-309.
22. Dinardo, O.; Kondos, P. D.; MacKinnon, D. J.; McCready, R. G. L.; Riveros, P. A.; Skaff, M. *Study on metals recovery/recycling from acid mine drainage*; Canada Centre for Mineral and Energy Technology, Ottawa, ON (Canada): 555 Booth Street, Ottawa, Ontario, 1991.
23. Bull, J. N.; Maclagan, R. G. A. R.; Fitchett, C. M.; Tennant, W. C., A new isomorph of ferrous chloride tetrahydrate: A 57Fe Mössbauer and X-ray crystallography study. *Journal of Physics and Chemistry of Solids* **2010,** *71* (12), 1746-1753.
24. Gayer, K. H.; Wootner, L., The Hydrolysis of Ferrous Chloride at 25°1. *Journal of the American Chemical Society* **1956,** *78* (16), 3944-3946.
25. Skoog, D. A.; West, D. M.; Holler, F. J.; Crouch, S. R., *Fundamentals of analytical chemistry*. Ninth edition. ed.; Brooks/Cole, Cengage Learning: Belmont, CA, 2014; p A12-A14.

26. Joachim, U., The Crystallization Technology Handbook, 2nd ed Edited by Marcel Dekker: . In *Crystal Growth & Design*, A. Marsmann, Ed. American Chemical Society: New York, Basel, 2001; pp 25-44 & 439-581.
27. Free, M. L., *Hydrometallurgy Fundamentals and Applications*. 2 ed.; Springer, Cham: 2022; p 458.
28. Saylam, H. In *Deposition of cobalt on iron powder*, 1982.
29. Cheng, D.; Li, Y.; Han, C.; He, Z.; Zhu, J.; Dai, L.; Meng, W.; Wang, L., Endowing electrospun carbon fiber with excellent electrocatalytic properties towards VO2+/VO2+ redox reaction for vanadium redox flow battery by in situ iridium decoration. *Colloids and Surfaces A: Physicochemical and Engineering Aspects* **2020,** *586*, 124137.
30. Jeong, S.; Kim, S.; Kwon, Y., Performance enhancement in vanadium redox flow battery using platinum-based electrocatalyst synthesized by polyol process. *Electrochimica Acta* **2013,** *114*, 439-447.
31. Zeng, Y. K.; Zhao, T. S.; Zhou, X. L.; Zou, J.; Ren, Y. X., A hydrogen-ferric ion rebalance cell operating at low hydrogen concentrations for capacity restoration of iron-chromium redox flow batteries. *Journal of Power Sources* **2017,** *352*, 77-82.
32. Hagedorn, N. H. *Nasa redox storage system development project*; NAS 1.15:83677; National Aeronautics and Space Administration, Cleveland, OH (USA). Lewis Research Center: 1984.
33. Park, J. H.; Park, J. J.; Lee, H. J.; Min, B. S.; Yang, A., Influence of Metal Impurities or Additives in the Electrolyte of a Vanadium Redox Flow Battery. *Journal of The Electrochemical Society* **2018,** *165* (7), A1263-A1268.
34. Ferrous Chloride Tetrahydrate. https://www.sigmaaldrich.com/ZA/en/search/fecl2?focus=products&page=1&perpage=30&sort=relevance&term=fecl2&type=product (accessed 2022-04-13).
35. Fine Iron Powder. https://www.sigmaaldrich.com/ZA/en/search/fe-powder?focus=products&page=1&perpage=30&sort=relevance&term=fe%20powder&type=product_name (accessed 2022-04-13).

CHAPTER 4

UV-Vis Spectrophotometric analytical technique for monitoring Fe^{2+} in the positive electrolyte of an ICRFB.

Johannes Petrus du Toit, Henning Manfred Krieg, Nico Mans, Derik Jacobus van der Westhuizen.

Abstract

The iron-chromium redox flow battery (ICRFB) is a promising low-cost large-scale energy storage solution. One of the main challenges associated with the ICRFB, compared to the vanadium redox flow battery (VRFB), is the capacity decay rate caused by an imbalance between the electrolytes. To counter and rectify the imbalance, an ICRFB requires a rebalancing system, which in turn requires an effective electrolyte monitoring system. This study was therefore conducted to develop a method that could be used to monitor the imbalance and rebalancing of a low-cost ICRFB by means of the Fe^{2+}/Fe^{3+} ratio. Using the near-IR (NIR) light spectrum (UV-Vis spectrophotometry), a function was derived from Beer's law that could be used to approximate Fe^{2+} concentrations in acidic aqueous solutions in the presence of Fe^{3+}. The function was derived by investigating the effect of temperature, HCl concentration, Cr^{3+}, Fe^{3+} and dissolved gasses on NIR absorbance. An analytical method was developed that could analyse the redox speciation of iron, differentiating between identical elements in solution with different valences, which could easily be used to monitor the imbalance and rebalancing of an ICRFB.

Keywords: Iron-chromium redox flow batteries, Electrolyte imbalance, Iron redox speciation, Ultraviolet-visible analysis, Beer-Lambert law, Electrolyte monitoring method

1. Introduction

In 1974, NASA conceptualised the idea of using an iron- and chromium-based electrolyte in a redox flow battery (RFB). Initially, the development of the iron-chromium redox flow battery ICRFB was held back by technological constraints such as limited selectivity and area specific resistance of the membranes available at that time, resulting in excessive electrolyte cross-over and low voltage efficiencies.[1-2] However, with continual technological advancements, RFB technology in general has become more viable as a large-scale energy storage solution (LESS).[3-4]

Shortly after the introduction of the ICRFB, research into the all-vanadium redox flow battery (VRFB) gained traction. Due to the decoupling of storage and power (intrinsic to RFBs), the ease of upscaling RFB storage capacity via the electrolyte volume/concentration allowed RFB technology to develop into a promising LESS.[1,5-7] However, VRFB technology still faces challenges hindering it's economic viability, including the cost of a required perfluorinated membrane and the cost of the vanadium electrolyte, which currently makes up 53% of the total battery cost.[7-8] As a result, ICRFB technology again gained more attention recently, not only because of the advances made in membrane technology, but more importantly due to the lower cost and availability of the iron-chrome couple compared to that of vanadium.[1,3-4] When comparing the cost of ICRFB's to VRFB's (1 MW-8h energy storage systems), the vanadium electrolyte was priced at \$122 kWh^{-1} in 2015, whereas the iron-chrome electrolyte only cost \$17 kWh^{-1}.[7] Additionally, there is an abundance of iron and chrome minerals as global production of ferrochrome was estimated to be 11.7 megatons in 2017, with South Africa holding the largest reserves of chromium ore in the world.[9-10]

Even though RFB technology has come a long way, ICRFB development is hindered by some specific challenges yet to be resolved. Foremost, the ICRFB suffers from a notable rate of discharge capacity decay per cycle, resulting in the requirement of a significant and efficient rebalancing system.[4,7,11-12]

The two half reactions of the Fe and Cr in the electrolytes at the respective electrodes during charging and discharging are as follows:[13]

Charging:	$Fe^{2+} \rightarrow Fe^{3+} + e^-$ (positive electrolyte)	0.771 V vs. SHE
	$Cr^{3+} + e^- \rightarrow Cr^{2+}$ (negative electrolyte)	-0.408 V vs. SHE

Discharging: $Fe^{3+} + e^- \rightarrow Fe^{2+}$ (positive electrolyte) -0.771 V vs. SHE

$Cr^{2+} \rightarrow Cr^{3+} + e^-$ (negative electrolyte) 0.408 V vs. SHE

Since the ions are usually in an acidic chloride environment (supporting electrolyte), these half reactions are accompanied by the migration of free-roaming H^+ or Cl^- ions through a cation or anion exchange membrane (CEM or AEM, respectively) to complete the electrical circuit. Most of the discharge capacity decay is caused by unwanted chemical side reactions resulting in chemical imbalance. These reactions are worsened by the higher overpotentials required during charging, caused by the internal resistances of the electrolytes and the ion exchange membrane (IEM). According to the current understanding, the most prominent side reaction is the hydrogen evolution reaction (HER) occurring at the negative electrolyte (Cr^{2+}/Cr^{3+}):[11,13]

$2H^+ + 2e^- \rightarrow H_2$ 0.000 V

During charging, this reaction competes with the reduction of chromium, which in principle could then result in the following reaction in the positive electrolyte:

Charging: $2Fe^{2+} + 2H^+ + Cr^{3+} \rightarrow 2Fe^{3+} + H_2 + Cr^{3+}$

The result of this competition is that Fe^{2+} is oxidised without the equimolar reduction of Cr^{3+}, i.e. there are not equal amounts of $Fe^{2+/3+}$ and $Cr^{3+/2+}$ ions at any given time.[11-12] As a result, during discharge, not enough electrons are released by the oxidation of the lower concentration of Cr^{2+} in the negative electrolyte to reduce all of the Fe^{3+} in the positive electrolyte. Over time, this results in an accumulation of Fe^{3+} ions in the positive electrolyte vessel, leading to a loss of charge/discharge capacity. This charge/discharge capacity loss then leads to a loss in the maximum state of charge (SOC) attainable, ultimately resulting in declining battery performance.

To correct the imbalance, a rebalancing cell must be added that can maintain the ionic balance between the electrolytes. It was shown that such rebalancers, by reducing the accumulated Fe^{3+}, can reduce the average 2% discharge capacity decay per cycle of an ICRFB to as low as 0.3%.[3,11] According to a review of electrolyte imbalance, the HER is also one of the main causes of the chemical imbalance in VRFB's, due to the consumption of charging current that produces H_2.[14] Research focussing on the rebalancing of VRFBs has demonstrated the suitability of chemical rebalancing methods, where for example ethanol was successfully used to reduce the vanadium ions without producing impurities.[15-16] When applying this to the ICRFB, it is clear that a reducing agent could facilitate the reduction of excess Fe^{3+}, thereby recovering the SOC.

While a few techniques exist that can analyse trace amounts of Fe^{2+} and Fe^{3+} in water, at present no suitable technique exists for in-line analysis of the elevated ionic concentrations of Fe^{2+} and Fe^{3+} in an ICRFB.[17-21] This is, however, necessary, not only to quantify the reduction required or obtained during rebalancing, but also for providing continuous monitoring of the electrolyte composition and SOC during operation.

For VRFB, many techniques have been investigated for monitoring the V species in the electrolyte, often focussing on methods that could be used to determine a true SOC, as the traditional way of measuring SOC such as open circuit voltage (OCV) fails due to imbalance between the half-cells.[15-16,22] Shin *et al., (2020)* for example, demonstrated the suitability of light absorption, using ultraviolet-visible (UV-Vis) spectrophotometry, to monitor the SOC of a VRFB.[23] Another technique investigated entailed measuring the conductivity of the electrolytes, however, in this case, measuring the chemical imbalance remained a challenge due to ionic build-up in the half-cells (due to crossover) influencing the conductivity.[16] Other methods to measure species in the VRFB, and iron redox speciation, were extensively reviewed in the Literature review - Section 2.2.2 and Section 3.1.2.

Significantly less research has focussed on measuring the SOC in ICRFBs. As mentioned, although the imbalance in the ICRFB is caused at the chromium side by hydrogen production, the result is a build-up of Fe^{3+} at the iron (positive) side of the RFB. Hence, it should be possible to measure the imbalance on the iron side after a discharge cycle. This would, however, require an analytical technique that could measure the Fe^{2+} and Fe^{3+} concentrations independently since the SOC never truly reaches 0% or 100% during battery operation, i.e., both ions will always be present. It is known that Fe^{2+} and Fe^{3+} have almost identical chemical and physical properties, except for their electron configuration, with Fe^{2+} = $[Ar]3d^6$ and Fe^{3+} = $[Ar]3d^5$. Furthermore, in crystal form, both cations are stabilised and considered labile by Cl^- and water ligands in octahedral configurations.[24-25] According to the crystal field and ligand field theories, these are weak field ligands, where the electron orbitals will have a small Δ_o. Consequently, the orbital configurations for Fe^{2+} and Fe^{3+} will be $t_{2g}^4e_g^2$ and $t_{2g}^3e_g^2$, respectively. Since these orbitals have different occupations, their excitation states will differ when absorbing electromagnetic radiation and, as a result, the different crystals' solutions in acidic medium would have different colours.[26-27]

Accordingly, the purpose of this study was to derive and develop a mathematical and analytical model to monitor the Fe^{2+} and Fe^{3+} concentrations using UV-Vis spectrophotometry, based on the different absorption properties of Fe^{2+} and Fe^{3+}. This could provide a method that can continuously measure Fe^{2+}/Fe^{3+} concentrations during ICRFB operation and, consequently, monitor the imbalance in line. In addition, other positive electrolyte components such as Cr^{3+},

water, HCl, dissolved O_2 and/or N_2 could influence the measurement of the Fe^{2+} and Fe^{3+} concentrations. Accordingly, a second goal of this study was to determine the influences of Cr^{3+}, water, HCl, N_2 and O_2 on the measured Fe^{2+} and Fe^{3+} concentrations.

2. Theory

The absorption of light by chemical species can be derived from the Beer-Lambert law, where the transmitted intensity (*I*) is defined as[28]

$$I = I_0 10^{-e(J)L} \tag{24}$$

where J = the absorbing species and L = the sample length (cm). This can then be expressed in terms of the absorption,

$$A = \varepsilon bc \tag{25}$$

where *A* = Absorbance, ε = molar absorptivity or molar absorption constant (mol^{-1} dm^3 cm^{-1}), *b* = path length of the sample (cm) and c = concentration of a specific species (mol dm^{-3}). At any given wavelength, the total absorbance (A_{total}) of all species in an electrolyte solution would be measured. If membrane crossover in the ICRFB is assumed to be negligible (using a selective IEM), the catholyte of an ICRFB should only contain ionic species from dissolved Fe/Cr chloride salts and Bi_2O_3 (catalyst) in HCl during typical operation.[2,7,29]. Little to no literature exists on using other acidic solvents than HCl, however using other counterions than Cl^- would affect UV-Vis spectra by shifting the positions of absorption peaks.[30] As for the small amounts of bismuth present (usually 0.01 mM to 5.0 mM) in the positive electrolyte, little to no absorption was expected and confirmed. By additionally including the dissolved gasses that will typically be encountered, the total absorbance of the positive electrolyte of the ICRFB can then be written as the sum of the individual absorbances:

$$A_{total} = A(Fe^{2+}) + A(Fe^{3+}) + A(Cr^{3+}) + A(Bi^{3+}) + A(O_2) + A(N_2) + A(H^+) + A(Cl^-) + A(H_2O, H_3O^+, OH^-) \tag{26}$$

Since chrome is present only as a spectator ion in the positive electrolyte and Cr^{2+} would only be present due to the unlikely event of severe membrane crossover, only Cr^{3+} was included in Equation (26).

3. Materials and methods

3.1 Materials

The following chemicals were used to simulate a typical ICRFB electrolyte and prepare samples in general.

- 32% HCl (LABCHEM). The HCl solution was prepared by diluting 10.17 M to 1.00 M.
- Iron(III) chloride hexahydrate (Rochelle Chemicals; ≥ 99.0%) and iron(II) chloride tetrahydrate (Sigma-Aldrich (Merck); ≥ 99.0%) were used as source for Fe^{3+} (ferric chloride) and Fe^{2+} (ferrous chloride), respectively.
- Chromium(III) chloride hexahydrate (Sigma-Aldrich (Merck); ≥ 98.0%) was used as Cr^{3+} source.
- Bi_2O_3 (Sigma-Aldrich (Merck); ≥ 99.9%)
- Ultra-purified Milli-Q water (0.055 µS cm^{-1}).

The following standard solutions provided by Ultraspec® were used to prepare the standards for inductively coupled plasma - optical emission spectrometry (ICP-OES) analysis:

- 1 000 ± 3 µg mL^{-1} Fe (99.999%) in 5% HNO_3
- 10 000 ± 30 µg mL^{-1} Fe (99.999%) in 5% HNO_3 for QC

3.2 Instrumentation

To ensure the highest possible accuracy, an Eppendorf Multipette® E3 with combitips was used for all sample preparations.

3.2.1 UV-Vis Spectrophotometry

As previously discussed, the absorbance spectra of different electron configurations of Fe^{2+} and Fe^{3+} were chosen as a differentiator. This was attained by exposing samples to monochromatic electromagnetic radiation while measuring the amount absorbed using an Agilent Technologies Cary 60 UV-Vis spectrophotometry instrument with acid-compatible polymer optical cuvettes (3.5 mL, 1 cm x 1 cm inner dimensions). To hold, change and thermally control the samples, an Agilent Technologies 18 Cell Holder Water Thermo (cell changer) and a PCB 1500 Water Peltier System were used.

3.2.2 ICP-OES

ICP-OES (Agilent Technologies 5110) was used to accurately measure the metal concentrations of the prepared solutions. It was specifically used to determine the concentrations of the ions in the various stock solutions, which can provide higher accuracy compared to that of using mass balance. Such accuracy is especially important when aiming to accurately determine molar absorption constants.

3.3 Experimental procedure

This chapter of the study was divided into five sections. Firstly, the most appropriate wavelength was determined for the analysis of iron ions (Section 4.1), followed by the deduction of the Beer-Lambert Law (Section 4.2) and the determination of both $\varepsilon_{(Fe^{2+})}$ and $\varepsilon_{(Fe^{3+})}$ (Section 4.3 and 4.4, respectively). Finally, the results were validated through experimental error evaluation (Section 4.5). The experimental procedure of each section will be discussed.

3.3.1 Wavelength determination

To establish the most suitable wavelength, two ~1.3 M stock solutions ferrous-chloride and ferric-chloride, respectively, were prepared in 1.00 M HCl (ICRFB operating range). A second set of solutions (factor 100 dilution ~0.013 M) was prepared from the stock solution using aspirating pipettes. Both the stock and the diluted solutions were analysed using UV-Vis spectrophotometry at room temperature, with a scanning rate of 4800 nm min^{-1} from 1100 nm to 200 nm (dual beam mode). A baseline correction obtained from a cuvette containing 1.00M HCl was applied.

Although UV-Vis analysis usually requires samples with concentrations in the range of 0.01 M, the ~1.3 M stock solution was included in this section in view of the envisaged practical implementation of this technique for continuous and real-time in-line monitoring of an ICRFB electrolyte.[30] This implies that deviations from Beer's law could occur and should hence be investigated. Nonetheless, the high concentration stock solutions were included to be able to identify a useful wavelength for both the undiluted and diluted solutions.

3.3.2 Deduction of the Beer-Lambert law

In the first series of experiments, the aim was to determine whether concentration variations from the species originating from the aqueous acidic solvent (HCl) of the electrolyte (see Equation (26)) affect absorption at 920 nm. This was achieved by preparing 5 x 25 mL solutions at 4 different HCl concentrations (0.50, 1.00, 2.00 and 5.00 M) to consist of only electrolyte solvent. Of the five solutions, two were prepared to contain 1.00 M HCl and either N_2 or O_2 were bubbled through them for 10 minutes, in order to determine the possible effect of these dissolved gases on the absorbance. A pure water solution containing no HCl was used as baseline control.

For the next set of experiments, the influence of H^+ and Cl^- concentration variations on the absorption of Fe^{2+}, Fe^{3+} and Cr^{3+} were determined by preparing three 50 mL stock solutions, each containing ~3 M of the respective ion (Fe^{2+}, Fe^{3+} or Cr^{3+}). Exactly 10.00 mL from each of the three stock solutions was combined and diluted to 50.00 mL in a volumetric flask, i.e., diluted 5 times. The quantitative addition of precisely 10.00 mL of each sample (using an electronic pipette) ensured identical ion concentrations of ~0.6 M for Fe^{2+}, Fe^{3+} and Cr^{3+} between samples 1-3 in Table 9. These combined samples were prepared at various HCl concentrations, i.e., 0.50, 1.00 or 2.00 M, resulting in identical samples where only [HCl] was the variable. All iron-containing samples were nitrogenated for at least 10 mins to ensure that Fe^{2+} would not oxidise due to any residual dissolved oxygen. Thirdly, a solution was prepared containing only ~1.4 M Cr^{3+} (Table 9 - sample 4) by dissolving $CrCl_3.4H_2O$ in 1.00 M HCl to determine the absorbance of Cr^{3+}. Lastly, the absorption of two 1 M HCl solutions with and without 5.0 mM bismuth catalyst was compared.

Table 9: Composition and concentrations of samples used for determining the influence of [HCl] on Cr^{3+}, Fe^{2+} and Fe^{3+} absorption of NIR light.

Sample	[HCl] (M)	[Cr^{3+}] (M)	[Fe^{2+}] (M)	[Fe^{3+}] (M)	[Bi^{3+}] (mM)
1	0.50	0.6	0.6	0.6	0.0
2	1.00	0.6	0.6	0.6	0.0
3	2.00	0.6	0.6	0.6	0.0
4	1.00	1.4	0.0	0.0	0.0
5	1.00	0.0	0.0	0.0	0.0
6	1.00	0.0	0.0	0.0	5.0

To measure the absorbance, all the solutions were analysed using the dual beam UV-Vis at 20 °C in the range of 1000 nm to 850 nm NIR light, with a scan rate of 600 nm min^{-1}.

3.3.3 Experimental determination of $\varepsilon_{(Fe^{2+})}$ and $\varepsilon_{(Fe^{3+})}$

Ferrous- and ferric-chloride salts, $FeCl_2$ and $FeCl_3$, respectively, were weighed and dissolved in 1.00 M HCl to create two stock solutions in the range of 1.3 M. Samples of these stock solutions were diluted (1/1000) in 1.00 M HCl and analysed with ICP-OES to determine the exact ion concentrations. For the ICP-OES analysis, six wavelengths (234.350 nm, 258.588 nm, 259.940 nm, 261.187 nm, 273.358 nm, and 275.574 nm) were used to obtain an average concentration (ppm). According to the ICP-OES analysis, the two stock solutions contained 73.40 ppm Fe^{2+} (1.314 M) and 70.84 ppm Fe^{3+} (1.269 M), respectively.

From the two stock solutions, 15 incrementally diluted 10.50 mL samples containing Fe^{2+} and Fe^{3+} were prepared in sealable tubes (to avoid Fe^{2+} from oxidising) using an electronic pipette. From the known concentrations of the stock solutions, the concentration of each dilution was calculated (Table 10).

Table 10: Composition and concentrations of two sets of 15 samples used for determining the molar absorption constants for Fe^{2+} and Fe^{3+}

Sample	Fe^{2+}			Fe^{3+}		
	HCl added (mL)	**Stock added (mL)**	**$[Fe^{2+}]$ (M)**	**HCl added (mL)**	**Stock added (mL)**	**$[Fe^{3+}]$ (M)**
1	10.50	0.00	0	10.50	0	0
2	9.10	1.40	0.175	9.10	1.40	0.169
3	8.40	2.10	0.263	8.40	2.10	0.254
4	7.70	2.80	0.350	7.70	2.80	0.338
5	7.00	3.50	0.438	7.00	3.50	0.423
6	6.30	4.20	0.526	6.30	4.20	0.508
7	5.60	4.90	0.613	5.60	4.90	0.592
8	4.90	5.60	0.701	4.90	5.60	0.677
9	4.20	6.30	0.788	4.20	6.30	0.761
10	3.50	7.00	0.876	3.50	7.00	0.846
11	2.80	7.70	0.964	2.80	7.70	0.931
12	2.10	8.40	1.051	2.10	8.40	1.015
13	1.40	9.10	1.139	1.40	9.10	1.100
14	0.70	9.80	1.226	0.70	9.80	1.184
15	0.00	10.50	1.314	0.00	10.50	1.269

Three mL of each of the 30 samples was analysed using the UV-Vis spectrophotometer in the range of 940 nm to 900 nm using a 300 nm min^{-1} scan rate (dual beam). A baseline correction using 1.00 M HCl was used for all scans. The samples were scanned in the temperature range of 20-45 °C with 5 °C increments using the water Peltier system and sample changer. For each sample, the average of five datapoints, using datapoints from multiple monochromatic

wavelengths, was determined. The wavelengths used were 920.9925 nm, 920.4990 nm, 920.0052 nm, 919.5113 nm and 918.9844 nm, yielding an average wavelength of 919.9985 nm, which in this study will be referred to as 920 nm.

During the heating of the samples, bubbles, probably due to gas-vapour cavities forming, were observed at 45 °C. Since such cavities in the path of the beam could influence the intended absorption of light, no scans were recorded above 45 °C.

3.3.4 Experimental error

To determine the experimental error of the cuvettes and UV spectrophotometer, 16 cuvettes were filled with deionised water before measuring the absorbance at 920 nm and 45 °C. The baseline scan (cuvette sample #1) was done with an empty cuvette, thereby representing not only the interference of absorbance due to gas cavity formations discussed earlier, but also the optical variations between cuvettes.

According to the results (Figure 24), the largest error that was obtained from the instrument between different cuvettes at 45 °C was 0.00263 Abs (0.13 % error in terms of Fe^{2+} absorbance).

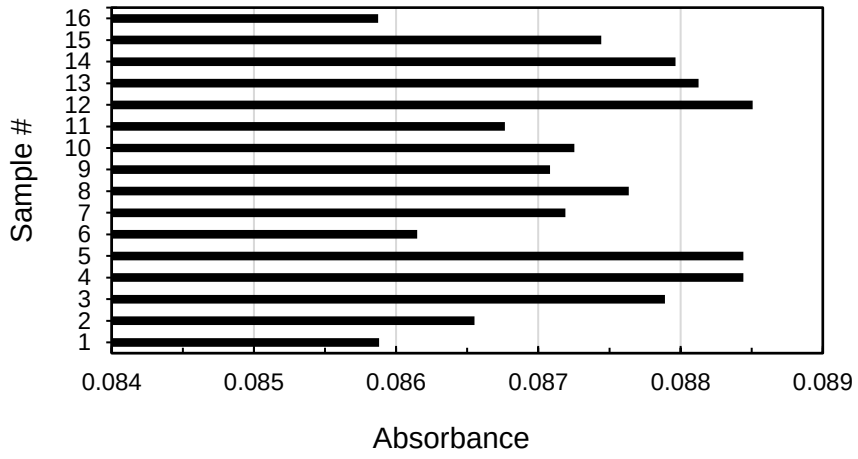

Figure 24: Absorbance of cuvettes containing water (45 °C).

3.3.5 Method validation

To determine the validity of the analytical method, the accuracy thereof in determining Fe^{3+} accumulation had to be assessed. This was approached by using a combination of ICP-OES analysis, UV-Vis analysis and RFB testing.

3.3.5.1 Electrolyte preparation

Two stock solutions, each containing ~1 M Fe^{2+} or ~1 M Fe^{3+} were prepared in 1.0 M HCl using $FeCl_2 \cdot 4H_2O$ and $FeCl_3 \cdot 6H_2O$ (see Section 3.1), respectively. The exact concentrations of the Fe^{2+} and Fe^{3+} stock solutions were determined using ICP-OES analysis by assuming that the purchased ferrous and ferric salts contained only the applicable oxidation state. For analysis, samples of each stock solution were diluted 1000 times with 1.0 M HCl. To simulate imbalance, five 50 mL catholyte samples were prepared from the stock solutions at varying ratios (Table 11), using an electronic pipette (Eppendorf Multipette® E3) to minimise volume measurement errors. It is clear from Table 11 that both the hygroscopic $FeCl_2 \cdot 4H_2O$ and $FeCl_3 \cdot 6H_2O$ salts contained additional absorbed water, which could subsequently be corrected for by analysing the total [Fe]. Four wavelengths were used for Fe analysis (234.350 nm, 238.204 nm, 239.563 nm and 259.940 nm), and an average deviation of 1.64% to 1.93% was obtained for Fe before and after sample measurements, respectively, using the Continuing Calibration Verification (CCV) method. For the purpose of method validation, the $FeCl_2 \cdot 4H_2O$ and $FeCl_3 \cdot 6H_2O$ salts used during catholyte preparations were obtained from different batches than those used for the initial method development.

Table 11: Catholyte ratios and compositions from ICP-OES analysis

Catholyte #	Fe^{2+} : Fe^{3+} Ratio	[Fe^{2+}] from ICP-OES	[Fe^{3+}] from ICP-OES
1	100:0	0.992	0.000
2	80:20	0.794	0.192
3	60:40	0.595	0.383
4	40:60	0.397	0.575
5	20:80	0.198	0.766

Using a baseline correction of 1.00 M HCl, the NIR absorption (900 – 940 nm) of the undiluted positive electrolytes were measured before and after ICRFB cycling at 20 °C (see Section 3.3.5.2), using the UV-Vis spectrophotometer (see Section 3.2.1) at a scan rate (dual beam) of 300 nm min^{-1}.

3.3.5.2 ICRFB Testing station

The catholyte was charged using a lab-scale RFB. The testing station and RFB described in Chapter 3 - Section 2.4.3 and Figure 16 were used, however with a different Potentiostat/Galvanostat (Interface 5000E, Gamry). Additionally, a Nafion 115 PEM membrane was used in the battery to reduce the transfer of Fe/Cr species across the membrane, while the electrolyte solutions were maintained at 65 °C. Graphite felt (SGL, GFA 6) with an active area of 28 cm^2 was used as electrodes. Since heat treating increases the electrochemical activity and hydrophilicity of the felt, while cleaning it from adsorbed chemicals[7,31], the felts used in this study were heat treated at 400 °C for 6 hours prior to the cycling tests. The two electrolytes were circulated through the cell at a flow rate of 50 mL min^{-1} using the pump and acid-compatible Masterflex L/S® Viton tubing. For each experiment involving the charging of a catholyte, a fresh anolyte consisting of a 50 mL solution of 1.0 M HCl + 1.3 M $CrCl_3$ was used. The compositions described in Table 11 were used to prepare the catholytes. No bismuth catalyst was added to this system, as the catholytes underwent one charge cycle each, eliminating the possibility of adding the Bi plating cycle that it would require. The battery was charged at a constant current density of 40 mA cm^{-2} using a cut-off voltage of 1.25 V.

The charging time achieved by catholyte 1 (Table 11) was used as the reference time for catholytes 2-5, which represent imbalanced catholytes containing varying amounts of Fe^{3+} to simulate Fe^{3+} build-up in an ICRFB. Furthermore, the amount of Fe^{2+} for each catholyte (2-5) was used to calculate the target charge capacity. Using an anolyte containing 1.3 M Cr^{3+} ensured that Cr^{3+} was in excess during the catholyte tests.

4. Results and discussion

4.1 Wavelength determination

To ascertain the suitability of UV-Vis for the quantification of iron species in an ICRFB electrolyte, the selective absorption of Fe^{2+} and Fe^{3+} was firstly studied to find a distinct and suitable wavelength for analysis. This was done both for the undiluted stock solutions (~1.3 M Fe^{2+} and Fe^{3+}) and the diluted (100x) solutions (~0.013 M of Fe^{2+} and Fe^{3+}). The results thereof are shown in Figure 25 and Figure 26, respectively. The undiluted stock solution (Figure 25) resulted in absorbance exceeding the instrument's upper limit between 200 nm and 540 nm for both Fe^{2+} and Fe^{3+}, with similar absorption of both at Abs = 3-4. However, in the NIR range (between 800 – 1100 nm), a distinct absorbance peak for Fe^{2+} was observed, reaching a

maximum between 900 and 1000 nm, with no significant absorbance (or distinct peak) for Fe^{3+} in this region.

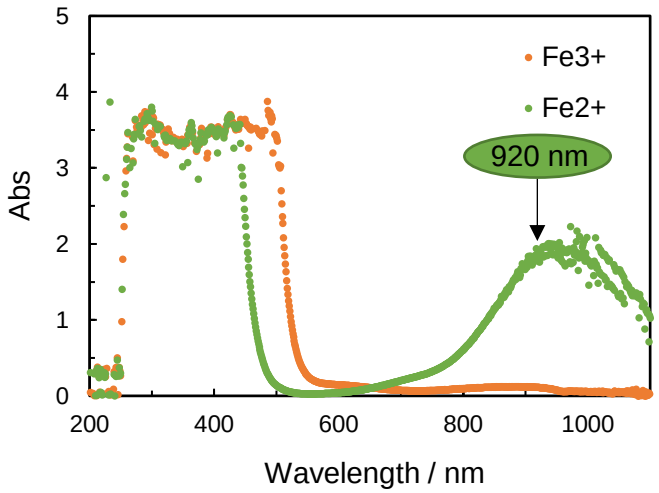

Figure 25: Absorbance spectra of undiluted 1.3 M Fe^{2+} and Fe^{3+} in 1.00 M HCl.

Although the UV range demonstrated possible distinguishing absorbances between Fe^{2+} and Fe^{3+} at 200 – 400 nm when diluted 100x (Figure 26), the absorption was still too strong (Abs = 3-4), exceeding the sensitivity limits of the instrument. It is also clear that the absorbance for the diluted Fe^{2+} was low, irrespective of the wavelength. Maloney *et al., (2005)* observed a strong correlation between the change observed at 320 nm with increasing Fe^{3+} concentrations when studying the conversion of Fe^{2+} to Fe^{3+} in lake water.[32] From both the diluted and undiluted results, it is clear that the absorption for both species of iron at 320 nm light is too strong and exceeds the limits of instrument. In fact, the dilution (Figure 26) only narrowed the absorption range down to the expected 320 nm.[32]

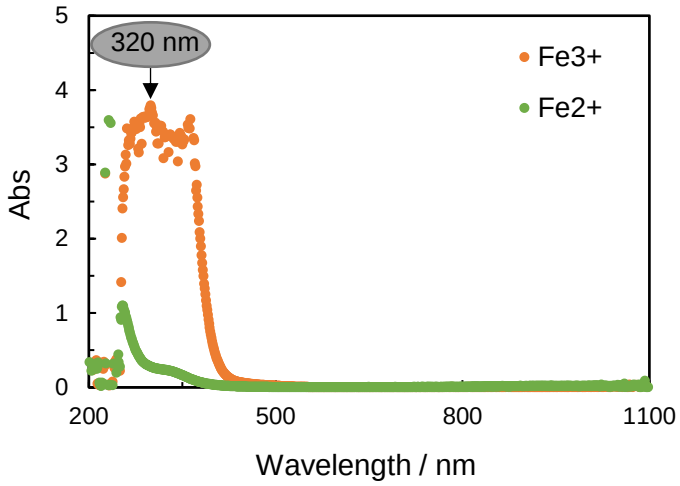

Figure 26: Absorbance spectra of ~0.013 M (100 x dilution) Fe^{2+} and Fe^{3+} in 1.00 M HCl.

Based on the above results, 920 nm was chosen for further analysis as the Fe^{2+} species seemed to dominate absorption (Abs ≈ 2) at this wavelength with limited scattering of data points. Consequently, from Figure 25, it is apparent that measuring absorbance at 920 nm could deliver an accurate measurement of the Fe^{2+} concentration without diluting the sample, making the method suitable for in-line analysis. In addition, if the total dissolved iron concentration of the sample is known, [Fe^{3+}] can simply be obtained by using deduction of the measured [Fe^{2+}] (Equation (27)) from the known total dissolved iron in the electrolyte.

$$z = [Fe^{3+}] + [Fe^{2+}] \quad (27)$$

where z = [Fe_{total}]: the concentration of both dissolved iron species in the positive electrolyte.

4.2 Deduction of the Beer-Lambert law

After identifying a suitable wavelength, the next step entailed determining whether the extended Beer-Lambert law (Equation (26)) could be simplified. Considering the aqueous acidic environment of the electrolyte, the most important species making up the matrix should be H^+, Cl^-, H_2O, H_3O^+ and OH^- ions. Hence, to simplify the equation, the effect of the terms $A(O_2)$, $A(N_2)$, $A(H^+)$, $A(Cl^-)$, $A(H_2O)$, $A(H_3O^+)$ and $A(OH^-)$ on the absorbance was studied experimentally. If these terms equalled zero (no absorbance), or remained constant, they could be removed as a variable from the final equation.

The concentration of H^+ and Cl^- ions in an electrolyte will vary with varying [HCl] and with varying SOCs during battery operation. During battery operation, ions need to cross over the membrane to complete the electric circuit or (to a lesser extent) due to accumulation in the respective half-cell compartments as seen with sulfates in systems using H_2SO_4.[16] It has also been shown that this accumulation of ions in the half-cell matrices of a VRFB can influence the battery monitoring system. To determine the absorbance influence of these ions, the wavelength established in Section 4.1 (920 nm) was used. Since N_2 and O_2 are the most prominent gasses dissolved in the electrolyte, their influences were also studied (Section 4.2).

In the first set of experiments, the influence of N_2, O_2 and the [HCl] in the absence of the Fe and Cr ions on the absorbance at 920 nm was determined. The results are shown in Table 12. From Table 12, it is evident that the largest absorbance difference was obtained between 0.00 M (baseline) and 2.00 M HCl (0.00208 Abs). Compared to the absorbance of Fe^{2+} (~2 Abs) at 920 nm, the deviation due to variations in the H^+ and Cl^- concentrations between 0 and 5 M HCl, as well as the two gasses (N_2 and O_2), was negligible and they were less than the experimental error described in Section 3.3.4.

Table 12: Absorbance at different HCl concentrations (0.500 – 5.00 M).

Sample	**0.500M HCl**	**1.00 M HCl +N_2**	**1.00 M HCl +O_2**	**2.00 M HCl**	**5.00 M HCl**
Abs (920 nm)	-0.00154	0.0000812	-0.000864	-0.00208	-0.00198

An interesting effect observed was that the absorption of the NIR light decreased slightly below the baseline with increasing HCl concentrations (or decreasing pH). This effect was further investigated and illustrated in Figure 27, where the absorbance as a function of the HCl concentration was plotted as a function of the wavelength (850 – 1000 nm). The decrease peaked at about 960 nm. This means that the HCl in the water slightly reduced the absorption, specifically at 960 nm. It should, however, also be noted that the 920 nm chosen above is not influenced by this effect at 960 nm.

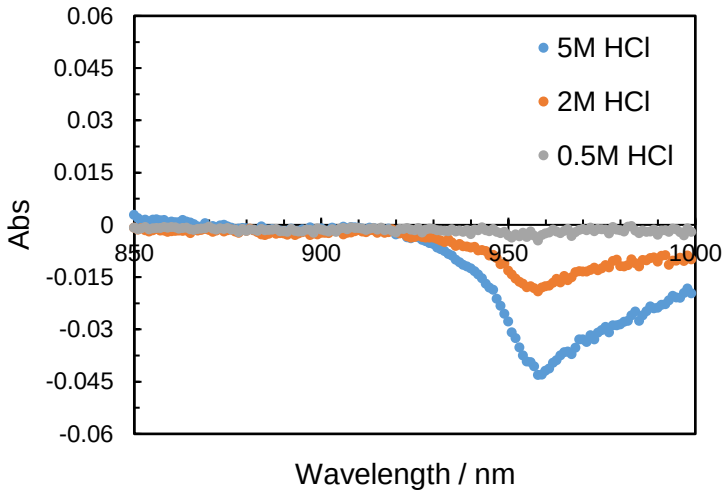

Figure 27: The influence of the HCl concentration on the absorbance between 850 nm and 1000 nm (20 °C).

Even though varying the [HCl] had no significant effect on the UV-Vis absorption at 920 nm when only using water, it is known to influence the absorption of other species in the water, especially when there is dissociation/association (complex formation) or if the change in pH induces changes in electron configurations.[30] The levels to which pH was varied during this investigation may or may not have exceeded the expected H^+ and Cl^- concentration variations during ICRFB operation, which, however, fell beyond the scope of this investigation. While IEMs do allow the balance of the pH of the electrolytes between the half-cells (migration of H^+ or Cl^-), it is known that the pH of VRFB electrolytes (using IEMs) change during cycling.[6] Even when using an organic compound such as TEMPOL (4-hydroxy-2,2,6,6-tetramethyl-1-pipperidinyloxyl) as an electrolyte, pH variations of half-cells were observed.[33] Although the electrolyte composition and charge/discharge mechanics of the TEMPOL RFB and VRFB are very different from that of an ICRFB, it is still useful in showing that an RFB with an aqueous electrolyte and an IEM can experience pH variations in the half-cells during operation. Side reactions during operation may also influence the pH, as shown by Orita *et al*., who observed an initial electrolyte pH of 6.7, which decreased to 4.0 after 50 battery cycles, which was ascribed to the consumption of OH^- from an electrolyte side reaction.[33]

In the second set of experiments, the influence of the [HCl] (also affecting the pH of the solution) on the total absorbance of a mixture containing equimolar concentrations of Fe^{2+}, Fe^{3+} and Cr^{3+} ions (~0.6 M each) was determined. While no changes in the valence of the possible absorbing Fe^{2+}, Fe^{3+} and Cr^{3+} species was expected, the H^+ and Cl^- concentration in the solution could change the sphere of ligands surrounding the metal cations. By changing the polarity of the solution, solvent effects could change the intensity and positions of

absorbance of the species in solution.[30] In Figure 28, the total observed absorbance of the mixture containing the three metals as a function of the [HCl] (0.500 – 2.00 M) is presented. It is clear that, above 900 nm, a higher [HCl] resulted in a slight increase in light absorption. At 920 nm, the absorbance increased slightly from 1.00053 at 0.500 M HCl to 1.03331 at 2.00 M HCl, which resulted in a maximum absorbance deviation of 0.03278. While this value was significantly larger (13 times) than the experimental error (see Section 3.3.4), it was, firstly, significantly smaller than the absorbance of the metal species (~ 1), and secondly, such large [HCl] variations are unlikely during ICRFB operation.

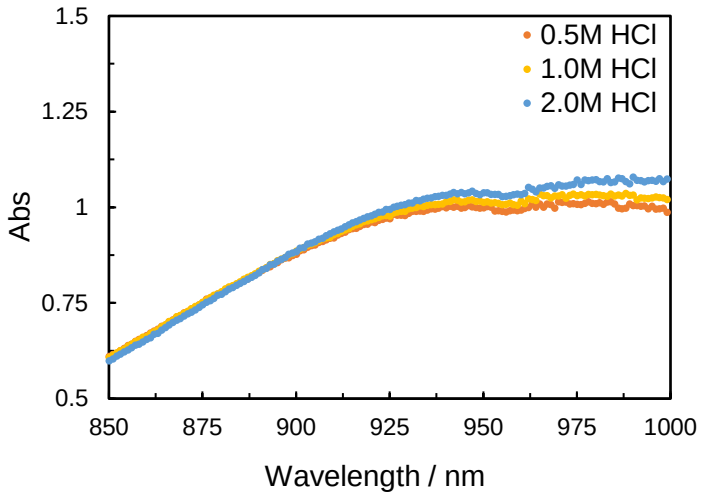

Figure 28: Total absorbance of a mixture containing Fe^{2+}, Fe^{3+} and Cr^{3+} as a function of the HCl concentration (20 °C).

Nonetheless, it could be advisable to investigate variations of pH in electrolytes, specifically during ICRFB operation, to verify their possible effect on absorption during normal ICRFB operation. If this were to pose a problem, the absorbance could still be measured closer to 890 nm, where this effect was hardly noticeable (Figure 28). However, in the absence of a specific ICRFB operational pH range, the choice of the 920 nm wavelength remained as it was closer to the peak of the Fe^{2+} absorbance, while remaining below the noisy region above 940 nm.

Since the [HCl] had no effect on the absorbance (920 nm) in the absence of metal ions, it can be concluded that absorbances due to varying concentrations of H^+, H_3O^+ and OH^- ions during battery operation should have no effect on the accuracy of the Fe^{2+} absorbance. Hence, while the acidic aqueous solution used in the electrolyte might have a molar absorption constant at 920 nm, it is unnecessary to investigate its influence, since any change in molarity (due to pH changes during battery operation) would not exceed that of the experiments mentioned above,

which yielded smaller variations than the experimental error. Since varying the levels of dissolved O_2 and N_2 yielded similar minute changes in absorbance, we can therefore conclude that, at 920 nm, $\varepsilon_{(H^+)}$, $\varepsilon_{(Cl^-)}$, $\varepsilon_{(H_3O^+)}$, $\varepsilon_{(OH^-)}$, $\varepsilon_{(O_2)}$ and $\varepsilon_{(N_2)}$ ≈ 0. Hence, Equation (26) reduces to:

$$A_{total} = A(Fe^{2+}) + A(Fe^{3+}) + A(Cr^{3+}) + A(Bi^{3+}) \quad (28)$$

Finally, the absorbance of Cr^{3+} at 920 nm was investigated by analysing a solution containing ~1.4 M Cr^{3+} as the only metal cation species. Even at this high concentration, a negligible absorbance value of -0.00121 was obtained at 920 nm. Furthermore, assuming there is no significant membrane crossover during battery operation ($\Delta[Cr^{3+}] = 0$), then $\varepsilon_{(Cr^{3+})} = 0$ and $A(Cr^{3+}) = 0$ at 920 nm. Lastly, it was found that electrolyte solvents with bismuth catalysts present at up to 10.0 mM showed no absorption at 920 nm (see Appendix - Figure A 1). Therefore, the Equation (28) can further be simplified and rewritten in terms of Equation (25), yielding Equation (29), expressing the absorbance only in terms of the concentration of the two Fe species present in a hypothetical ICRFB electrolyte.

$$\frac{A_{obs}}{b} = \varepsilon_{(Fe^{2+})}[Fe^{2+}] + \varepsilon_{(Fe^{3+})}[Fe^{3+}] \quad (29)$$

4.3 Experimental determination of $\varepsilon_{(Fe^{2+})}$

According to Equation (29), $\varepsilon_{(Fe^{2+})}$ is required for a final approximation of the amount of Fe^{2+} present. Hence, in this section, this term was quantified experimentally, keeping in mind that $\varepsilon_{(Fe^{2+})}$ will only be constant when the Beer-Lambert law holds, which might, however, deviate considering the high concentrations of the analysed solutions used.[34] Assuming that $\varepsilon_{(Fe^{2+})}$ might not be constant, the coefficient of determination (R^2) was used as a verification of the linear relationship between concentration and absorbance, thus indicating if the Beer-Lambert law held. In this section, the effect of both the iron concentration and the temperature was investigated since ICRFBs could be operated at different temperatures.

In Figure 29, the influence of the Fe^{2+} concentration (0.00 – 1.30 M) on the absorbance is presented. Although concentrations of ≥ 1.3 M are usually considered high for UV-Vis spectrophotometry, it is clear from Figure 29 that the absorbance as a function of [Fe^{2+}] yielded an almost perfectly linear plot (R^2 = 0.9999) for the investigated concentration range. The strong linear relationship at 920 nm light between the absorbance of Fe^{2+} in an HCl matrix and

the [Fe^{2+}] confirms that the Beer-Lambert law holds at concentrations as high as 1.3 M. Accordingly, a constant $\varepsilon_{(Fe^{2+})}$ = 1.50039 mol^{-1} dm^3 cm^{-1} ± 0.021 was obtained at 20 °C.

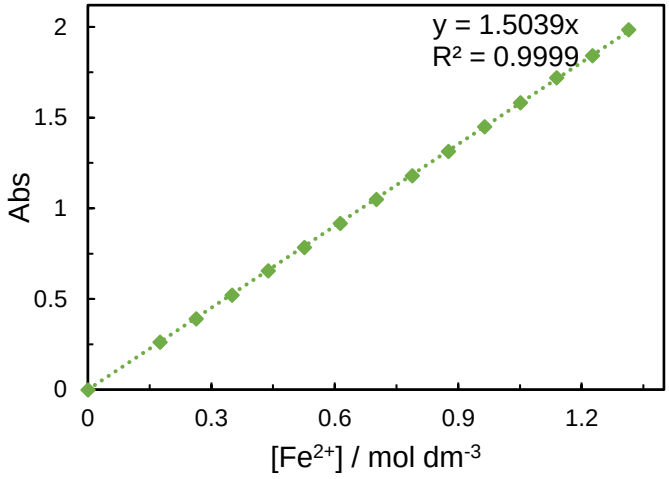

Figure 29: Absorbance at 920 nm of Fe^{2+} at different concentrations (20 °C).

In the second experiment, the influence of the temperature on the absorbance of Fe^{2+} as a function of its concentration was investigated by varying the temperature between 20 °C and 45 °C (maximum temperature before vapour cavities formed in the cuvette, influencing light absorption). In the absence of any iron, the 920 nm absorbance increased by 0.001099 with increasing temperature, which falls below the experimental error.

According to Figure 30, the absorbance as a function of Fe^{2+} concentration at all the temperatures investigated yielded an R^2 of 0.9999, confirming a linear data series. Although the data series at different temperatures seemed close to each other, an increase in temperature from 20 °C to 45 °C caused an increase in $\varepsilon_{(Fe^{2+})}$ from 1.5039 to 1.5739, which contributes to a deviation in the total absorbance of 4.45%. This deviation of $\varepsilon_{(Fe2+)}$ from 20 °C is significant as it is common for ICRFBs to operate at higher temperatures than 45 °C to allow higher charge efficiencies by shifting the equilibrium from the inactive to the active chromium species in the negative electrolyte.[35] Since the increase of $\varepsilon_{(Fe^{2+})}$ due to temperature amounts to 0.15% per °C, the error between absorbance and [Fe^{2+}] will be significant at ICRFB operating temperatures.

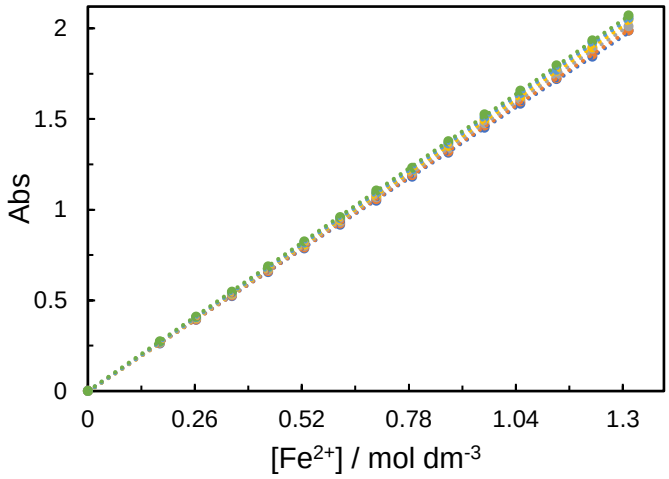

Temperature (°C)	20	25	30	35	40	45
Slope	1.5039	1.5126	1.5302	1.5459	1.5601	1.5739

Figure 30: Absorbance of Fe^{2+} at 920 nm at different concentrations and temperatures.

However, by plotting the $\varepsilon_{(Fe^{2+})}$ as a function of temperature (Figure 31), a linear function was obtained (y = 0.0029x + 0.6523), which can hence be used to compensate for the influence of temperature on the absorbance of Fe^{2+}. Since the influence of temperature on $\varepsilon_{(Fe^{2+})}$ can be represented linearly with an R^2 of 0.9955, and assuming this linearity to continue, $\varepsilon_{(Fe^{2+})}$ could be calculated for temperatures above 45 °C.

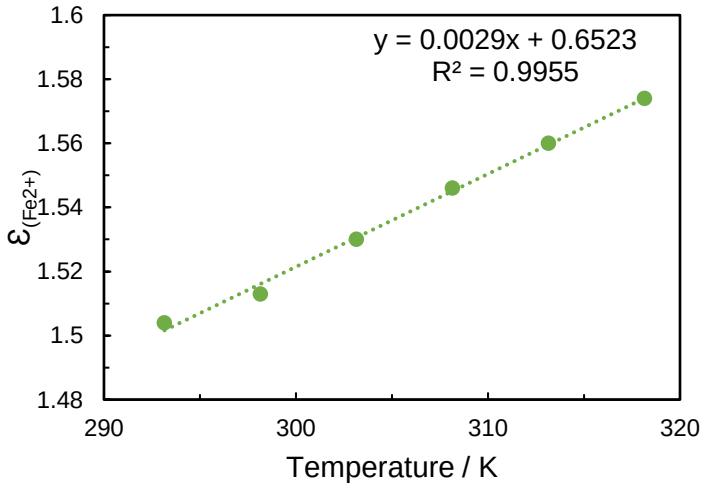

Figure 31: $\varepsilon_{(Fe^{2+})}$ from 293.15-318.15 K.

Using the linear regression obtained from Figure 31 (y = 0.0029x + 0.6523), $\varepsilon_{(Fe^{2+})}$ can now be expressed as a function of temperature (T):

$$\varepsilon_{(Fe^{2+})} = 0.0029(T)\ mol^{-1}\ dm^3\ cm^{-1}\ K^{-1} + 0.6523\ mol^{-1}\ dm^3\ cm^{-1} \quad (30)$$

4.4 Experimental determination of $\varepsilon_{(Fe^{3+})}$

According to Figure 25 (Section 4.1), 1.3 M Fe^{3+} absorbed 0.115 at 920 nm, which is 5.75% of the total Fe absorbance (~2). This confirms that the absorption of Fe^{3+} does influence the total absorbance considerably and since the [Fe^{3+}] will vary intrinsically during ICRFB operation, its influence should be examined. Hence, similarly to determining $\varepsilon_{(Fe^{2+})}$ in Section 4.3, a value for $\varepsilon_{(Fe^{3+})}$ was sought in this section. Since Fe^{3+} absorbs significantly less light at 920 nm than Fe^{2+}, a larger error due to instrument sensitivity and signal-to-noise ratios was expected, which was confirmed by the deviations from the straight line shown in Figure 31. The straight-line equation confirms a possible quadratic behaviour caused by Beer-Lambert law deviations due to the high concentrations used. However, even with a standard deviation of 7.8% for $\varepsilon_{(Fe^{3+})}$, this deviation might still be negligible, considering that the maximum values of Fe^{3+} absorbance (at 20 °C) compared to Fe^{2+} absorbance was less than 7.3%.

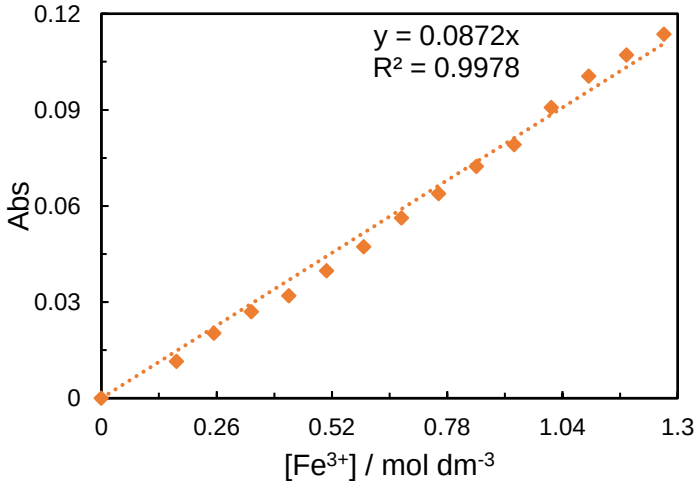

Figure 32: Absorbance of Fe^{3+} at different concentrations (20 °C).

When investigating the effect of temperature on the absorbance of Fe^{3+} (Figure 33), it became apparent that a temperature increase caused a reduction in absorbance at lower Fe^{3+} concentrations. A possible explanation to this effect, which should be investigated further, is that varying [Fe^{3+}] in 1.00 M HCl contributes to changes in the ligand sphere of the dissolved complex, which might result in minute changes in the observed absorbance. This decrease in absorbance at low concentrations, however, only caused slight shifts in linearities since the regressions were forced to intercept at 0. Hence the slopes ($\varepsilon_{(Fe^{3+})}$) of these plots are very similar with no clear temperature dependency. The maximum absolute error of $\varepsilon_{(Fe3+)}$, present between 30 °C and 40 °C, computed to only 2.31%. However, if the regression was not forced through 0, the slope would increase on average with 0.00078 mol^{-1} dm^3 with every 5 °C, which computes to 0.89% of the 0.0872 mol^{-1} dm^3 at 20 °C and 8.01% at 65 °C. This error becomes smaller (0.47%) in the scope of the dominant Fe^{2+} absorbance by a factor of 17. However, the issue with not forcing the intercept through 0 is that the measurements of samples with low concentrations (<~0.2 M) of Fe^{3+} will be inaccurate, while the function will also not be able to accommodate ~0 M Fe^{3+}. While using a polynomial regression (fit not shown) yielded slight improvements to the R^2 values (lowest R^2 of 0.998), the drastic increase in complexity in the function approximating [Fe^{2+}] was not worth the small improvement made towards the fit of the regression.

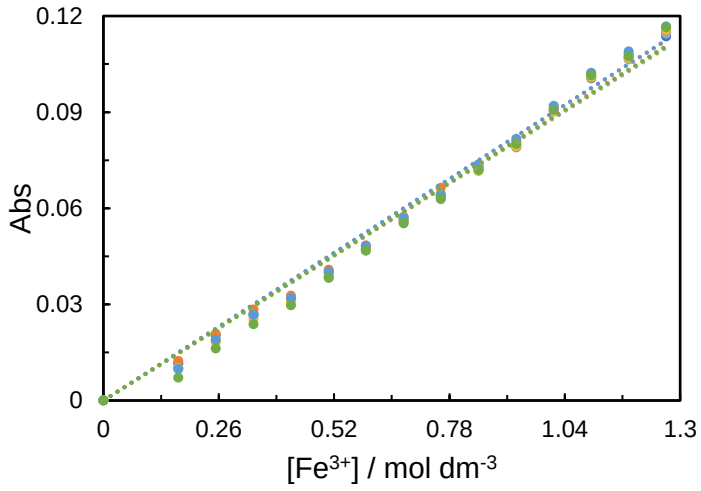

Temperature (°C)	20	25	30	35	40	45
Slope	0.0872	0.0886	0.0867	0.0872	0.0887	0.0871
R^2	0.998	0.998	0.997	0.9965	0.9971	0.9948

Figure 33: Absorbance of Fe^{3+} at 920 nm at different concentrations and temperatures.

Using a linear regression with a forced intercept at 0 hence seemed like the best solution for modelling the relationship of [Fe^{3+}] and absorbance to produce a function with an accurate [Fe^{2+}] approximation. Additionally, this linear regression approach does not require any addition of complexity to accommodate the effect of temperature, as it assumes no clear correlation between absorbance and temperature within the analysed ranges. The value for $\varepsilon_{(Fe^{3+})}$ can therefore be obtained from the average of the analysed ranges as 0.0876 mol^{-1} dm^3 cm^{-1}. When using this value to approximate [Fe^{3+}] values and comparing it to the data obtained, the largest error obtainable was an absorbance value of 0.00964, which was four times larger than the experimental error. Although this value was bigger than the experimental error, it seemed insignificant when considering that Fe^{3+} absorbance values were significantly smaller than Fe^{2+} absorbance values, with a lower signal-to-noise ratio than Fe^{2+} absorbance. Accordingly, $\varepsilon_{(Fe^{3+})}$ was taken as a constant (independent of temperature changes) using the average of the slopes from 20 °C to 45 °C obtained with linear regression intercepting at 0 (Figure 33), yielding Equation (31):

$$\varepsilon_{(Fe^{3+})} = 0.0876\, mol^{-1}.dm^3.cm^{-1} \tag{31}$$

4.5 Final approximation for [Fe^{2+}]

Based on the values and functions derived experimentally for $\varepsilon_{(Fe^{2+})}$ and $\varepsilon_{(Fe^{3+})}$, a function can be obtained for monitoring the [Fe^{2+}] in the positive electrolyte of an ICRFB by substituting Equations (30) and (31) into Equation (29), yielding Equation (32):

$$\frac{A_{obs}}{b} = 0.0029(T)[Fe^{2+}]\, mol^{-1}\, dm^3\, cm^{-1}\, K^{-1} + 0.6523[Fe^{2+}] mol^{-1}\, dm^3\, cm^{-1} + 0.0876\, mol^{-1}\, dm^3\, cm^{-1}[Fe^{3+}] \tag{32}$$

The [Fe^{3+}] can be rewritten in terms of [Fe^{2+}] by substituting Equation (27) into Equation (32), delivering Equation (33):

$$\frac{A_{obs}}{b} = 0.0029(T)[Fe^{2+}]\, mol^{-1}\, dm^3\, cm^{-1}\, K^{-1} + 0.6501[Fe^{2+}]\, mol^{-1}\, dm^3\, cm^{-1} + 0.08758 mol^{-1}\, dm^3\, cm^{-1}(z\, mol\, dm^{-3} - [Fe^{2+}]) \tag{33}$$

By factorising Equation (33), Equation (34) is obtained, where the [Fe^{2+}] is defined as a function of the obtained absorbance:

$$\left[\boldsymbol{Fe^{2+}}\right] = \frac{\frac{A_{obs}}{b} - 0.0876(z)\, cm^{-1}}{0.00290(T)\, mol^{-1}\, dm^3\, cm^{-1}\, K^{-1} + 0.563\, mol^{-1}\, dm^3\, cm^{-1}} \tag{34}$$

Irrespective of the ICRFB electrolyte being prepared, *z* will be known since synthesising the electrolyte would require knowledge of the desired and required concentration that usually does not exceed 1 M.[4] However, even if the concentration was unknown for some or other reason, it could simply be obtained using for example ICP-OES to yield an accurate value of z.

5. Method validation

The five catholytes with varying Fe^{2+}/Fe^{3+} ratios (Table 11), simulating imbalance from Fe^{3+} accumulation, were analysed with ICP-OES and compared to the results obtained from applying the developed function (Equation (34)) to the UV-Vis (NIR absorption) data. The results of the NIR absorption measurements (900 – 940 nm) for the five catholytes are presented in Figure 34. As hoped, the absorbance spectra of the different ratios were evenly spaced, with the absorbances decreasing with decreasing Fe^{2+} content, irrespective of the wavelength.

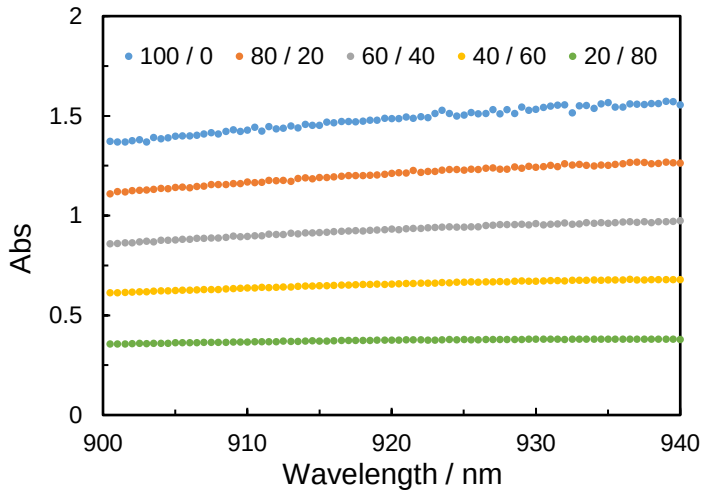

Figure 34: Absorbance of catholytes 1-5 with varying Fe^{2+}/Fe^{3+} ratios between 900 nm and 940 nm, prior to RFB charge cycles (20 °C).

The obtained absorbance values for catholytes 1-5, the ICP-OES values and the absolute differences between these values for both Fe^{2+} and Fe^{3+} are presented in Table 13. The results show that the largest absolute error was obtained for $[Fe^{2+}]$ (3.33%), which increased as the $[Fe^{2+}]$ decreased. The increased error is likely due to the fact that, during the approximation development, the absorption of Fe^{2+} at 920 nm was much higher than that of Fe^{3+} (factor of

>15). The absolute error for [Fe^{3+}] did not show any distinguishable trend, where the largest error (3.08%) was observed at an Fe^{2+}/Fe^{3+} ratio of 60/40 (catholyte #3).

Table 13: ICP-OES and UV-Vis results with NIR analysis method/function error for catholytes 1-5 prior to RFB charge cycles.

	Catholyte # and Fe^{2+}/Fe^{3+} ratios				
	#1 100 / 0	**#2 80 / 20**	**#3 60 / 40**	**#4 40 / 60**	**#5 20 / 80**
[Fe^{2+}] from ICP-OES	0.992	0.794	0.595	0.397	0.198
[Fe^{3+}] from ICP-OES	0.000	0.192	0.383	0.575	0.766
[Fe^{2+}] (UV-Vis) NIR	0.991	0.795	0.597	0.404	0.205
[Fe^{3+}] (UV-Vis) NIR	0.001	0.197	0.395	0.588	0.787
Abs. error [Fe^{2+}] (%)	0.10	0.18	0.30	1.81	3.33
Abs. error [Fe^{3+}] (%)	0.00	2.82	3.08	2.30	2.69

After the comparison of the UV-VIS and the ICP-OES data, the catholytes underwent a single RFB charge cycle to compare the charge curve to the NIR absorption data. In Figure 35 the RFB charge time for catholytes 1-5 are presented as a function of the potential obtained from the work electrode. It is clear that the charge curves obtained from each catholyte are evenly spaced, with the time to reach the cut-off voltage of 1.25 V for the catholyte decreasing with decreasing [Fe^{2+}]. This decrease in time represents a direct decrease in charge capacity (or storage capacity), conferring that the capacity of the synthetically imbalanced electrolytes decreased as the [Fe^{3+}] increased.

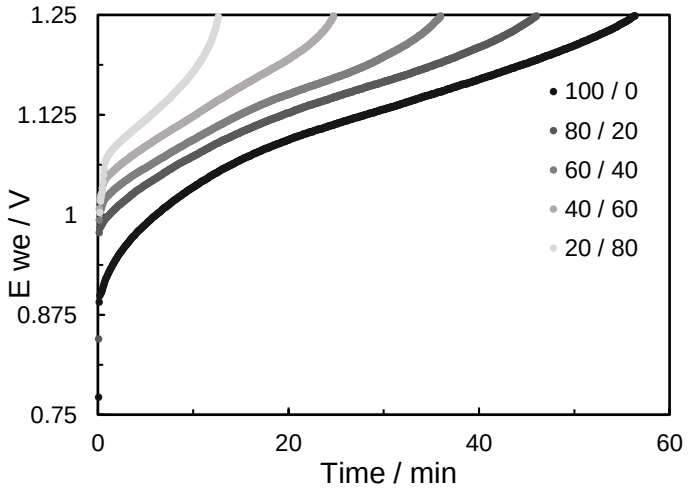

Figure 35: RFB charge curves of catholytes 1-5 with 1.3 M Cr^{3+} anolyte (65 °C).

The capacity (Q_{cap}) used of a catholyte can be calculated using Faraday's law (Equation (35)),[36]

$$Q_{cap} = \frac{nF}{3600\ s\ h^{-1}} \quad (35)$$

where n = the moles of active species in the electrolyte and F = Faraday's constant (96485 C). Since the amount of available Cr^{3+} at the anolyte exceeded the amount of available Fe^{2+}, the charge capacity during charging of a catholyte was limited by the amount of available Fe^{2+} that could supply electrons. Therefore, the $Q_{cap(charge)}$ values obtained during battery cycling were directly proportional to the amount of Fe^{2+} used. Using this approach, the capacity use of Catholyte 1 was determined and used to calculate the target $Q_{cap(charge)}$* values to draw a correlation between RFB cycles and the simulated imbalance in catholytes (2-5). The charge time, $Q_{cap(charge)}$, $Q_{cap(charge)}$* and the error of the two charge values are presented in Table 14. While the target capacity values appear similar, it is clear that the absolute error between $Q_{cap(charge)}$ and $Q_{cap(charge)}$* increased as [Fe^{2+}] decreased ([Fe^{3+}] increased), reaching an error of 12.38% for catholyte 5. However, when considering the ICRFB redox reactions (Section 1) combined with the Nernst equation (Equation (36)), it is clear that the OCV voltage at the end of the charging cycle of each electrolyte (1-5 in Table 11) will decrease due to the increasing amount of remaining Cr^{3+}.[37] In Equation (36), the magnitude of the negative potential (E) decreases with increasing [Cr^{3+}] and decreasing [Cr^{2+}], which means that a cycle in an RFB with a catholyte containing less Fe^{2+} available to reduce the Cr^{3+} present might take longer to reach the cut-off potential of 1.25 V.

Table 14: RFB charge times and capacity for catholytes 1-5.

	Catholyte # and Fe^{2+}/Fe^{3+} ratios				
	#1	**#2**	**#3**	**#4**	**#5**
	100 / 0	**80 / 20**	**60 / 40**	**40 / 60**	**20 / 80**
Charge time (min)	56.35	46.00	35.95	24.72	12.63
$Q_{cap(charge)}$ (A h)	1.052	0.859	0.671	0.461	0.236
$Q_{cap(charge)}$ (A h)*	1.052	0.842	0.631	0.421	0.210
Abs. error (%)	0.00	2.02	6.34	9.50	12.38

$Q_{cap(charge)}$ (A h)* = Target charge capacity as calculated from the charge time of catholyte #1

The Nernst equation can be used to determine the theoretical potential of the anolyte,[37]

$$E = E^0 - \frac{RT}{nF} ln\left\{\frac{[Cr^{2+}]}{[Cr^{3+}]}\right\} \quad (36)$$

where E^0 = the standard electrode potential (V), R = ideal gas constant 8.314 J K^{-1} mol^{-1}, T = temperature (K), n = number of moles of electrons in the half-reaction and F = Faraday's

constant (96485 C). According to Equation (36), it is likely that the observed error increase in Table 13 is caused by the Nernst potential introduced by the increasing [Cr^{3+}] in the anolyte, incrementally extending the charge times to the cut-off potential of 1.25 V by lowering the cell OCV.

This theory is supported by the UV-Vis analysis of the catholytes after charging, as shown in Figure 36. When comparing the absorbance values of the uncharged (Figure 34) to the charged (Figure 36) catholytes, it is clear that the charged catholyte samples all had lower absorbance values (<0.22 Abs at 920 nm) than the uncharged electrolytes. This observed decrease in absorption is a direct result of the decrease in [Fe^{2+}] and increase in [Fe^{3+}] during charging. It is also clear that each catholyte with less charge time was able to charge deeper, meaning less Fe^{2+} remained after reaching a cut-off voltage of 1.25 V. The deeper charging correlates to the expected lowering of OCV caused by the Nernst potential of [Cr^{3+}] remaining after a charge cycle.

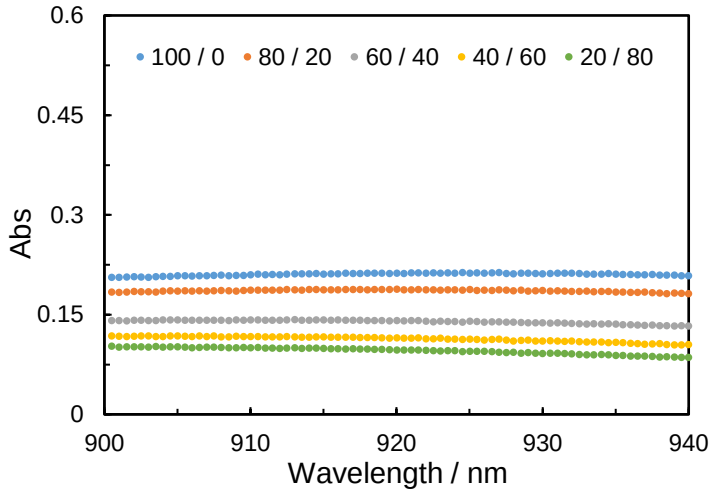

Figure 36: Absorbance of catholytes 1-5 with varying Fe^{2+}/Fe^{3+} ratios between 900 and 940 nm, after RFB charge cycles (20 °C).

In summary, correlations between RFB cycles and Fe^{2+}/Fe^{3+} concentrations were obtained using the developed UV-Vis method. However, significant errors (12.38%) were observed, which were ascribed to the effect of the Nernst potentials. Nonetheless, the largest error obtained for the method's accuracy with ICP-OES was 3.33%. It is worthy to note that this error was probably increased by the assumption that the $FeCl_2$ used was 100% pure, i.e. containing no Fe^{3+}, which was probably closer to 99%. However, this could not be confirmed since the ICP-OES cannot distinguish between Fe^{2+} and Fe^{3+}.

6. Conclusions

In this study, it was attempted to derive a function that, when used with a fast and non-destructive analytical method, could accurately approximate a value for the concentration of Fe^{2+}, which is necessary to monitor the imbalance of an ICRFB system. When investigating the effects of temperature on NIR absorption, a strong linear relationship with Fe^{2+} absorption in an HCl matrix was observed. After investigating the NIR absorption of [HCl] and other species in an ICRFB electrolyte, only the absorption of Fe^{2+} and Fe^{3+} was found to be significant. There were some indications that [HCl] could have a small effect on NIR absorption, which could be avoided by using 890 nm NIR, but the significance of [HCl] variations should first be investigated in an ICRFB. After thorough investigation and quantification of the most important factors that could influence NIR absorption, a function that approximates $[Fe^{2+}]$ with absorbance, with a maximum error of 3.33%, was obtained, which allows an accurate approximation of $[Fe^{3+}]$, with a maximum error of 3.08%, if the total [Fe] is known. It was stated initially that imbalance in an ICRFB results in an increased $[Fe^{3+}]$ changing the Fe^{2+}/Fe^{3+} ratio over time. This study provided a method to instantaneously measure the imbalance of an ICRFB by only analysing a stream of the electrolyte with monochromatic NIR light, which can be done in-line and continuously.

7. References

1. Ling, J. S.; Charleston, J. *Advances in Membrane Technology for the NASA Redox Energy Storage System*; NASA TM-82701; NASA Lewis Research Center Cleveland, OH, United States: 1980.
2. Hagedorn, N. H. *NASA Redox Storage System Development Project. Final Report*; National Aeronautics and Space Administration, Cleveland, OH (USA). Lewis Research Center: 1984.
3. Thaller, L. H. *Recent advances in Redox Flow Cell Storage Systems*; NASATM-79186; NASA Lewis Research Center Cleveland, OH, United States: 1979.
4. Sun, C.; Zhang, H., Review of the Development of First-Generation Redox Flow Batteries: Iron-Chromium System. *ChemSusChem* **2021,** *15* (1), 15.
5. Wei, W.; Qingtao, L.; Bin, L.; Xiaoliang, W.; Liyu, L.; Zhenguo, Y., Recent Progress in Redox Flow Battery Research and Development. *Advanced Functional Materials* **2013,** *23* (8), 970-986.
6. Weber, A. Z.; Mench, M. M.; Meyers, J. P.; Ross, P. N.; Gostick, J. T.; Liu, Q., Redox flow batteries: a review. *Journal of Applied Electrochemistry* **2011,** *41* (10), 1137-1164.
7. Zeng, Y. K.; Zhao, T. S.; An, L.; Zhou, X. L.; Wei, L., A comparative study of all-vanadium and iron-chromium redox flow batteries for large-scale energy storage. *Journal of Power Sources* **2015,** *300*, 438-443.
8. Wang, W.; Nie, Z.; Chen, B.; Chen, F.; Luo, Q.; Wei, X.; Xia, G.; Skyllas-Kazacos, M.; Li, L.; Yang, Z., A New Fe/V Redox Flow Battery Using a Sulfuric/Chloric Mixed-Acid Supporting Electrolyte. *Advanced Energy Materials* **2012,** *2* (4), 487-493.
9. Fares, A. I.; Sohel, K. M. A.; Al-Jabri, K.; Al-Mamun, A., Characteristics of ferrochrome slag aggregate and its uses as a green material in concrete – A review. *Construction and Building Materials* **2021,** *294*, 123552.
10. Ren, S.; Li, H.; Wang, Y.; Guo, C.; Feng, S.; Wang, X., Comparative study of the China and U.S. import trade structure based on the global chromium ore trade network. *Resources Policy* **2021,** *73*, 102198.
11. Gann, R. F.; Hagedorn, N. H.; Johnson, J. A. *Cycling Performance of the Iron-Chromium Redox Energy Storage System*; NASA TM-87034; NASA Lewis Research Center Cleveland, OH, United States: 1985.
12. Zeng, Y. K.; Zhao, T. S.; Zhou, X. L.; Zou, J.; Ren, Y. X., A hydrogen-ferric ion rebalance cell operating at low hydrogen concentrations for capacity restoration of iron-chromium redox flow batteries. *Journal of Power Sources* **2017,** *352*, 77-82.

13. Skoog, D. A.; West, D. M.; Holler, F. J.; Crouch, S. R., *Fundamentals of analytical chemistry*. Ninth edition. ed.; Brooks/Cole, Cengage Learning: Belmont, CA, 2014; p A12-A14.
14. Jirabovornwisut, T.; Arpornwichanop, A., A review on the electrolyte imbalance in vanadium redox flow batteries. *International Journal of Hydrogen Energy* **2019,** *44* (45), 24485-24509.
15. Liu, L.; Xi, J.; Wu, Z.; Zhang, W.; Zhou, H.; Li, W.; Qiu, X., State of charge monitoring for vanadium redox flow batteries by the transmission spectra of V(IV)/V(V) electrolytes. *Journal of Applied Electrochemistry* **2012,** *42* (12), 1025-1031.
16. Corcuera, S.; Skyllas-Kazacos, M., State-of-Charge Monitoring and Electrolyte Rebalancing Methods for the Vanadium Redox Flow Battery. *European Chemical Buletin* **2012,** *1*, 511-519.
17. Achterberg, E. P.; Holland, T. W.; Bowie, A. R.; Fauzi, R.; Mantoura, C.; Worsfold, P. J., Determination of iron in seawater. *Analytica Chimica acta* **2001,** *442* (1), p 1-14.
18. Jeitner, T. M., Optimized ferrozine-based assay for dissolved iron. *Analytical Biochemistry* **2014,** *454*, 36-37.
19. Bolster, K.; Heller, M.; Moffett, J., Determination of iron(II) by chemiluminescence using masking ligands to distinguish interferences. *Limnology and Oceanography: Methods* **2018,** *16*, 10.
20. Lin, M.; Hu, X.; Pan, D.; Han, H., Determination of iron in seawater: From the laboratory to in situ measurements. *Talanta* **2018,** *188*, 135-144.
21. Yan, X.-P.; Hendry, M. J.; Kerrich, R., Speciation of Dissolved Iron(III) and Iron(II) in Water by On-Line Coupling of Flow Injection Separation and Preconcentration with Inductively Coupled Plasma Mass Spectrometry. *Analytical Chemistry* **2000,** *72* (8), 1879-1884.
22. Skyllas-Kazacos, M.; Kazacos, M., State of charge monitoring methods for vanadium redox flow battery control. *Journal of Power Sources* **2011,** *196* (20), 8822-8827.
23. Shin, K.-H.; Jin, C.-S.; So, J.-Y.; Park, S.-K.; Kim, D.-H.; Yeon, S.-H., Real-time monitoring of the state of charge (SOC) in vanadium redox-flow batteries using UV–Vis spectroscopy in operando mode. *Journal of Energy Storage* **2020,** *27*, 101066.
24. Persson, I., Ferric Chloride Complexes in Aqueous Solution: An EXAFS Study. *J Solution Chem* **2018,** *47* (5), 797-805.
25. Bull, J. N.; Maclagan, R. G. A. R.; Fitchett, C. M.; Tennant, W. C., A new isomorph of ferrous chloride tetrahydrate: A 57Fe Mössbauer and X-ray crystallography study. *Journal of Physics and Chemistry of Solids* **2010,** *71* (12), 1746-1753.

26. Atkins, P.; Armstrong, F.; Hagerman, M.; Overton, T.; Rourke, J.; Weller, M., *Shriver & Atkins' Inorganic Chemistry*. W. H. Freeman and Company: 41 Madison Avenue, New York, NY 10010, 2010; Vol. 5th Edition, p 483-488.
27. Pavia, D. L.; Lampman, G. M.; Kriz, G. S.; Vyvyan, J. R., *Introduction to spectroscopy*. 4 ed.; 2009, 2001 Brooks/Cole, Cengage Learning: 2009; p 381-413.
28. Atkins, P.; de Paula, J., *Physical Chemistry: Thermodynamics, Structure, and Change*. 10th ed.; Oxford University Press: 2014; p 479-480.
29. Zeng, Y. K.; Zhao, T. S.; Zhou, X. L.; Zeng, L.; Wei, L., The effects of design parameters on the charge-discharge performance of iron-chromium redox flow batteries. *Applied Energy* **2016,** *182*, 204-209.
30. Skoog, D. A.; West, D. M.; Holler, F. J.; Crouch, S. R., *Fundamentals of analytical chemistry*. Ninth edition. ed.; Brooks/Cole, Cengage Learning: Belmont, CA, 2014; p 658-674 & 722-738.
31. Kim, S.; Thomsen, E.; Xia, G.; Nie, Z.; Bao, J.; Recknagle, K.; Wang, W.; Viswanathan, V.; Luo, Q.; Wei, X.; Crawford, A.; Coffey, G.; Maupin, G.; Sprenkle, V., 1 kW/1 kWh advanced vanadium redox flow battery utilizing mixed acid electrolytes. *Journal of Power Sources* **2013,** *237*, 300-309.
32. Maloney, K. O.; Morris, D. P.; Moses, C. O.; Osburn, C. L., The Role of Iron and Dissolved Organic Carbon in the Absorption of Ultraviolet Radiation in Humic Lake Water. *Biogeochemistry* **2005,** *75* (3), 393-407.
33. Orita, A.; Verde, M. G.; Sakai, M.; Meng, Y. S., The impact of pH on side reactions for aqueous redox flow batteries based on nitroxyl radical compounds. *Journal of Power Sources* **2016,** *321*, 126-134.
34. Braithwaite, A.; Smith, J. F., *Chromatographic Methods*. 5 ed.; Springer Science & Business Media: 2012.
35. Johnson, D. A.; Reid, M. A., Chemical and Electrochemical Behavior of the Cr(III)/Cr(II) Half-Cell in the Iron-Chromium Redox Energy Storage System. *Journal of The Electrochemical Society* **1985,** *132* (5), 1058-1062.
36. Zhang, H.; Li, X.; Zhang, J., *Redox Flow Batteries: Fundamentals and Applications.* CRC Press: 2017.
37. Skoog, D. A.; West, D. M.; Holler, F. J.; Crouch, S. R., *Fundamentals of analytical Chemistry*. Ninth edition ed.; Brooks/Cole, Cengage Learning: Belmont, CA, 2014; p 442-469.

CHAPTER 5

EVALUATION AND RECOMMENDATIONS

In Chapter 1, it was stated that the aim of the study was to contribute to the development of ICRFB technology to make it a more feasible LESS. Two objectives were identified; firstly, to develop a suitable and cheap method for the purification of $FeCl_2$, thereby reducing the cost of the electrolyte (Chapter 3) and secondly, to develop a simple method to monitor battery imbalance and rebalancing (Chapter 4). The outcomes of the purification process and the development of the analytical technique are evaluated in this Chapter's Sections 1 and 2, respectively, providing recommendations for each step.

1. Purification procedure for $FeCl_2$

When assessing the suitability of the purification process, there are three key objectives that should be discussed: i) the impurity removal, as well as ii) the simplicity and iii) economic viability of the process. In this evaluation, these three topics will be critically assessed (Section 1.1-1.3) by stating the original goals before discussing if and how they were addressed. Finally, recommendations will be made on how these objectives may be addressed further.

1.1 Impurity removal

Firstly, any purification process, as the name states, should remove dissolved metal impurities that might be present in chemicals obtained either from mining or production processes. To be suitable as an RFB electrolyte, the removal of the impurities should result in a substantial performance increase during battery cycling. Ideally, the obtained performance should be comparable to an electrolyte that contains commercial, laboratory-grade $FeCl_2$ that is commonly used for battery testing, thereby showing that those contaminants that specifically affect cell performance have been removed. According to the literature on VRFB research, the most important impurities, or metals of concern, are Cu, Ni and Sn, which all promote the unwanted HER in acidic aqueous electrolyte systems.

From the ICP-OES results, it became clear that the concentration of most of the dissolved metal impurities present in the unpurified $FeCl_2$ solution was reduced significantly (Chapter 3: Tables 4, 5 and 6). Since, in addition the Cu, Ni and Sn levels were reduced to 4.334, 4.409

and 1.559 mg L^{-1}, respectively, the electrolyte performance was improved significantly considering, for example, the capacity retention, which was only 0.1% lower than that obtained when using lab-grade $FeCl_2$. It is clear that the purified electrolyte outperformed the unpurified and performed similarly to the lab-grade in terms of all the parameters investigated, including the efficiencies (VE, CE and EE), storage capacity and capacity retention. Conclusively, the purification was successful in meeting the objective set for this study.

Recommendations

- Variables such as the cell configuration, battery testing station, temperature and electrolyte composition could be optimised to further reduce the capacity decay of both the purified and lab-grade $FeCl_2$, which in this study was 5.7% and 5.6%, respectively.
- To determine the effect of an additional purification step on the metal impurities, the purification process could be repeated using the purified crystals from the first purification step. If the cost of such a repetition remains lower than the price of pure crystals, the increased purity could result in an electrolyte that outperforms an electrolyte made from lab-grade chemicals.

Highlighting again the goal of developing a purification process that is rationally achievable, it should be one of low complexity. To achieve this, the process should exclude i) dangerous procedures, ii) highly specific lab equipment, iii) chemicals that are expensive or in short supply, and iv) the requirement of skilled chemists, which might not always be available or add substantial cost.

The process that was developed in this study and executed on a demonstration scale (40 L) is schematically illustrated in Figure 37. The process starts with an acidic aqueous solution that contains adequate amounts of $FeCl_2$ (1). Having said that, the process does allow for a wide concentration range of $FeCl_2$, as well as the presence of various types and amounts of impurities, which should, however, not exceed the $FeCl_2$ concentration. This source composition flexibility adds simplicity by providing a wide choice of unrefined sources of $FeCl_2$ that could be used for the electrolyte. After the $FeCl_2$ solution has been chosen, no application-specific vessel is required as the solution could be poured into an open vessel (preferably conically shaped) that is corrosion resistant, such as glass. N_2 is then bubbled through the solution (2), while thermal energy (3) is required to evaporate the solvent (typically water) into a standard fume extraction hood. By using N_2 to blanket hot $FeCl_2$ from oxygen, the process does not require an advanced inert and closed setup that will add to the cost, increase operational difficulties while increasing the risk of working with pressurised vapours.

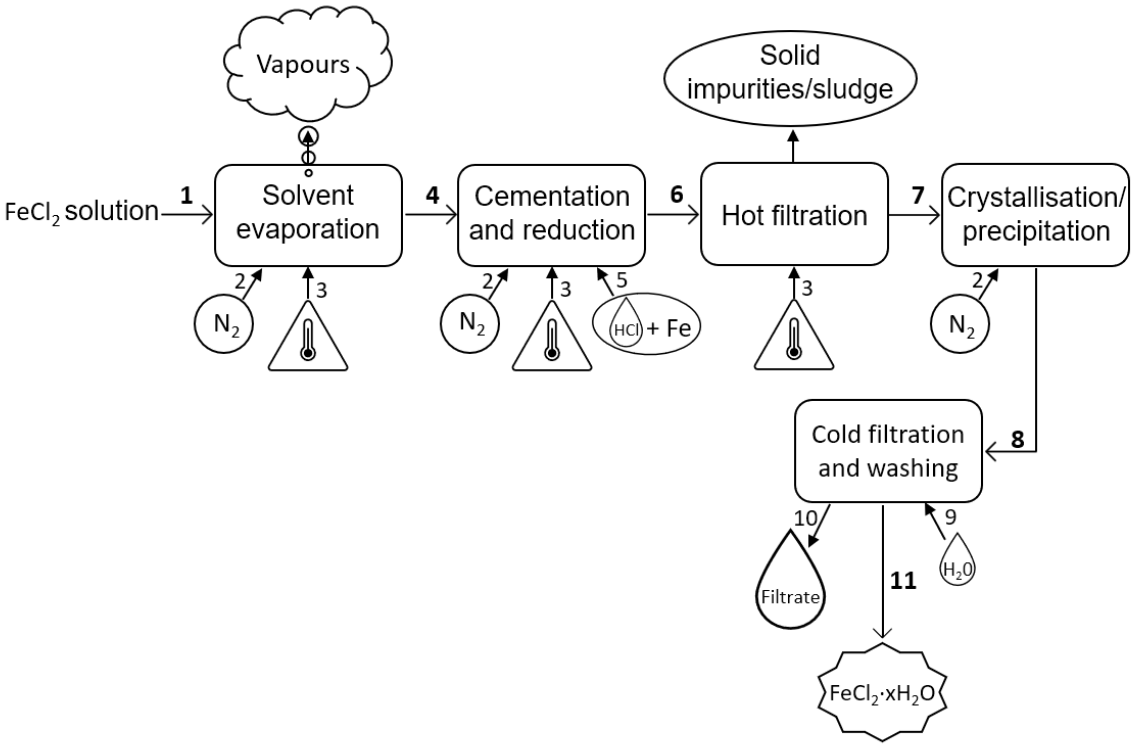

Figure 37: Flow diagram of the purification process established and used in this study.

After the desired Fe concentration has been reached (as indicated by the specific boiling-point temperature of ~119 °C), cementation is initiated (4) by adding Fe powder and HCl (5). During cementation, metal impurities nobler than Fe are cemented out of the solution, while simultaneously reducing Fe^{3+} to Fe^{2+}. Given the large surface area of iron powder being added to a saturated and boiling solution, it is imperative that the powder has to be added slowly to avoid a potentially dangerous exothermic reaction leading to uncontrolled foaming. While such a slow addition is a relatively simple solution, it nonetheless introduces a safety risk. After cementation, the solution needs to be filtered (6) to remove any unreacted iron, solid impurities, and possible sludge. This step will also require caution since the corrosive solution has to be filtered while hot to ensure that the product remains in solution, i.e. in the filtrate. However, with standard personal protective equipment (PPE) and the correct operating procedure, the risk of harm can be minimised. The hot solution can then cool to room temperature in any clean vessel, that was purged with N_2 (2), to allow $FeCl_2$ to crystallise. After crystallisation has reached an adequate solid to liquid ratio, the solution is easily (vacuum) filtered (8) to remove the $FeCl_2$ crystals from the filtrate (10). During this step, cold water (9), preferably pure, is used to help remove any remaining filtrate from the crystals.

Recommendations

- The small risk and level of complexity introduced by the addition of iron powder (5) could be reduced by lowering the surface area of the particles, therefore lowering the reaction rate. Since this would reduce the surface area available for impurities to precipitate, the amount of iron added might have to be increased.
- The hot filtration (6) introduces the risk of spillage and harm that could occur due to equipment malfunction or human error. Simple automation in the form of pumps/valves in this step would lower the chances of errors and remove the risk of human harm.
- A HAZOP analysis would have to be done to identify all possible risks and to determine best operational practice.

1.3 Economic feasibility

If a process is to be rationally feasible to be accepted for application, it should also translate to economic feasibility when considering large-scale applications. Of course, this should translate into the best compromise between economics and safety. It was also mentioned in the introduction that the purpose of developing this process was to reduce the cost of the electrolyte.

From the cost analysis of the electrolyte presented in Chapter 3 (Section 3.4 - Figure 23), the amount of iron solution required to produce 10 L of electrolyte would cost approximately R 20.30. Considering other sources of $FeCl_2$ could further reduce cost. Nonetheless, working with the current cost and including the costs of N_2 (2), Fe powder and HCl (5), while excluding the costs of Cr^{3+}, electricity and equipment, yielded a total of R 350.37 for 10 L of the Fe component of the electrolyte. Since this is only 5.42% of the cost of the lab-grade $FeCl_2$ that is commonly used in experimental ICRFB studies, this process is clearly economically viable.

Recommendations

Some optimisations can be proposed to the process presented in Figure 37, which might further reduce the cost of the electrolyte. These recommended changes, discussed below, are illustrated in Figure 38.

- The N_2 gas makes up the largest fraction of the cost at 61.1%. The amount of N_2 used during purification could be reduced without negatively affecting the degree of quality

of the produced $FeCl_2$ by lowering the flow rates and possibly cutting the N_2 supply during boiling, as outward flowing vapours should inhibit O_2 from reaching the solution.

- Since the pure iron powder is the second largest cost contributor at 29.3%, a new step (14) could be introduced (Figure 38), whereby any unreacted Fe powder is washed, extracted from the solids on the filter and reused for cementation (4), which would reduce the amount required and hence the cost of Fe powder.
- The filtrate (10) of step (8) does contain unprecipitated $FeCl_2$, as high concentrations are an important driving factor for crystallisation. Additionally, the washing of the crystals with water further increases the concentration of $FeCl_2$ in the filtrate. Recrystallising this filtrate (12) would increase the $FeCl_2$ yield per L of bought $FeCl_2$ solution, thereby further reducing the costs of the purification process.
- Finally, using water, albeit cold, to wash the crystals in step (8) does contribute to a decrease in yield. Substituting the water with, for example, an organic solvent such as ethanol or chloroform could contribute to an increase in the yield.

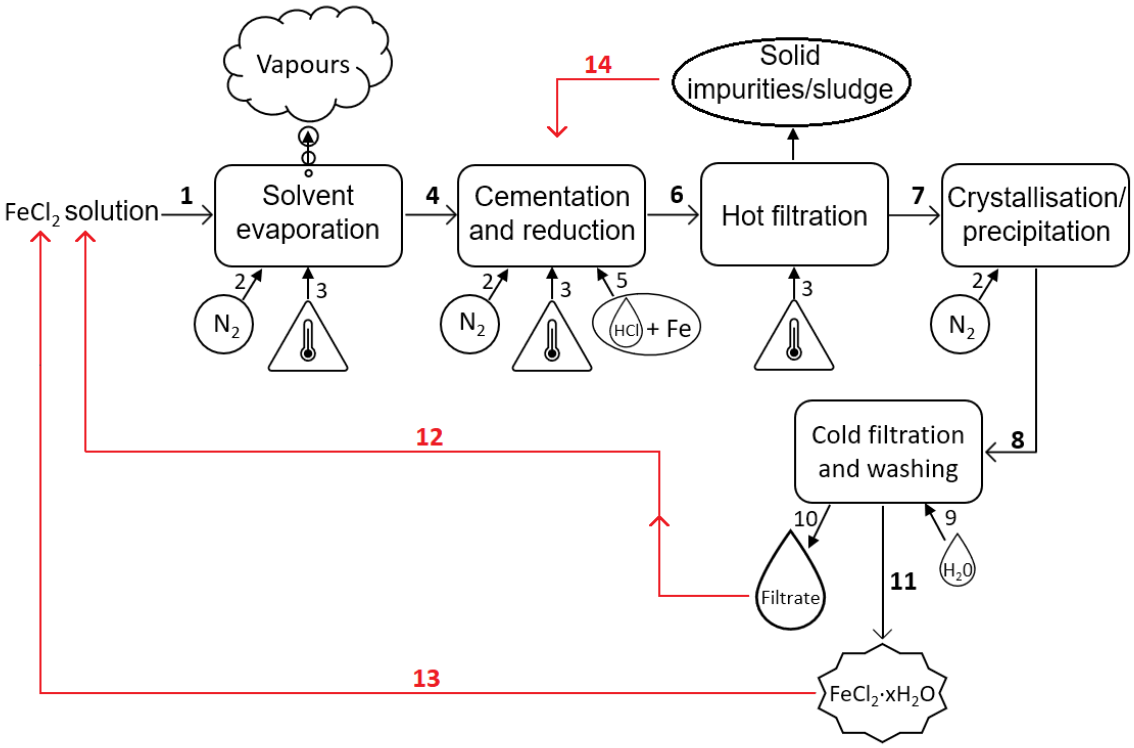

Figure 38: Flow diagram of the purification process established and used in this study, including possible optimisation possibilities.

2. $FeCl_2$ and positive electrolyte analysis

The second objective of this study was to develop a non-destructive and simplistic analytical technique that would be able to differentiate between Fe^{2+} and Fe^{3+} ions at relatively high concentrations. This technique should hold high application value for the ICRFB; therefore, measurements should be fast and non-destructive, hence excluding analytical methods that require sample preparation or destruction. This topic correlates to the principal aim set out for this research project, which was to aid in the advancement of the ICRFB as a feasible LESS. When introducing an analytical technique to quantify dissolved Fe^{2+} and Fe^{3+}, there were certain goals in mind. In Section 2.1, the accuracy and usefulness of the developed analytical technique will be evaluated, while additionally discussing the main challenges encountered together with their solutions. Section 2.2 will cover a short results section that correlates the first and second objectives of this study. Finally, recommendations are given on each section.

2.1 Iron redox speciation analysis technique

In this section, some of the main challenges encountered will be discussed, followed by the steps taken to obtain the desired results with a short discussion on whether the objective has been met. Finally, two possible recommendations are presented on how this process might be improved further.

Since the method should be able to accurately distinguish between Fe^{2+}/Fe^{3+} speciation, the first challenge encountered was the difficulty experienced in accurately creating samples for UV-Vis analysis, which is necessary for obtaining reliable molar absorption constants. After numerous repetitions of these experiments, the deviations could be ascribed to ambient temperature changes, miniscule differences in sample preparation and oxidation. Some of the adjustments that had to be made included installing a heat-regulated sample holder, adjusting the use of the electronic pipette to ensure consistency and optimising the amount of N_2 required to prevent oxidation. Eventually, after numerous experiments and modifications, a satisfactory accuracy was obtained for the method, where the largest obtained absolute errors for repeated analyses were 3.33% for [Fe^{2+}] and 3.08% for [Fe^{3+}]. The developed method therefore proved to be suitable in quantitatively distinguishing between Fe^{2+} and Fe^{3+} species at elevated concentrations (up to 1.3 M).

Secondly, the method would have to be suitable for the ICRFB application, i.e. a correlation between the method and its application in an RFB environment would be beneficial as a further validation of the method. Hence, multiple experiments were done in an attempt to draw

correlations between RFB imbalance and the UV-Vis analysis. However, attempting to use an RFB as an analytical method to validate another analytical method proved difficult. Firstly, solvent osmosis across the membrane in the RFB cell from the catholyte to the anolyte caused an increase in [Fe^{2+}], even when the catholyte was imbalanced with [Fe^{3+}] accumulation (See Appendix - Figure A 2 and Table A 1). Calculating a correct mass balance also proved difficult due to the many different phenomena at play during ICRFB operation. Since multiple repeated attempts to induce imbalance by cycling resulted in inaccuracies from bidirectional Fe/Cr migration over the membrane, solvent evaporation and solvent osmosis, synthetically imbalanced catholytes were used as opposed to obtaining imbalance from prolonged cycling (see Chapter 4 - Section 3.3.5.1). In a further attempt to improve repeatability, the bismuth catalyst was removed since the bismuth plating would have required an additional catalyst plating cycle.

After many failed attempts and adjustments, the decision was made to use an unmixed electrolyte configuration with single charge cycles for the method validation (see Chapter 3 - Section 5). This was the only logical solution since a mixed electrolyte configuration caused capacity gains due to Fe/Cr migration over the membrane. Another issue causing deviations when correlating a RFB to the UV-Vis method, was that hot electrolyte samples rapidly oxidised during the external sampling procedure. This caused lower-than-expected [Fe^{2+}] values for electrolytes that underwent any form of cycling in the heated RFB system, as seen in Figure 36 and in the appendix (Table A 2). After considering every issue and solution, the error of the correlation was still as high as 12.38%. Another reason why it was not possible to reduce this error further was the varying Nernst potentials obtained from the remaining [Cr^{3+}] in the anolyte. While using a different [Cr^{3+}] for each run would resolve the Nernst potential differences, it would introduce new variations in solution resistance, which in turn would affect the time taken for electrolytes to reach the cut-off potential.

Nonetheless, it can be concluded that the method could be integrated into an ICRFB system. However, to reduce the explainable error, the UV-Vis analysis should be used *in situ*, as it did not seem possible to use an external sampling method to obtain accurate correlations between an RFB and the UV-Vis method. In conclusion, the developed function, together with UV-Vis analysis, has shown sufficient functionality and accuracy with the potential to accurately analyse the iron redox speciation of the active metal species in the positive electrolyte, which in turn would provide accurate data for electrolyte rebalancing. In its current state, this newly developed technique could further contribute to ICRFB technology by being one step closer to having in-line SOC and SOH monitoring sensors.

Recommendations

- Additional research is required to develop an *in-situ* monitoring system containing a monochromatic NIR light and a light intensity sensor. This would allow actual real-time analysis of an electrolyte side stream while not drastically adding to the total costs of the technology. Furthermore, since hot analysed samples would not be exposed to air, which in turn leads to rapid oxidation, this would provide more accurate correlations between an ICRFB and the NIR spectra.
- Since it was found that [HCl] affects 920 nm absorption, the actual degree of HCl concentration variation in half-cells of battery operation should be determined. In a worst-case scenario, these results could indicate that the degree of [HCl] variations during cycling is too great for reliable analysis. In that case, using 900 nm instead of 920 nm could possibly avoid this issue, although this wavelength does result in slightly lower absorptions due to being further from the peak.
- Since a colour shift in the visible wavelength region exists when charging an ICRFB anolyte (Appendix - Figure A 3), a UV-Vis analytical method could also be developed for the anolyte, which would allow accurate SOC measurements while providing additional electrolyte information on active species concentrations in both half-cells (including membrane crossover) in real time. For this, the method development for Fe^{2+}/Fe^{3+} could, in principle, be applied to Cr^{3+}/Cr^{2+} using an *in-situ* measurement system, as it was observed in this study that external sampling also resulted in Cr^{2+} oxidation, even when samples were carefully injected underneath the solvents to avoid air exposure (Appendix - Figure A 4).

2.2 Analysis of purified $FeCl_2$

Finally, the analytical method should also be suitable to verify the effectiveness of the purification procedure (Chapter 3), as analysing the fraction Fe^{2+} of the total Fe content would provide information on possible unwanted oxidation that might have occurred. Since such verification would also confirm the usefulness of the analytical method itself, a brief discussion thereof is presented here.

The ratio of Fe^{2+}/Fe^{3+} was analysed in the unrefined $FeCl_2$ solution as well as a solution made from the crystals produced by purification. The UV-Vis method described in Chapter 4, varying the light absorption between 860 and 960 nm, was used on both solutions after adjusting the

total dissolved Fe concentrations to 1.30 M. From the results (Figure 39), the higher absorption obtained for the purified $FeCl_2$, which increased with increasing wavelength, shows that it contained more Fe^{2+} than the unrefined $FeCl_2$ solution. When using these absorption results in conjunction with the function derived in Chapter 4, the Fe^{2+}/Fe^{3+} content of the unrefined and purified $FeCl_2$ was 1.259 M / 0.041 M and 1.369 M / -0.069 M, respectively. The negative result for Fe^{3+} in the purified $FeCl_2$ is indicative that the $FeCl_2$ used to develop the function of absorption was slightly less pure than the $FeCl_2$ produced in this study, resulting in a slightly higher absorption than predicted by the function. Nonetheless, the results confirm that at least 3.2% of the Fe content in the unpurified $FeCl_2$ consisted of unwanted Fe^{3+}, which the purification procedure, specifically the addition of Fe powder and HCl, successfully reduced to Fe^{2+}. Additionally, this result confirms that the N_2 used with the open setup was effective in preventing oxidation during the entire purification procedure.

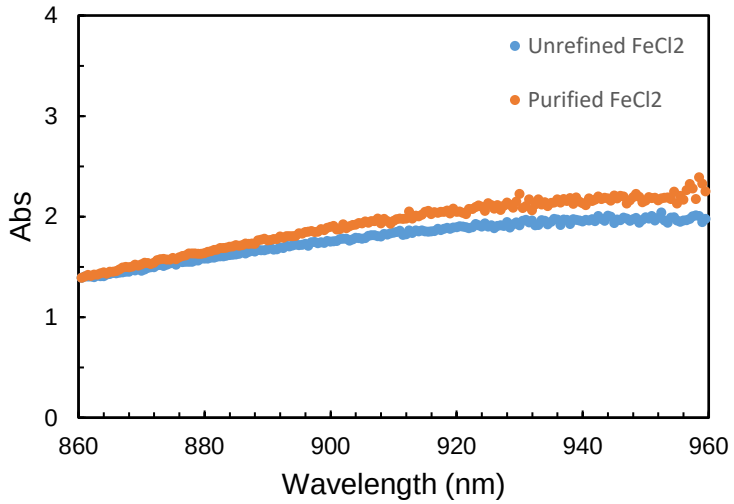

Figure 39: NIR Spectra of 1.30 M solutions of Fe in 1.0 M HCl, for unrefined $FeCl_2$ and purified $FeCl_2$ (25 °C).

In this section, the work done in Chapter 3 and Chapter 4 of this research project was appropriately connected. The successful analysis, using the analytical technique presented in Chapter 4, of the Fe^{2+} / Fe^{3+} ratio in the $FeCl_2$ produced by the process presented in Chapter 3, highlights the usefulness while linking the two main objectives of this study.

Recommendations

- Considering that Fe^{2+} readily oxidises to Fe^{3+}, it can be assumed that commercial $FeCl_2 \cdot 4H_2O$ could contain some degree of impurity. This was, therefore, also likely for the commercial $FeCl_2 \cdot 4H_2O$ used in this study, confirmed by the slightly negative value obtained for Fe^{3+} for the carefully purified and stored crystals. It could therefore be recommended that the function of absorption be revisited and reworked using purified and reduced $FeCl_2$, thereby minimising the presence of Fe^{3+}. This could further reduce the obtained error margin for Fe^{2+}/Fe^{3+} detection.

Appendix

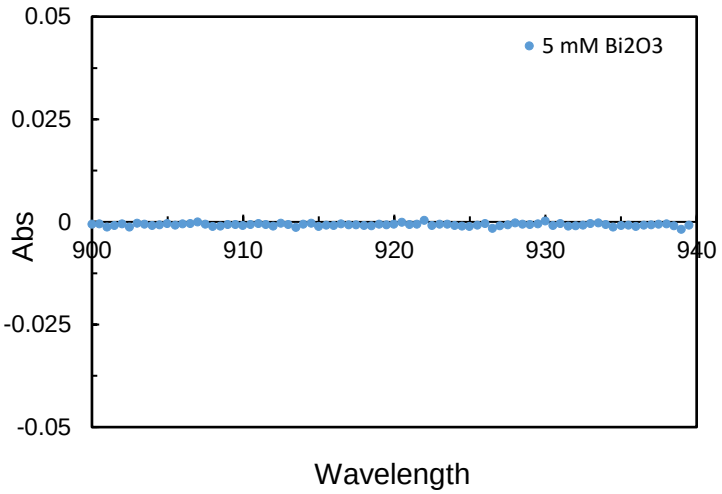

Figure A 1: NIR spectra (900-940 nm) of 5 mM Bi_2O_3 in 1.0 M HCl.

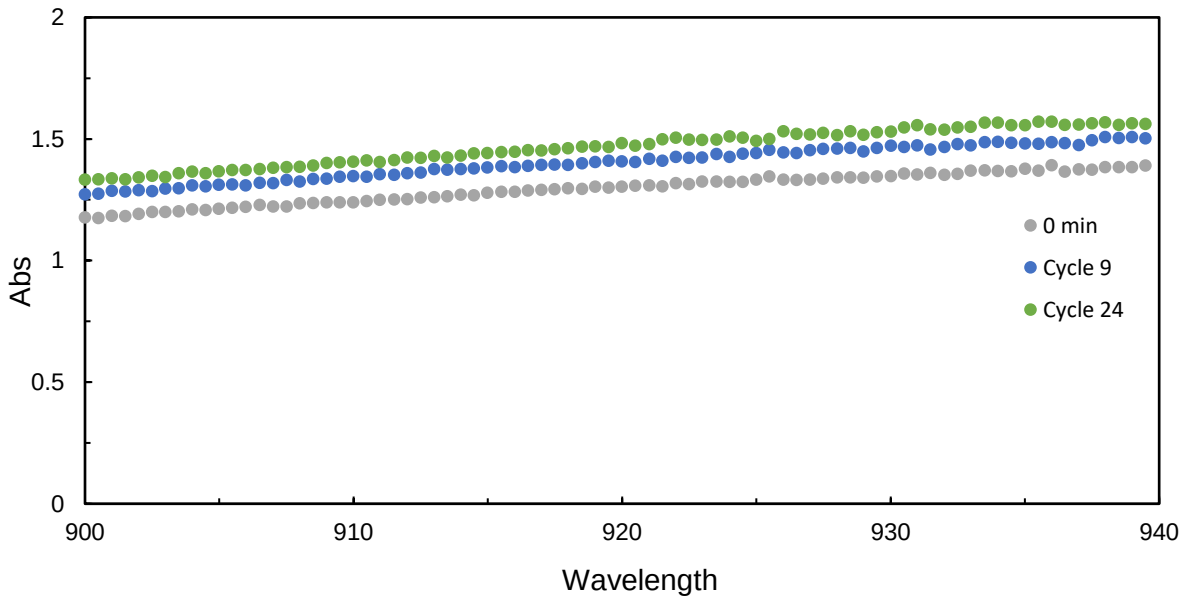

Figure A 2: NIR spectra (900-940 nm) of RFB cycled catholyte: 1 M Fe^{2+}, 1 M Cr^{3+}, 1 M HCl.

Table A 1: ICP-OES analysis of mixed configuration electrolyte before (i) and after (f) 24 cycles.

	Cr (mg L^{-1})	Fe (mg L^{-1})
Catholyte i	50.4	55.3
Anolyte i	50.4	55.3
Catholyte f	44.3	66.9
Anolyte f	59.0	49.1

Table A 2: Δ [Fe3] obtained from charge capacity of catholyte, vs Δ [Fe3] as obtained from UV-Vis method.

	Catholyte # and Fe^{2+}/Fe^{3+} ratios				
	# 1: 100 / 0	**# 2: 80 / 20**	**# 3: 60 / 40**	**# 4: 40 / 60**	**# 5: 20 / 80**
[Fe^{3+}] i from NIR	0.001	0.197	0.395	0.588	0.787
[Fe^{3+}] f from NIR	0.903	0.921	0.954	0.972	0.985
Δ [Fe^{3+}] from NIR	0.902	0.724	0.559	0.384	0.198
A h to C Δ [Fe^{3+}]	0.785	0.641	0.501	0.344	0.176
Correlation (%)	87.02	88.50	89.58	89.67	88.85

Figure A 3: Colour shift between uncharged (Cr^{3+}) anolyte and charged (Cr^{2+}).

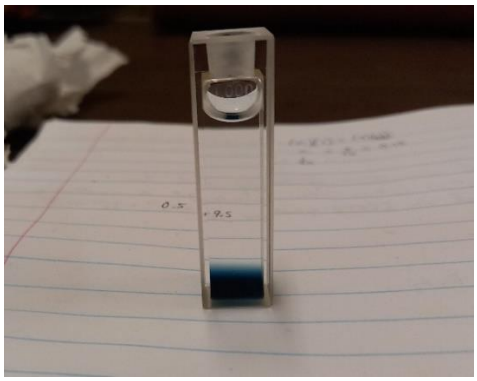

Figure A 4: Injection method used to combat Cr^{2+} oxidation in atmosphere.

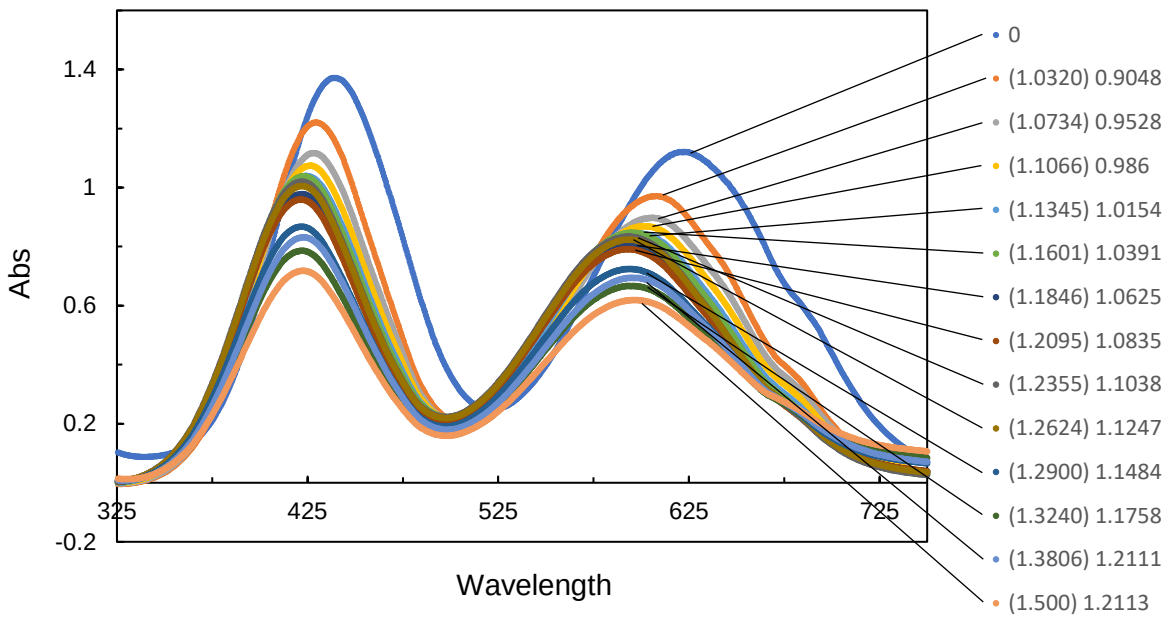

Figure A 5: Absorbance shifts in visible region of ICRFB anolyte (Cr^{3+}/Cr^{2+}) at (charging) and resting OCV potentials.